High Cycle Fatigue and Crack Arrest Analysis of Components with Compressive Residual Stress

Xuran Xiao

Submitted to the Department of Mechanical and Aerospace Engineering in fulfilment of the requirements for the degree of *Doctor of Philosophy*

2024

Declaration of Authenticity and Author's Rights

This thesis is the result of the author's original research. It has been composed by the author and has not been previously submitted for examination which has led to the award of a degree.

Xuran Xiao

08/07/2024

Previously published work

Some of the content within this thesis has been published in whole or in part for conference proceedings and journal publications listed in the List of Publications. The extent of the author's contribution to these works was 100% and as such no further clarification on the author's contributions to these works is necessary.

Xuran Xiao

08/07/2024

Abstract

This thesis presents a method based on fracture mechanics to predict the high cycle fatigue life of structures with induced compressive residual stress and to calculate the minimum autofrettage pressure required to achieve crack arrest.

For high cycle fatigue life assessment, the total fatigue life of a component is calculated as the sum of crack initiation life and crack propagation life. Three finite element models are included in the proposed method. In the first model, the residual stress distribution is determined using the tested monotonic stress-strain curve of the material. The second model simulates crack propagation, where the crack propagation life is evaluated by superimposing the applied load and residual stress fields. In the third model, an equivalent stress amplitude is calculated based on mean stress correction and applied to obtain the crack initiation life from a stress-crack initiation life curve, generated based on an assumed crack initiation length.

For crack arrest analysis, these three models are employed to determine an effective stress intensity factor. Crack arrest is then defined by comparing the effective stress intensity factor with the thresholds of crack propagation from various models. Finally, the minimum autofrettage pressure required to cause crack arrest is determined under a given working load cycle.

Two types of double-notched specimens made from 316L stainless steel and S355 low carbon steel are investigated to validate the accuracy of the proposed method. Numerical results show good agreement with experimental observations for both fatigue life prediction and crack arrest analysis. The proposed method is also applied to practical components from literature, demonstrating good applicability in the design of pressure vessels, valves, and pipes.

Publications

Journal papers:

1. X Xiao, V Okorokov, D MacKenzie, *High cycle fatigue life assessment of notched components with induced compressive residual stress.* International Journal of Pressure Vessels and Piping, 206: 105069.

Conference papers:

X Xiao, V Okorokov, D MacKenzie, *High Cycle Fatigue Analysis with induced Residual stress based on Fracture Mechanics.* Procedia Structural Integrity, 2024. 52: p. 111-121.

Acknowledgements

Firstly, I would like to thank my supervisors, Prof. Donald MacKenzie and Prof. David Nash, for providing me the opportunity to continue my studies at the University of Strathclyde as a PhD student. My sincere thanks to Prof. Donald MacKenzie for his support throughout this research. His wisdom and experience have been invaluable guidance on my academic journey.

I would also like to express my gratitude to my family and friends for their support. I am deeply grateful to my parents and grandparents in China; even though I am overseas, their countless acts of kindness always reach me. Special thanks to my girlfriend, Taiyang, whose love and companionship have motivated me to keep moving forward.

Contents

List of Figures

List of Tables

Nomenclature

σ_{ar}	Equivalent stress amplitude
ΔK_C	Extrinsic threshold
ΔK_{eff}	Effective stress intensity factor
$\varepsilon_f{}'$	Fatigue ductility coefficient
$\sigma_f{}'$	Fatigue strength coefficient
$\sigma_Y{}'$	Yield stress of expanded yield surface
$\Delta\sigma_\gamma{}'$	Range of transformed stress
$\Delta K_{th,a}$	Fatigue crack threshold for PSC
ΔK_{app}	Stress intensity factor of applied forces
ΔK_{dR}	Intrinsic threshold
ΔK_{eff}	Effective stress intensity factor range
ΔK_{eq}	Equivalent stress intensity range
ΔK_{thR}	Stress intensity factor threshold of LC
ΔS	Nominal stress range
$\Delta\varepsilon$	Strain range
$\Delta\sigma$	Stress range
$\Delta\sigma_{eR}$	Plain fatigue limit
a	Crack length
a_M	Material constant in FKM mean stress correction
a_N	Neuber factor
a_t	Crack transition length
b	Fatigue strength coefficient
b_M	Material constant in FKM mean stress correction

C	Material constant in Paris law
C_h	Initial hardening modulus
d_1	The transition between MSC and PSC
d_2	The transition between PSC and LC
E	Young's modulus
E_T	Tangent modulus
G	Energy-release Rate
G_r	Related stress gradient
K'	Material constant in Ramberg-Osgood equation
K^*	Fatigue crack driving force
$K_{max,app}$	Maximum applied stress intensity factor
$K_{min,app}$	Minimum applied stress intensity factor
K_f	Fatigue notched factor
K_{Ic}	Fracture strength
K_{max}	Maximum stress intensity factor
K_{min}	Minimum stress intensity factor
K_{op}	Crack opening stress intensity factor
K_{rs}	Stress intensity factor of residual stress
K_T	Stress concentration factor
L_c	Critical distance in TCD
L_M	Critical length in medium cycle fatigue region
L_s	Critical length of the static limit
m	Material constant in Paris law
M_σ	Mean stress sensitivity factor

n'	Material constant in Ramberg-Osgood equation
N_f	Number of cycles to failure
N_g	Crack growth life
N_i	Crack initiation life
N_t	Total fatigue life
Q	transform matrix
R	Stress ratio
R_∞	Saturation value of the yield surface
R_{eff}	Effective stress ratio
R_p	Crack tip plastic zone
$S_{alt\ ij}$	Alternating stress
$S_{eq\ ij}$	Equivalent alternating stress
S_e	Fatigue strength of the smooth structure
S_N	Fatigue strength of the notched structure
U	Ratio of ΔK_{eff} and ΔK
Y	Configuration factor
α	Back stress tensor
γ	Material constant in Walker equation
γ_h	Decreasing rate of the hardening modulus
ΔK_{th}	Threshold of fatigue crack propagation
$\Delta\sigma_0$	Amplitude of the fatigue limit
ε_a	Total strain amplitude
ε_{ea}	Elastic strain amplitude
ε_{pa}	Plastic strain amplitude

ε_{true}	True strain
ε-N	Strain-life
η	Fictitious crack tip
ν	Poisson's ratio
ρ	Radius of the notch tip
σ_{-1}	Fatigue strength under fully reversed cyclic stress
$\sigma_{1,\Delta\sigma}$	First principal stress of the stress range
$\sigma_{c,max}$	Maximum normal stress on the critical plane
$\sigma_{nm\ ij}$	Mean normal stresses
$\sigma_{1,2,3}$	Three principal stresses
σ_{∞}	Remotely applied stress
σ_a	Stress amplitude
σ_{AMP}	Absolute maximum principal stress
σ_m	Mean stress
σ_{max}	Maximum stress
σ_{min}	Minimum stress
σ_n	Nominal stress
σ_{rs}	Residual stress
σ_{SVM}	Signed Von Mises stress
σ_{true}	True stress
σ_u	Ultimate tensile strength
σ_V	Von-Mises stress
$\sigma_{xm,ym,zm}$	Mean stress on x,y,z direction
σ_Y	Yield stress

$\sigma_{\tau 1,2,3}$	Normal stresses on the critical plane
τ_{-1}	Fully reversed shear fatigue limit
$\tau_{1,2,3}$	Three maximum shear stresses
τ_a	Shear stress amplitude

Acronyms

CZM	Cohesive Zone Modelling
FEA	Finite Element Analysis
FKM	Forschungskuratorium Maschinenbau
HCF	High Cycle Fatigue
LC	Long cracks
LCF	Low Cycle Fatigue
LEFM	Linear Elastic Fracture Mechanics
MSC	Microstructurally small cracks
PSC	Physically small cracks
SIF	Stress Intensity Factor
SMART	Separating Morphing and Adaptive Remeshing Technology
TCD	Theory of critical distance
VHCF	Very High Cycle Fatigue
XFEM	Extended Finite Element Method

Chapter 1 Introduction

Pressure vessels, pumps, valves and pipes are important components of industrial systems to store, handle or transport liquids and gases at a wide range of pressures and temperatures. In the design of these industrial structures, sufficient strength, stiffness and fatigue life are basic conditions that must be met, otherwise design errors may have severe impact on the safety and environment. Fatigue failure is one of the main causes of failure of engineering structures. Critical equipment is subject to cyclic loading, thermal fluctuations and wind or seismic loads in special cases throughout their service time. These repeated loadings can lead to the nucleation of cracks and the development of crack propagation, which can undermine the structural integrity and the safety of these components and ultimately disable the entire industrial systems. The maximum value of the cyclic load is often smaller than the safe load estimated by static ductile fracture analysis. Therefore, the issue of fatigue failure in these components has received considerable attention among engineers and researchers. Engineers have developed several methods for extending the fatigue life of structures by inducing residual stress such as shot peening, swage autofrettage and hydraulic autofrettage. Then, estimating the fatigue life becomes a challenge for researchers.

Several standards have been proposed to assess the fatigue life of structures, including the Forschungskuratorium Maschinenbau (FKM) guideline [1] developed in Germany, ASME Boiler and Pressure Vessel Code [2] developed in America. These structural safety assessment procedures have been successfully applied in design by engineers. However, based on some research, the results of fatigue life obtained by these standards may be conservative [3]. Additionally, for situations involving induced residual stress, the approaches in standards may not be suitable and require adjustment by introducing factors related to the residual stress. However, as the residual stress is induced by different approaches, simply adding "residual stress factors" to the standards may not be suitable.

1.1 Objectives

Autofrettage is one of the fatigue life extension methods which can be applied widely in industrial fields such as the aerospace industry, oil and gas industry, etc. However, it is unrealistic to verify or observe the influence of autofrettage through experiments due to the huge cost of experiments. Therefore, the purpose of this study is to propose a numerical method based on Finite Element Analysis (FEA) to predict the influence of autofrettage on the fatigue life and the fatigue limit. To achieve the purpose, double-notched specimens were designed for the fatigue tests to be compared with the numerical results from the proposed method. Furthermore, the proposed method is applied to some practical 3D structures for validation.

1.2 Outline of the Thesis

This thesis consists of eight chapters and the topics of these chapters are outlined as follows.

Chapter 2 introduces the definition of the fatigue, some fatigue life enhancement methods and summarizes three main fatigue life assessment methods. Among which, the stress-based approach and the fracture mechanics approach are focused on.

Chapter 3 presents the monotonic stress-strain curve and the cyclic stress-strain curve and some constitutive models applied to fit these curves based on the obtained experimental data.

Chapter 4 proposes a methodology to assess the fatigue life under compressive residual stress. The total life of structures with induced compressive residual stress can be calculated by adding the crack initiation life with the crack propagation life. The crack initiation life is obtained by the stress-crack initiation life ($S - N_i$) curve determined by an assumed crack initiation length and the simulation of the crack growth on the smooth specimen. The crack propagation life with induced residual stress is obtained by an effective stress intensity factor (ΔK_{eff}) that consists of the effect of the stress intensity factor of residual stress (K_{rs}), applied forces (ΔK_{app}) and the stress ratio. A new method based on the superposition method and FEA is applied to calculate the K_{rs}.

Chapter 5 focuses on the application of the proposed methodology, double-notched specimens are designed and tested to determined their fatigue life with and without the residual stress. The numerical obtained fatigue life based on the proposed method is then validated by the experimental results.

Chapter 6 focuses on the application of the proposed method on the practical structures. Cross bore blocks and injection system components in diesel engines from literatures are employed to be investigated by the proposed method. The influence of structure responses on the crack growth simulation is discussed.

Chapter 7 extends the application of the proposed method to the determination of the minimum autofrettage pressure. The effective stress intensity factors obtained from various autofrettage pressures can be compared with the thresholds in different stages of crack propagation to find the minimum autofrettage pressure that causes the crack arrest. The influences of two kinds of threshold models on the crack arrest analysis are also discussed.

Chapter 8 summarizes the conclusions from each chapters and provides the future work of this thesis.

Chapter 2 Fatigue Life Assessment

Fatigue life refers to the number of cyclic loads to which a material or structure is subjected until failure. From the development process of fatigue damage, fatigue can be divided into three stages as crack initiation, crack propagation and final fracture as shown in Figure 2.1. The number of cycles from the start of loading to the crack reaching a given crack initiation length is the crack initiation life. Thereafter, the number of cycles from the crack initiation extending to the final crack length is the crack growth life. In the last stage, the structure goes through rapid fracture and the life is significant short.

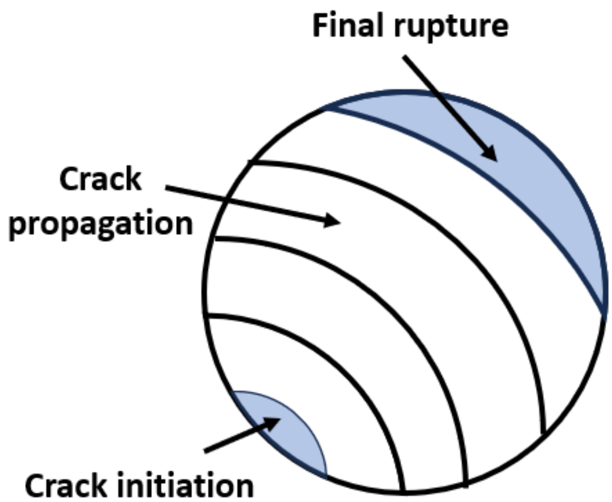

Figure 2.1． Three stages of fatigue life model.

2.1 Fatigue Life Enhancement Through Induced Residual Stress

Residual stress is an internal stress in a component even when subjected to no external loading. This stress can be induced in practical manufacture due to mechanical processes (machining, cutting and grinding) and thermal processes (welding). The presence of residual stress can have both negative and positive effects on the fatigue life. For instance, in the welding process, the residual stress is induced as a consequence of temperature gradients that result in compressive strain along the welding path compared to other areas. Once the cooling process is completed, this compressive stress is transformed into tensile residual stress on the critical points which can decrease the fatigue life of structures. On the contrary, if compressive residual stress is induced, the fatigue life may be increased. Based on this concept, engineers and researchers have developed various approaches to induce compressive residual stress in regions prone to fatigue crack initiation and propagation, to enhance fatigue life. This can be achieved through several different mechanical processes, such as shot peening, laser peening, low plasticity burnishing, swaging and autofrettage.

2.1.1 Shot Peening and Laser Peening

Shot peening and laser peening are both methods used to induce compressive residual stress on the surface of structures to increase fatigue life.

Shot peening is a cold working process where small spherical media are impacted on the surface to form small indentations, which can be regarded as plastic deformations. After shot peening, compressive residual stress is induced on the surface. This offsets the tensile stress under working loads to enhance the structure from the fatigue failure. For example, experimental investigations of shot-peened surfaces in 316 stainless steel have shown that the number of cycles required to form a crack increased from 8000 to 500,000 after shot-peening intensity with 12.2N and the crack propagation rate was also decreased due to the residual stress. In addition, peened specimens can have longer crack initiation life than polished specimens [4]. Therefore, shot peening is widely applied in structures such as aircraft engine blades, aircraft fuselage and transmission system parts in automobiles.

In laser peening, a laser with high power density and short pulse is employed to induce a strong shock wave within the metal. When the peak value of the shock wave is larger than the yield strength of the metal, plastic deformation occurs on the surface, resulting in compressive residual stress [5]. Zhang et al. investigated fatigue life improvement by laser peening Ti-6AL-4V with a constant load ratio fatigue test. According to the experimental investigation, the fatigue life of laser peened specimens was increased by 22.2% to 41.7% compared to as-received specimens [6]. Laser peening can induce deeper and larger compressive residual stress compared with shot peening [7] and can maintain a clean surface finish. Therefore, it has been used to extend the fatigue life of key aviation components.

2.1.2 Low Plasticity Burnishing

Low plasticity burnishing developed from traditional ball burnishing and roller burnishing techniques. In comparison to these methods, low plasticity burnishing controls the pressure applied on the structure by a spherical fluid bearing tool to just exceed the yield stress of the material [8]. With this technology, a layer of compressive residual stress can be created by the plastic deformation to enhance the fatigue life. According to experiments on the fatigue performance for Inconel 718 after low plasticity burnishing, the surface roughness of specimens declined by 64.3% to 70.6% compared with the as-received specimens, and according to the tested results of specimens under three different burnishing pressures, the fatigue life of specimens was increased by approximately 37.1%, 62.4% and 82.4% respectively [9]. Low plasticity burnishing can extend the fatigue life without significantly changing the shape and tolerances of components and has been widely applied to the repair of commercial aircraft components.

2.1.3 Swage Autofrettage

Swage autofrettage is widely applied in the nuclear industry. In swage autofrettage, an oversized tapered mandrel is pushed through the bore of the tube inducing plastic deformation at the interior wall. After swage autofrettage, compressive residual stress is induced on the internal surface, leading to increased the fatigue life [10]. According to the experiment results of the fatigue life of thick-walled cylinders through a hybrid rotational-swage autofrettage, the fatigue life of different cylinders subject to a range of internal pressure can be increased by 15.37 times for SS316 cylinder and 377.33 times for Al7075-T6 cylinder [11].

2.1.4 Hydraulic Autofrettage

Engineers must explore alternative methods to enhance fatigue life to meet design requirements. While increasing wall thickness can reduce maximum stress and thereby increase fatigue life, this approach has limitations and can also raise costs. Therefore, autofrettage as a localized surface strengthening method becomes a favourable option for fatigue enhancement to eliminate the need to change the shape and material of the component. Detailed numerical and experimental analyses of hydraulic autofrettage have been carried out by many studies [12-14]. The method of hydraulic autofrettage is commonly applied to pressure vessels with thick walls, and involves subjecting the components to an intense internal pressure through a hydraulic liquid [15].

In hydraulic autofrettage, the component is subject to internal pressure great enough to cause limited plastic deformation in highly loaded regions prior to service. When this autofrettage pressure is reduced to zero, the elastically deformed regions of the vessel seek to recover their original dimensions but are prevented from doing so by the permanent deformation of the plastically deformed material, inducing residual compressive stress at these locations. Experimental investigations have shown that this procedure can significantly increase the fatigue life of components or vessels in subsequent operations. Mughrabi *et al*. found the fatigue limit can be increased by more than 40% by autofrettage [16]. Other autofrettage studies by Rees, Underwood *et al*., Badr *et al*., Lee and Koh, PoLzl and Schedelmaier, Thumser *et al*., Sellen *et al*. have reported fatigue strength increase in excess of 60% [17-23].

For instance, half of a thick-walled cylinder is shown in Figure 2.2, considering a 2D structure, the radial stress and hoop stress based on elastic analysis can be calculated analytically [24]. For elastic-perfectly plastic material, the radial and hoop stress can be calculated as well by equations [25] and the residual stress can be described by equations [26].

After hydraulic autofrettage, compressive residual stress can be induced on the internal surface as shown in Figure 2.2 (b). With the same internal pressure, the hoop stress through the thickness can be changed from Figure 2.2 (a) to Figure 2.2 (c) where the maximum tensile hoop stress on the internal surface shown in Figure 2.2 (a) encounters the compressive residual stress and then is decreased as shown in Figure 2.2 (c).

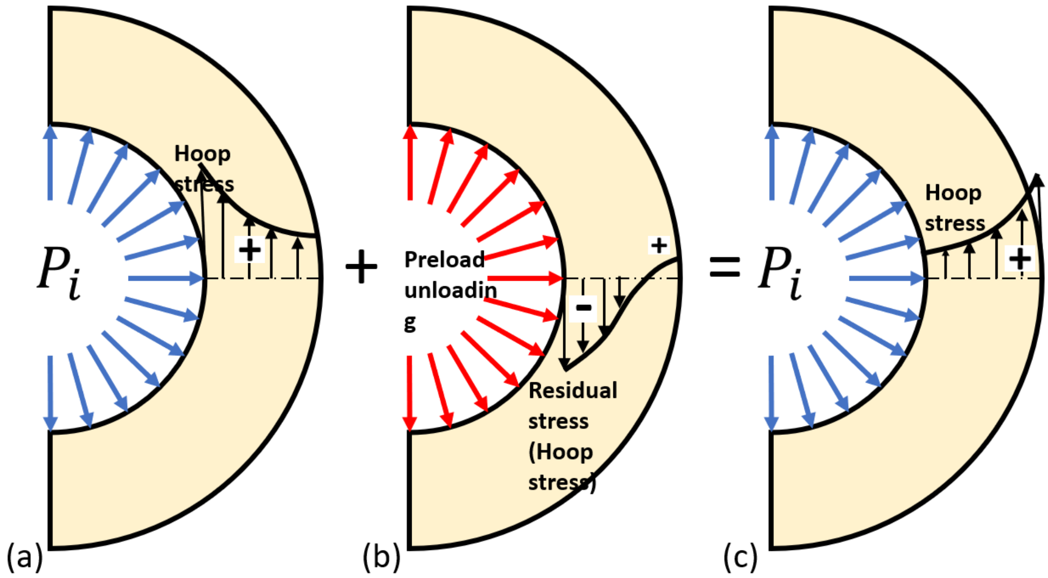

Figure 2.2. Theory of autofrettage: (a) Hoop stress of thick-walled cylinder with internal pressure; (b) Residual stress distribution; (c) Hoop stress distribution after autofrettage.

2.2 Fatigue Categories

The load that causes a material or structure to fail under monotonic loading is called the static strength. The fatigue failure occurs due to the repeated stress or strain and the number of times or cycles leading to failure is called fatigue life and the load value that corresponds to the fatigue life is fatigue strength. Fatigue can be classified from different perspectives. From the perspective of the stress state at the critical points, fatigue can be classified as uniaxial fatigue and multiaxial fatigue. Uniaxial fatigue refers to the stress state at the critical point of a material or structure that experiences only one stress or strain component, as observed in a fatigue test, for instance. In contrast, multiaxial fatigue refers to the stress state that experiences two or three stress or strain components that independently vary periodically with time. Additionally, based on the types of cyclic loadings applied to the structure, fatigue can be classified into mechanical fatigue (structures only subject to mechanical loadings), thermomechanical fatigue (structures subject to thermal loadings and mechanical loadings), creep fatigue (structures under high temperature conditions), and corrosion fatigue (structures in chemically corrosive environments) and so on.

The fatigue life of a structure at room temperature is determined by the cyclic load. Based on the number of cycles to failure, it can be classified as low cycle fatigue (LCF) when less than around 10^4 cycles, high cycle fatigue (HCF) when greater than around 10^4 cycles up to 10^7 cycles, whereafter it is classified as very high cycle fatigue (VHCF).

In this chapter, only mechanical fatigue is considered, and uniaxial and multiaxial fatigue criteria discussed. In addition, the fatigue life assessment methods appropriate for different lengths of fatigue life are introduced. There are three common methods to estimate fatigue life: the stress-life method, the strain-life method and the fracture mechanics method. The stress-life methods and fracture mechanics methods are focused on here.

2.3 Constant Amplitude Stressing

When the maximum and minimum stress levels of the cyclic loading are constant, as shown in Figure 2.3, the cyclic loading is called constant amplitude loading.

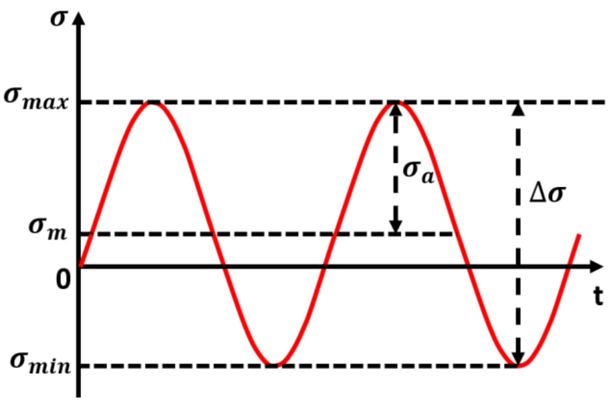

Figure 2.3. Cyclic loading with constant amplitude stressing.

As shown in Figure 2.3, σ_{max} and σ_{min} are the maximum and minimum cyclic stress. The stress cycle is characterised by stress range, $\Delta\sigma$. σ_a is the stress amplitude, σ_m is the mean stress and R is the stress ratio. The relationships between these stresses are shown in equations (2.1) to (2.4).

$$\Delta\sigma = \sigma_{max} - \sigma_{min} \tag{2.1}$$

$$\sigma_a = \frac{\Delta\sigma}{2} = \frac{\sigma_{max} - \sigma_{min}}{2} \tag{2.2}$$

$$\sigma_m = \frac{\sigma_{max} + \sigma_{min}}{2} \tag{2.3}$$

$$R = \frac{\sigma_{min}}{\sigma_{max}} \tag{2.4}$$

Cyclic stressing can be specified in terms of the stress ratio R. If $R = -1$, $\sigma_m = 0$ and the absolute values of σ_{max}, σ_{min} are equal. This fully-reversed cycle is shown in Figure 2.4 (a). When $R = 0$, σ_{min} is zero, $\sigma_a = \sigma_m = \frac{\sigma_{max}}{2}$. This stress cycle is called as zero-based or zero-to-tension cycling, as shown in Figure 2.4 (b). These two cases of cycling are the most common cases considered in fatigue life assessment methods.

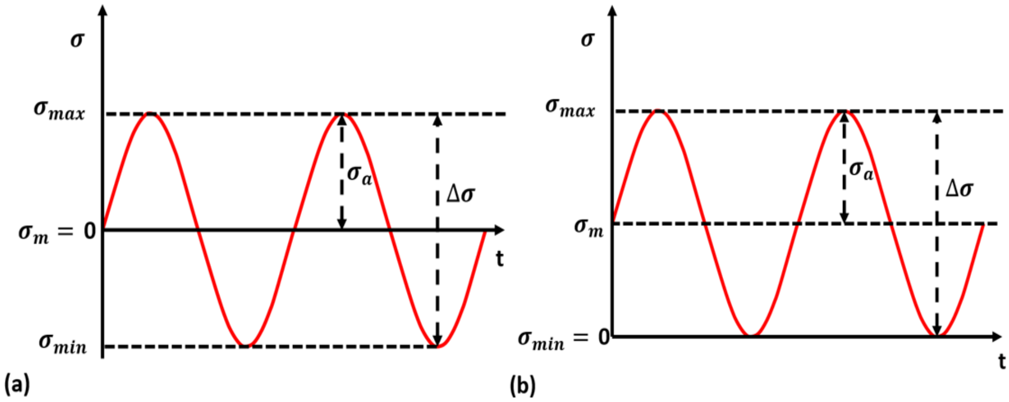

Figure 2.4. Two specified cyclic stressing (a) Fully-reversed cycling (b) Zero-based cycling.

2.4 Stress Life Approach

When a structure is subjected to cyclic loading, fatigue cracks form and propagate until complete fracture occurs. Higher stresses result in a smaller number of cycles to failure, while lower stresses lead to a larger number of cycles. To estimate the fatigue life from stress, it is necessary to establish the relationship between nominal stress and the number of cycles to failure for several different test stress levels, as illustrated in Figure 2.5 (a) where the stress -life data obtained from fatigue tests are included. LCF, HCF and VHCF regions are distinguished by the number of cycles to failure. The stress-life data can be fitted by a curve called as the stress versus life (*S*-

N) curve. It can be applied to calculate the life if the nominal stress amplitude is determined.

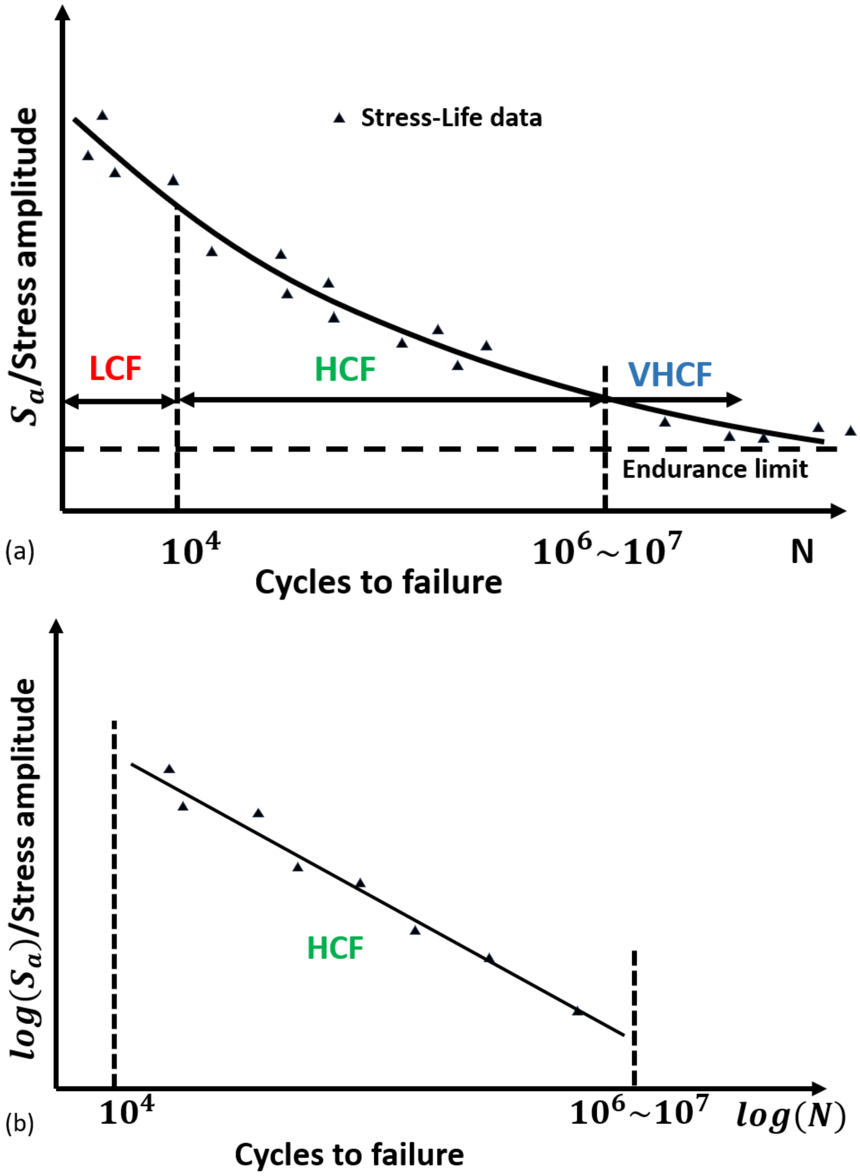

Figure 2.5. (a) Classical stress-life curve. (b) Stress-life curve of HCF in log-log plot.

Commonly, *S-N* curves in HCF region are plotted on log-linear or log-log scales as shown in Figure 2.5 (b) so that the S-N data can be assumed to lie on a straight line and can be fitted mathematically as:

$$\sigma_a = C + D \log N_f \tag{2.5}$$

where C and D are material constants for log-linear scale.

In log-log plot:

$$\sigma_a = A{N_f}^B \tag{2.6}$$

where A and B are also material constants.

(2.6) can also be expressed as:

$$\sigma_a = {\sigma_f}'(2N_f)^b \tag{2.7}$$

(2.7) is called the Basquin equation, which has been widely adopted by researchers, where ${\sigma_f}'$ and b are material constant for fully reversed cyclic loading.

2.4.1 Mean Stress Correction

Although, the stress range is the main feature to affect fatigue failure, it can also be influenced by the mean stress. Tensile mean stress trends to decrease the fatigue life [27], but compressive mean stress may increase it [28-30].

The stress-life curve and strain-life curve are generated based on fatigue tests with specific stress ratios. To apply these curves across various stress ratios, they are typically converted to the fully reversed cyclic loading condition ($\sigma_m = 0, R = -1$) using mean stress correction. If the mean stress is not zero, to apply these curves, the mean stress is required to be considered by some mean stress correction method. Fatigue strength varies with changes in mean stress. To estimate the endurance limit under different mean stress conditions, various simple models have been developed. For the stress life method, the three widely used models are Gerber model, Goodman model and Soderberg model [31] as shown:

Gerber model
$$\sigma_a = \sigma_{-1}\left[1 - \left(\frac{\sigma_m}{\sigma_u}\right)^2\right] \tag{2.8}$$

Goodman model
$$\sigma_a = \sigma_{-1}\left[1 - \left(\frac{\sigma_m}{\sigma_u}\right)\right] \tag{2.9}$$

Soderberg model
$$\sigma_a = \sigma_{-1}\left[1 - \left(\frac{\sigma_m}{\sigma_Y}\right)\right] \tag{2.10}$$

where, σ_{-1} is the fatigue strength under fully reversed cyclic stress and σ_u is the tensile strength, σ_Y is the yield stress.

All three models are shown in Figure 2.6, with the same mean stress, the corrected fully-reversed stress amplitude of Gerber model is the largest and the Soderberg gives smallest value. Therefore, compared with Gerber and Goodman models, Soderberg model is the most conservative for tensile mean stress that the mean stress is positive [32]. In addition, all these three models are employed typically with tensile mean stress as shown in Figure 2.6 and needs to be updated for the situation with negative mean stress.

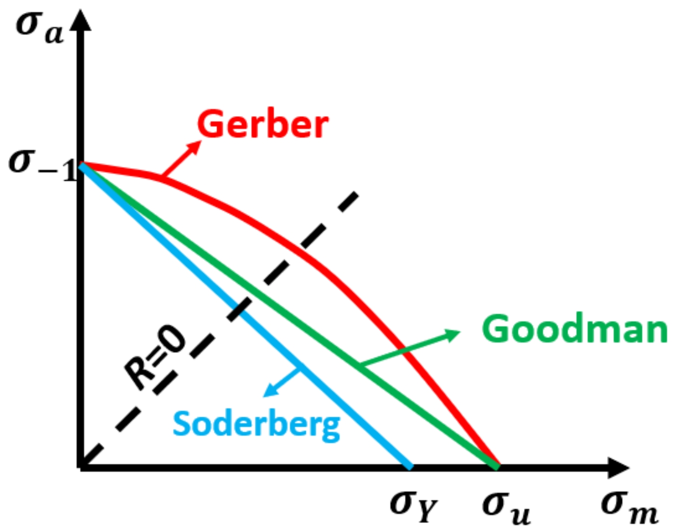

Figure 2.6. Gerber, Goodman and Soderberg mean stress correction model.

The Walker equation (2.11) [33] may be a better choice to be applied in the negative mean stress region compared with previous three models to calculate the equivalent stress amplitude:

$$\sigma_{-1} = \sigma_a\left(\frac{1}{2-R}\right)^{1-\gamma} \tag{2.11}$$

where, γ is a material constant.

A mean correction method included in the FKM guideline [34] is available for a wider range of R ratios, as shown in Figure 2.7. The so-called Haigh diagram is divided by four regimes by the R ratios as follows:

- Regime 1: The values of R are larger than 1, but the mean stress is negative. In this situation, the maximum stress and the minimum stress are compressive.

- Regime 2: -∞ $\leq R \leq 0$, the minimum stress is negative or equal to 0. Two specific cases are included in this regime that fully reversed cyclic loading ($R = -1$) and zero-based cyclic loading ($R = 0$).
- Regime 3: 0< $R < 0.5$, both maximum stress and minimum stress are tension.
- Regime 4: $0.5 \leq R < 1$, the alternating stress in this regime is high.

For the four regimes shown in Figure 2.7: the equivalent stress amplitude ($R = -1$) can be corrected from the mean stress as:

$$\sigma_{ar} = \sigma_a \qquad \text{for Regime 1 and 4} \tag{2.12}$$

$$\sigma_{ar} = \sigma_a + M_\sigma \sigma_m \qquad \text{for Regime 2} \tag{2.13}$$

$$\sigma_{ar} = (1 + M_\sigma)\frac{\sigma_a + (M_\sigma/3)\sigma_m}{1 + M_\sigma/3} \qquad \text{for Regime 3} \tag{2.14}$$

where, M_σ is the mean stress sensitivity factor:

$$M_\sigma = a_M \sigma_u + b_M \tag{2.15}$$

and, a_M and b_M are material constants.

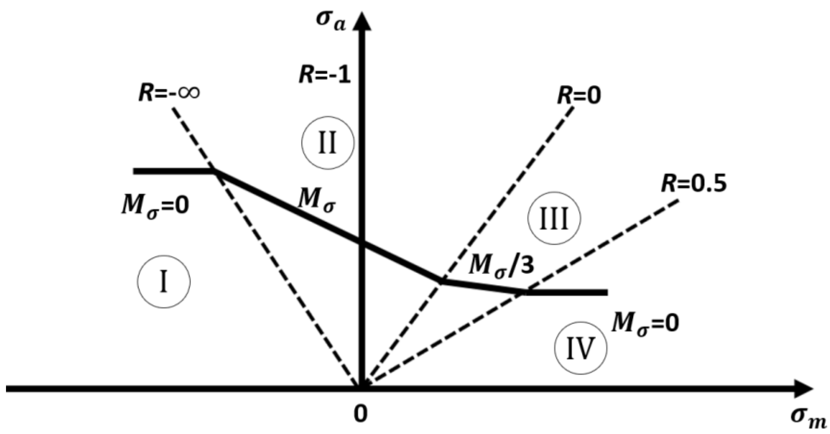

Figure 2.7. Four regimes in the FKM-guideline mean stress correction graph.

Although mean stress can influence the fatigue life, there are some situations where the mean stress effect is ignored. For instance, for welded structures where the residual stress is induced after a heat-intensive process [35], high longitudinal tensile residual stress is present in the weld [36-38]. Initially, researchers believed that this induced tensile residual stress could lead to tensile mean stress, resulting in a decrease in the fatigue life [39]. However, further research found that the mean stress has no notable effect on fatigue failure since with high tensile residual stress, the stress in the welded joints can reach the yield point, even though the applied external stress is not large, making the mean stress effect negligible [40]. Nevertheless, some researchers argue that the residual stress effect on the mean stress in welded structures should be considered due to the relaxation of the residual stress after applied load cycles, especially during the first cycle [41-44]. Additionally, there are some approaches trying to induce compressive mean stress in the weld to increase the fatigue life [45].

2.4.2 The Influence of Stress Concentration

Notches in a structure, such as a sharp change in cross-sectional, can increase the stress and strain in the local region of the structure. This phenomenon is called stress concentration and can be expressed by stress concentration factor K_T as (2.16).

$$K_T = \frac{\sigma_{max}}{\sigma_n} \tag{2.16}$$

where, σ_n is nominal stress as shown in Figure 2.8.

Stress concentration is a common phenomenon in structures. Compared with safety design under static loading, the effect of stress concentration is more significant in fatigue design under cyclic loading. This is because when a structure is subjected to cyclic loading, even if the nominal stress is less than the yield stress, plasticity may still be induced in local region with high stress concentration factors, causing fatigue damage. Therefore, the fatigue life of the entire structure is dependent on the local stress and strain. Since the concept of stress concentration factor was proposed, many experiments have been performed to obtain the stress concentration factor and the longitudinal stress distribution σ_{yy}, shown in Figure 2.8.

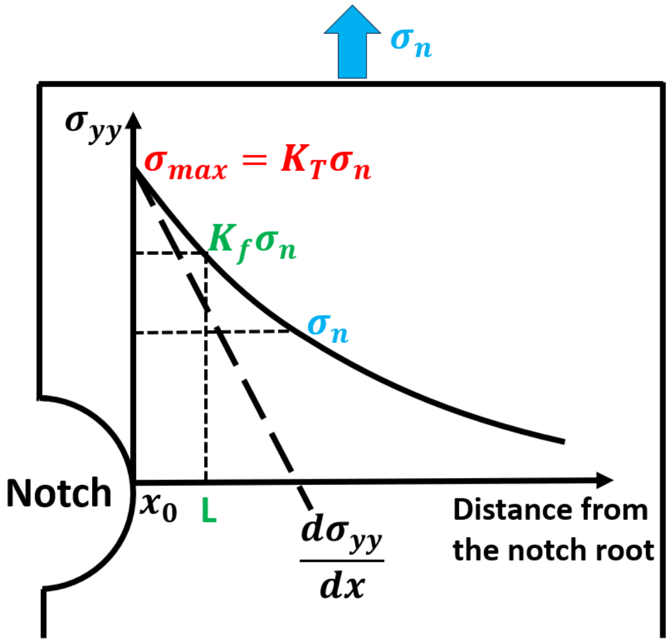

Figure 2.8. Stress distribution along the notch.

For instance, in a single notched flat specimen, the stress concentration factor can be affected and determined by the radius of the notch root [46, 47]. By multiplying the nominal stress with the K_T, the maximum stress, σ_{max} on the notch root, x_0 in Figure 2.8 can be determined. Then, σ_{yy} of the vicinity of the notch tip can then be estimated from σ_{max} by polynomial functions, but for more complex structures, Finite Element Analysis is required.

Although, stress concentration has significant influence on fatigue strength, the theoretical stress concentration factor K_T can not fully describe those effects. In application of the stress life method to notched specimens, if the maximum stress calculated from the stress concentration factor is substituted into *S-N* curve to calculate the fatigue life of the structure, the results may be underestimated. For instance, in welding structures, researchers have proposed the concept of hot-spot stress, which is related to the stress distribution in the front of the weld toe rather than directly on the weld toe, to estimate the fatigue life [48]. Therefore, a concept called the fatigue notched factor K_f has been proposed as:

$$K_f = \frac{S_e}{S_N} \tag{2.17}$$

where, S_e is the fatigue strength of the smooth structure and S_N is the fatigue strength of the notched structure. Several methods were proposed to determine the value of K_f. In the line method proposed by Neuber [49], a length L could be selected as shown in Figure 2.8, and when the average stress over the length was larger than the fatigue strength, fatigue damage would occur. In this theory, the K_f can be calculated from the K_T as:

$$K_f = 1 + \frac{K_T - 1}{1 + \sqrt{\frac{a_N}{\rho}}} \tag{2.18}$$

where, a_N is a function of yield stress and it is called the Neuber factor. ρ is the radius of the notch tip. Similar to Neuber's theory, Peterson [50] assumed that the fatigue damage occurred when the point stress at a distance from the notch tip was larger than the fatigue strength of the smooth structure. Then K_f can be presented as:

$$K_f = 1 + \frac{K_T - 1}{1 + \frac{a_P}{\rho}} \tag{2.19}$$

K_T is easier to obtain than K_f by experiments or finite elements analysis. Therefore, the value of K_f is typically determined from K_T by assessing the ratio of K_T/K_f in the FKM guideline [51]. n_σ is employed to represent the ratio which can be determined by the related stress gradient (G_r), the tensile strength and the width at the notch net section.

The related stress gradient is an important factor in FKM, and for a simple structure it can be determined directly by the radius of the notches [52]. However, for more complex structures, the values of G_r have to be obtained from the practical stress distribution in the vicinity of the notches shown in Figure 2.8 as (2.20).

$$G_r = \frac{1}{\sigma_{max}} \frac{\partial \sigma_{yy}}{\partial x}\bigg|_{x=x_0} \tag{2.20}$$

where, x_0 is the coordinate point where the stress is the maximum stress.

In both Neuber's and Peterson's theories, a length must be determined to calculate the average stress or the point stress. A new theory named as the theory of critical distance (TCD) was proposed by Taylor [53] to define a critical distance where the average of stresses should be calculated. The critical distance L_c can be calculated by:

$$L_c = \frac{1}{\pi}(\frac{\Delta K_{th}}{\Delta \sigma_0})^2 \tag{2.21}$$

where, ΔK_{th} is the threshold of fatigue crack propagation and $\Delta \sigma_0$ is the amplitude of the fatigue limit.

The TCD approach has been proven to have high accuracy when employed to predict fatigue failure [54]. However, the length L_c of (2.21) is mostly used in high cycle fatigue prediction. In medium cycle fatigue region, the critical length is assumed as a function of the number of cycles as:

$$L_M = A(N_f)^B \tag{2.22}$$

where, L_M is the critical length in medium cycle fatigue region and N_f is the number of cycles to failure. A and B are material constants, where $A > 0$ and $B < 0$.

Two methods can be applied to determine the values of A and B. The first method is based on the static and fatigue limits. When the stress amplitude is equal to the static-limit loading, the life is N_s. The critical length L_M versus N_f relationship can be determined as:

$$L_M = L_s = \frac{1}{\pi}(\frac{K_{Ic}}{\sigma_u})^2 \tag{2.23}$$

where, L_s is the critical length of the static limit, K_{Ic} is fracture strength and σ_u is the ultimate tensile stress. Meanwhile, when the amplitude stress is equal to the fatigue-limit loading, the life is N_0. The critical length L_M versus N_f relationship is:

$$L_M = L_0 = \frac{1}{\pi}(\frac{K_{th}}{\sigma_0})^2 \tag{2.24}$$

Then

$$B = -\frac{\log(\frac{L_s}{L})}{\log(\frac{N_0}{N_s})} \tag{2.25}$$

$$A = LN_0{}^{-B}$$

The second method is dependent on two *S*-*N* curves: one for a plain specimen and another for a notched specimen. For a given life N_i, the corresponding amplitude stress in plain specimens, $\sigma_{a,p}$ should be equal to the stress in the critical length. In addition, for the same given life N_i, the result of the corresponding amplitude stress in notched specimens, $\sigma_{a,n}$ multiplied by K_T, is equal to the maximum stress on the notch root. Then the critical length can be calculated by two or more selected N_i, as shown in Figure 2.9.

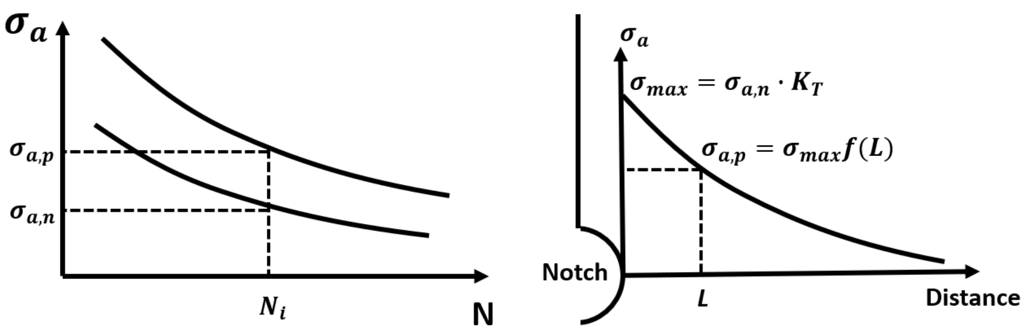

Figure 2.9. Critical length determination in TCD.

2.4.3 Limitation of TCD Method

In (2.21), the critical length in TCD is determined by the values of ΔK_{th} and $\Delta\sigma_0$. As both values are dependent on the stress ratio R, a key premise of TCD is that the stress ratio must be constant. However, after autofrettage with the presence of the induced compressive residual stress, the stress ratio and the mean stress are variable, such that the TCD approach is not directly applicable. The approach mentioned in the Section 2.4.2 can be applied to determine the critical length with a specific autofrettage pressure by conducting experiments to generate the *S*-*N* curve for autofrettaged notched specimens and plain specimens. However, a large number of fatigue tests must be conducted for both autofrettaged notch specimens and plain specimens. Moreover, the critical distance varies with different autofrettage pressures. Therefore, conducting these tests for the determination of critical length can be expensive.

2.5 Strain Life Approach

Similar to the stress life approach, in the strain life approach the number of cycles to failure is determined by the strain range, and the relationship between strain and the fatigue life is expressed by the strain-life (ε-N) curve as shown in Figure 2.10. The strain life data in this curve is collected by strain controlled fatigue test and for each test, amplitudes of strain, stress can be obtained from a hysteresis loop as shown in Figure 2.10 as well and for longer fatigue life, the hysteresis loop is smaller with less strain amplitude.

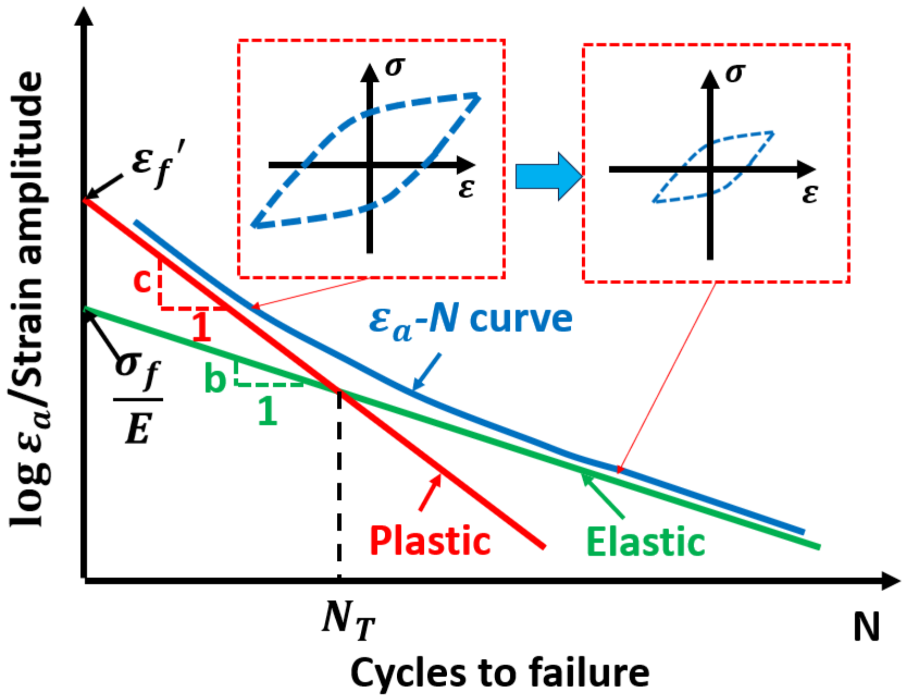

Figure 2.10. Classical strain-life curve.

The ε-N curve can be described by the Manson-Coffin equation, which is the most widely used in the form:

$$\varepsilon_a = \varepsilon_{ea} + \varepsilon_{pa} = \frac{\sigma_f{}'}{E}(2N)^b + \varepsilon_f{}'(2N)^c \tag{2.26}$$

where, ε_a is the total strain amplitude, ε_{ea} is the elastic strain amplitude and ε_{pa} is the plastic strain amplitude. $\sigma_f{}'$ and b are fatigue strength coefficients, $\varepsilon_f{}'$ and c are fatigue ductility coefficients. All these coefficients should also be obtained from the fully reversed cyclic loading test [55].

The Manson-Coffin equation consists of elastic parts and plastic parts, as shown in Figure 2.10, where, the red line is for plastic and the blue line is for elastic. There is an intersection point (N_T) of the elastic and plastic lines. When $N< N_T$, the plastic strain plays the main role in fatigue and when $N> N_T$, the elastic strain has a key effect on fatigue.

2.5.1 Local Stress-strain Approach

For notched structures, fatigue failure arises from the accumulation of fatigue damage in localized areas, which is influenced by the magnitude of local stress and strain. In response to this, methods have been proposed to estimate the fatigue life of notched structures by local stress-strain analysis [56]. The cyclic stress-strain curve and the Neuber rule transforming the nominal stress spectrum into the local stress-strain spectrum at the critical area is included in this method. Subsequently, life estimation is conducted based on the local stress-strain history and the Manson-Coffin equation (2.26).

The local stress-strain method is predominantly employed for evaluating LCF, where, compared to the HCF, the area around the notch root mostly undergoes plastic deformation, as shown in Figure 2.11. The gradient in (2.20) is smaller in the plastic zone, so that the stress or strain at the notch root can represent the stress or strain distribution around the notch area. However, in elastic stress or strain distribution, the gradient is larger and the “average stress” around the notch root cannot be represented by a single stress or strain at the notch root.

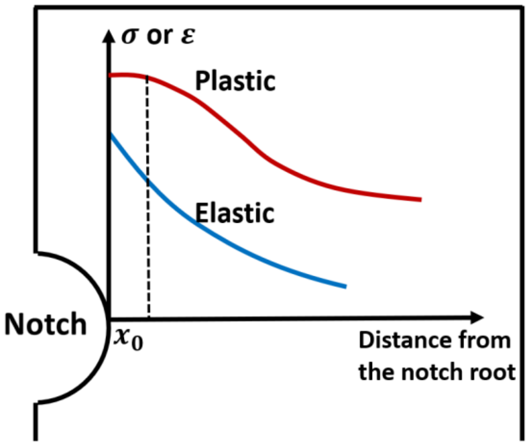

Figure 2.11. Comparison of elastic stress-strain distribution with plastic stress-strain distribution around the notch root.

The procedure for estimating the fatigue life of structures by applying the local stress-strain method is shown in Figure 2.12.

(1) Identification of critical point: Mostly, the points or areas on the structure with high concentration factors.

(2) Determination of the nominal stress spectrum and the cyclic stress-strain curve for the material of the structure.

(3) Calculation of the local stress-strain spectrum by FEA or Neuber approximate solution. In Neuber's approximate solution, (2.27) with Neuber constant, *C* and (2.28) are employed to calculate the stress and strain range.

$$\Delta\sigma\Delta\varepsilon = \frac{{K_f}^2 \Delta S^2}{E} = C \tag{2.27}$$

$$\frac{\Delta\varepsilon}{2} = \frac{\Delta\sigma}{2E} + (\frac{\Delta\sigma}{2K'})^{1/n'} \tag{2.28}$$

The Neuber approximate solution can be described as shown in Figure 2.13. In each cycle, nominal stress either increases or decreases, enabling the calculation of the Neuber constant based on this change. Then, by solving the (2.27) and (2.28), the increment or decrement of stress and strain can be determined. Finally, the stress and strain state at the critical point at the end of each cycle can be obtained.

(4) Calculation of the fatigue life by the strain-life curve and the accumulation of fatigue damage.

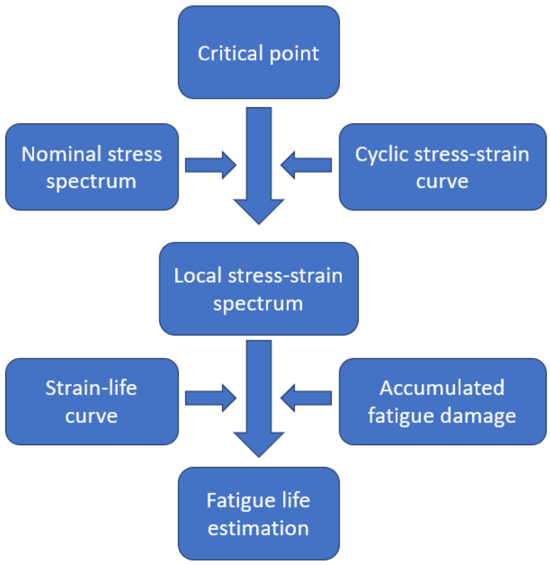

Figure 2.12. The procedures of local stress-strain method.

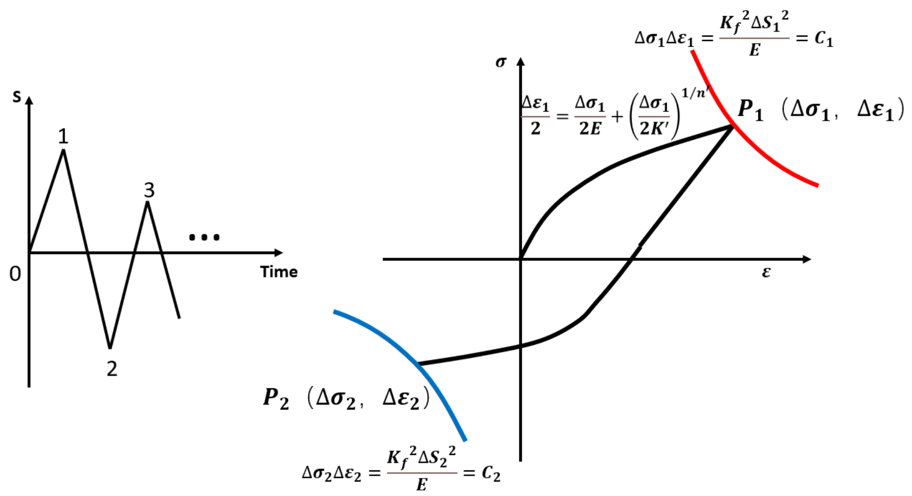

Figure 2.13. Neuber approximate solution.

2.6 Multiaxial Fatigue

S-N curves are commonly based on 1D stress. However, for real structures experiencing 3D stress, the results from 3D analysis need to be related to 1D material properties. Several multiaxial fatigue failure criteria have been proposed by researchers, among which, the most successful and widely used criterion is the critical plane approach [57], which is related to the Tresca yield criterion. Findley proposed that variable shear stress on the critical plane was the main factor to generate fatigue damage, and the stress normal to the critical plane affected the ability of the material to resist fatigue damage. Based on this theory, he proposed a linear function combining the shear stress amplitude and normal stress as a fatigue criterion [58]. Kandil proposed a strain critical plane criterion [59] and McDiarmid proposed a stress criterion [60]. Brown proposed that the crack generated at the plane with the maximum shear stress and propagated along the orientation of the maximum normal strain [61]. The influence of the mean stress on the critical plane approach can be expressed on the normal strain or stress in Susmel's work[62] as:

$$\tau_s = \tau_a + (\sigma_{-1} - \frac{\tau_{-1}}{2}) \cdot \frac{\sigma_{c,max}}{\tau_a} \tag{2.29}$$

where, τ_a is the shear stress amplitude on the critical plane, $\sigma_{c,max}$ is the maximum normal stress on the critical plane, σ_{-1} and τ_{-1} are the fully reversed tensile and shear fatigue limit. In summary, in the critical plane approach, the shear stress amplitude and normal stress are employed for the estimation of fatigue failure with high accuracy [63]. This fatigue criterion is also included in the ASME BPVC VIII Div 3 [64] where the principal stresses are employed to calculate the maximum shear stress as show in Figure 2.14.

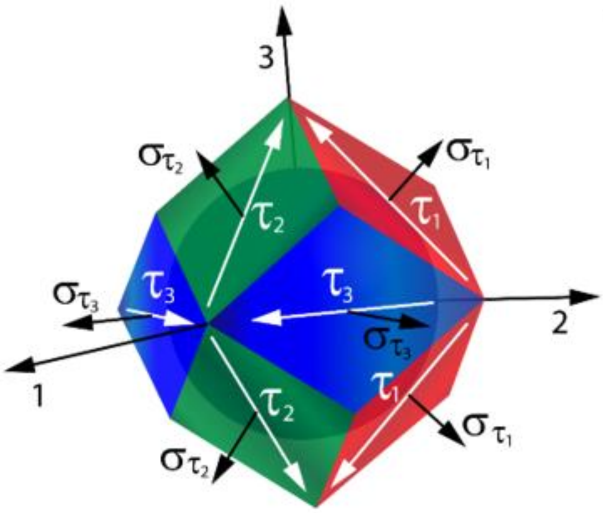

Figure 2.14. Maximum shear stress around a point.

As shown in Figure 2.14, the maximum shear stresses on the three planes are:

$$\tau_1 = \frac{\sigma_2 - \sigma_3}{2} \tag{2.30}$$

$$\tau_2 = \frac{\sigma_3 - \sigma_1}{2}$$

$$\tau_3 = \frac{\sigma_1 - \sigma_2}{2}$$

where, $\tau_{1,2,3}$ are three maximum shear stresses on the planes and $\sigma_{1,2,3}$ are principal stresses.

The normal stresses on planes are:

$$\sigma_{\tau 1} = \frac{\sigma_2 + \sigma_3}{2} \tag{2.31}$$

$$\sigma_{\tau 2} = \frac{\sigma_3 + \sigma_1}{2}$$

$$\sigma_{\tau 3} = \frac{\sigma_1 + \sigma_2}{2}$$

The procedures included in the ASME BPVC VIII Div. 3 are based on Figure 2.14 to determine the fatigue controlling stress components as follows:

- Determine the values of principal stresses ($\sigma_1, \sigma_2, \sigma_3$) at the interest points during the cyclic loading.
- Calculate the principal stress differences:

$$S_{12} = \sigma_1 - \sigma_2 \tag{2.32}$$

$$S_{23} = \sigma_2 - \sigma_3$$

$$S_{31} = \sigma_3 - \sigma_1$$

Determine the stress differences under the maximum cyclic loading ($S_{ij\,max}$) and the stress differences under the minimum cyclic loading ($S_{ij\,min}$). An alternating shear stress range $S_{alt\,ij}$ ($i \neq j = 1,2,3$) is defined for each stress difference.

Then, all the alternating stress can be calculated as:

$$S_{alt\,ij} = 0.5(S_{ij\,max} - S_{ij\,min}) \tag{2.33}$$

All stress differences can be obtained as: $S_{alt\,12}$, $S_{alt\,23}$, $S_{alt\,31}$.

- The mean stresses are the normal stresses on the planes of the maximum shear stresses, calculated as:

$$\sigma_{n\,12} = 0.5(\sigma_1 + \sigma_2) \tag{2.34}$$

$$\sigma_{n\,23} = 0.5(\sigma_2 + \sigma_3)$$

$$\sigma_{n\,31} = 0.5(\sigma_3 + \sigma_1)$$

  where, $\sigma_{n\,ij}$ is applied to represent any one of these normal stresses. The mean normal stresses can be calculated as:

$$\sigma_{nm\,ij} = 0.5(\sigma_{n\,ijmax} + \sigma_{n\,ijmin}) \quad \text{For } S_{ij\,max} < S_y \text{ and } S_{ij\,min} > -S_y \tag{2.35}$$

$$\sigma_{nm\,ij} = 0 \quad \text{For } S_{alt\,ij} \geq S_y$$

- Finally, the equivalent alternating stress $S_{eq\,ij}$ can be obtained by the mean stress correction method included in the ASME code as:

$$S_{eq\,ij} = S_{alt\,ij} \frac{1}{1 - \beta\sigma_{nm\,ij}/S'_a} \tag{2.36}$$

  where, β is a material constant and S'_a is the amplitude of fatigue limit with zero mean stress and 10^6 fatigue life cycles.

One of the limitations of the critical plane approach and Tresca criterion is that the fatigue controlling stress is determined by the maximum shear stress, which is not invariant. When the principal directions change during the load cycle, the maximum shear stress amplitude cannot be determined easily by the procedures above. The critical plane must be obtained considering the change of the shear stress plane [65, 66]. This problem can be easily resolved if the fatigue controlling stress is taken to be the von Mises stress, which is invariant. However, when applying the Von Mises stress, compressive stress cannot be represented as negative. To solve this problem, a method with signed Von Mises stress [67] is proposed as:

$$\sigma_{SVM} = \frac{\sigma_{AMP}}{|\sigma_{AMP}|} \cdot \sqrt{\frac{(\sigma_1 - \sigma_2)^2 + (\sigma_2 - \sigma_3)^2 + (\sigma_3 - \sigma_1)^2}{2}} \tag{2.37}$$

where, σ_{SVM} is the signed Von Mises stress, σ_{AMP} is the absolute maximum principal stress and is usually defined as $\sigma_1 > \sigma_2 > \sigma_3$ in FEA. For compressive residual stress, although the value of σ_3 is negative, the absolute value of σ_3 is larger than σ_1, so the σ_{AMP} in (2.37) can be defined by σ_3 and the value of σ_{SVM} is negative and in the same way, the value of σ_{SVM} for tensile residual stress is positive. However, there are concerns regarding the signed von Mises approach, as it may not provide as accurate results as the critical plane approach [68, 69].

2.7 Fracture Mechanics Fatigue Method

Fatigue can be studied from various perspectives. Both stress-based and strain-based approaches are based on a continuum, focusing on the number of cycles leading to failure and relating these cycles to stress and strain. However, from the nature of the fatigue mechanism, the process of studying fatigue is also the process of studying cracks. Fatigue generally refers to the damage of a structure under repeated loads, which includes the following stages: formation of cracks, crack propagation and fracture. In more detail, it includes the formation of slip bands, small crack propagation, long crack propagation and final fracture. After crack initiation, the typical fatigue crack propagation process of metallic materials can be divided into three stages, as microstructurally small cracks (MSC), physically small cracks (PSC) and long cracks (LC) [70]. The microstructurally small cracks and physically small cracks can be considered to be small cracks. The study of fracture mechanics fatigue method is based on the analysis of crack length.

2.7.1 Crack Initiation

Traditionally, total fatigue life is considered to be the sum of crack initiation life and crack propagation life. The crack initiation life is difficult to determine if the crack initiation length does not have an exact value and the complexity of micro crack monitoring methods. To predict the crack initiation life numerically, engineers often assume the crack initiation length based on experience, and the values used are often different. The crack initiation length plays an important role in addressing the issue of fatigue life prediction, as crack initiation life can be a significant part of the total life, especially for high cycle fatigue [71]. It is therefore important to define at which length crack initiation terminates and crack propagation starts.

The typical fatigue process for metallic materials can be divided into MSC growth PSC growth and LC growth. Among these, the nucleation and MSC growth are difficult to represent through a numerical model, but the rate of PSC and long crack growth can be represented by the Paris law [72]. For engineering applications, it is convenient to treat the MSC length as the initiation crack length.

Investigations of microstructurally small crack growth [73-75] have shown that in the early stage, several fatigue cracks occur from persistent slip bands and then stretch across one grain. However, most of the cracks stop at the boundary of grains, and the crack can only extend when adjacent grains have nearly identical orientations. By observing the micro-cracks in the grains of 316L stainless steel, Obrtlik et.al [75] gave a crack transition length (a_t) which divided the whole fracture process into a crack generation region and a crack propagation region. The crack generation was limited by reaching a_t, which could be assumed as the crack initiation and was the length of one or two average grains sizes. As the average length of grains in their investigation was $100\mu m$, the value of a_t can be assumed as $200\mu m$. Similarly, Angelika and Huang [73] proposed that two-segment cracks were formed when a micro-crack in a grain broke through the boundary and grew into another one, and, likely, three or more kinks formed by crack growth. Pham and Holdsworth [74] proposed that the size of an MSC was affected by the applied strain amplitude and the temperature, by observing the first fatigue striation of material 316L steel, for which the average grain size is about 60 μm.

2.7.2 Small Crack Propagation

The presence of a small crack implies that its dimensions are within the same order of magnitude as the structural scale of the material. In such cases, the assumption of a macro-continuum can no longer be considered valid. Determining the precise size range for what constitutes a "small crack" varies and is often drawn from experimental findings specific to a given material. The Kitagawa-Takahashi diagram [76] was proposed to define the range of cracks as shown in Figure 2.15. The crack growth length is divided into three stages in the KT diagram. Length d_1 is the microstructurally small crack length, from d_1 to d_2 is physically small crack growth and after d_2 is long crack growth.

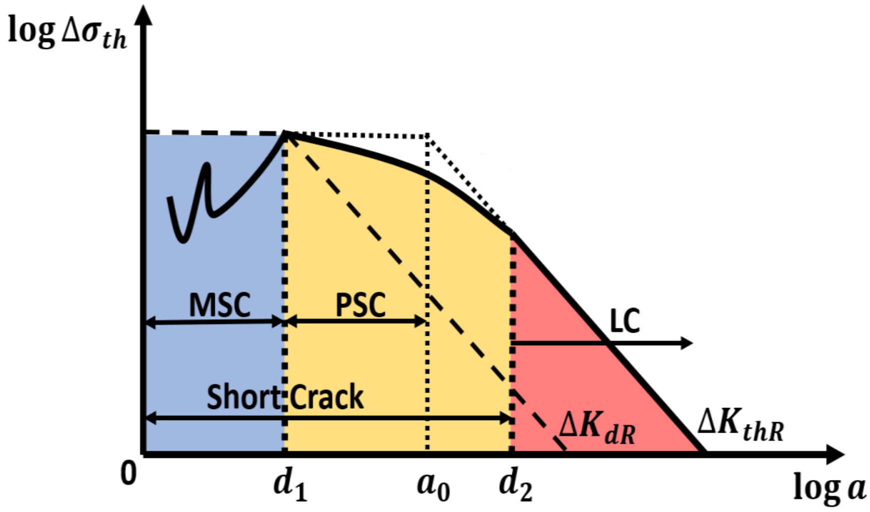

Figure 2.15. Kitagawa-Takahashi diagram showing the threshold.

EI Haddad proposed that the structural scale of a material was a_0, where a_0 can be determined from the stress intensity factor threshold of LC (ΔK_{thR}) and the fatigue strength amplitude at high number of cycles to failure ($\Delta\sigma_{eR}$) as:

$$a_0 = \frac{1}{\pi}(\frac{\Delta K_{thR}}{\Delta\sigma_{eR}})^2 \tag{2.38}$$

A crack length less than a_0 should be defined as a small crack. The a_0 in EI Hadded's equation is same as the critical distance in TCD. Based on the applicability of linear elastic fracture mechanics, Miller proposed the cracks smaller than d_2 should be defined as small cracks [77, 78].

KT diagram shown in Figure 2.15 is the most widely used tool to describe the short crack threshold. There are two available models to describe the curve in the KT diagram. One of these is the EI Haddad model [79] where $\Delta K_{th,a}$ is a function of ΔK_{thR} with crack size and the transition between PSC and LC (d_2) as:

$$\Delta K_{th,a} = \Delta K_{thR}\sqrt{\frac{a}{d_2}} \tag{2.39}$$

where, $\Delta K_{th,a}$ is the crack size dependent stress intensity factor threshold of PSC. The EI Haddad model has been successfully applied in the calculation of $\Delta K_{th,a}$ in the fretting fatigue crack arrest analysis [80, 81]. Another model was proposed by

Chapetti. In this model, the nonlinear threshold is considered. In the Chapetti model, the types of thresholds during crack propagation can be summarized as the intrinsic threshold ($\Delta K_{th,d}$) and the extrinsic threshold (ΔK_C) as in (2.40) and shown in Figure 2.16.

$$\Delta K_{th,a} = \Delta K_{dR} + \Delta K_C \tag{2.40}$$

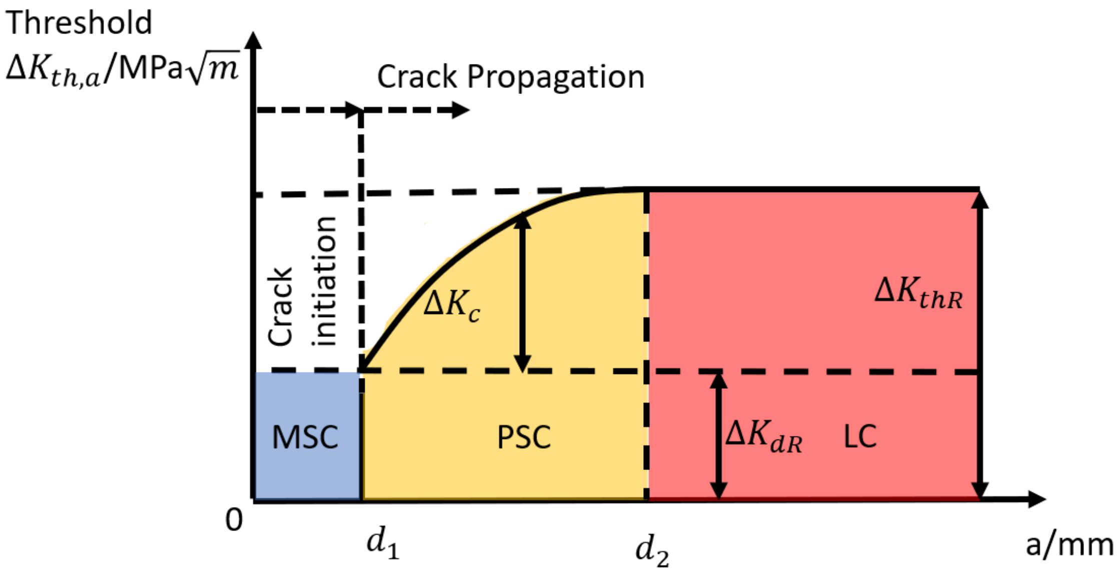

Figure 2.16. Threshold of stress intensity factor ranges with crack size.

For an MSC, only when the applied stress range is larger than the plain fatigue limit range $\Delta\sigma_{eR}$, the nucleated crack can break through the microstructural grain barriers and continue to grow as a PSC, whereby the ΔK_{dR} as the intrinsic threshold is dependent on the plain fatigue limit and the transition between MSC and PSC (d_1), as shown in (2.41)

$$\Delta K_{dR} = Y \Delta\sigma_{eR}\sqrt{\pi d_1} \tag{2.41}$$

where Y is the geometrical correction factor which can be assumed as 0.65 as in Chapetti's article [82]. However, in [71], researchers assumed a semi-ellipse crack with a specific aspect ratio a/b, where a (initial crack length) is the half length of the minor axis and b is the half length of the major axis, and proposed that the value of Y should be dependent on the aspect ratio. For example, it can be assumed as 0.746 if the aspect ratio is 0.8. The value of d_1 is defined as the strongest microstructural barrier of the material, such as the ferrite grain size in ferrite-perlite microstructure, but for engineering applications it is difficult to determine the value without experiments, and it is commonly taken to be the average grain size of the material.

In PSC region, the ΔK_C changes as the extrinsic component of ΔK_{th} increases from ΔK_{dR} to ΔK_{thR}, as shown in Figure 2.16. The value of $\Delta K_{th,a}$ can be obtained by (2.42).

$$\Delta K_{th,a} = \Delta K_{dR} + (\Delta K_{thR} - \Delta K_{dR})[1 - e^{-k(a-d_1)}] \tag{2.42}$$

where, k is material constant to fit the curve in (2.42), and can be calculated as (2.43).

$$k = \frac{1}{4d_1}\frac{\Delta K_{dR}}{\Delta K_{thR} - \Delta K_{dR}} \tag{2.43}$$

Finally, when the size of the crack is larger than d_2, the threshold is constant at ΔK_{thR}.

2.7.3 Long Crack Growth

The predominant focus in fracture mechanics lies in the analysis of long crack growth, since the length of such cracks comprises the majority of the total propagation. In typical fracture mechanics, various parameters are utilized to characterize the energy release rate or stress amplitude at the crack tip, including J-integral, Stress Intensity Factor (SIF), and Energy-release Rate (*G*). The prevalent approach for simulating crack propagation and computing these parameters is Linear Elastic Fracture Mechanics (LEFM). Irwin [83] developed a solution for stress distribution surrounding the crack tip in an infinite plate as:

$$\begin{aligned}
\sigma_{xx} &= \frac{\sigma_\infty\sqrt{\pi a}}{\sqrt{2\pi r}}\cos\frac{\theta}{2}(1 - \sin\frac{\theta}{2}\sin\frac{3\theta}{2}) \\
\sigma_{yy} &= \frac{\sigma_\infty\sqrt{\pi a}}{\sqrt{2\pi r}}\cos\frac{\theta}{2}(1 + \sin\frac{\theta}{2}\sin\frac{3\theta}{2}) \\
\tau_{xy} &= \frac{\sigma_\infty\sqrt{\pi a}}{\sqrt{2\pi r}}\cos\frac{\theta}{2}\sin\frac{\theta}{2}\cos\frac{3\theta}{2}
\end{aligned} \tag{2.44}$$

where, σ_∞ is the remotely applied stress and r and θ are two axes in a circular coordinate system, a is the crack length as shown in Figure 2.17. When θ=0, it becomes $\sigma_{yy} = \frac{\sigma_\infty\sqrt{\pi a}}{\sqrt{2\pi r}}$, and note that all three stress equations contain the same expression, $\sigma_\infty\sqrt{\pi a}$. Irwin first used this to describe the stress state at the tip of the crack. Therefore, under static loading, the stress intensity factor for cracked structures can be determined as:

$$K = Y\sigma\sqrt{\pi a} \tag{2.45}$$

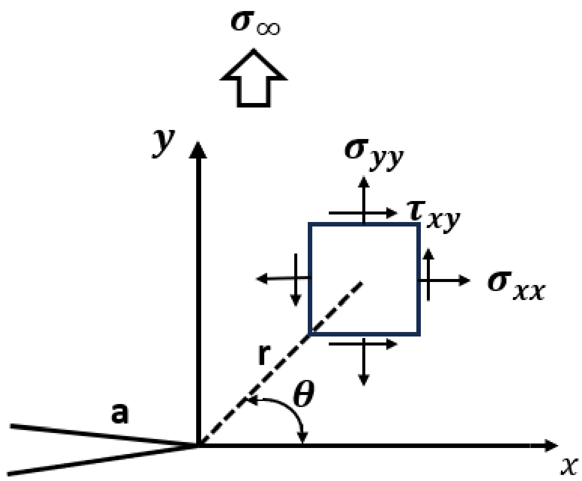

Figure 2.17. Stress components on a point around the crack length a.

Under cyclic loading, crack propagation is determined by the range of stress intensity factor:

$$\Delta K = Y(\sigma_{max} - \sigma_{min})\sqrt{\pi a} = Y\Delta\sigma\sqrt{\pi a} \tag{2.46}$$

The crack growth rate ($\frac{da}{dN}$) defined as increment crack growth per load cycle can be related to the ΔK as shown in Figure 2.18, where the long crack propagation can be divided into three regions. In the first region, the crack can propagate only when the stress intensity range is larger than the threshold of long crack. In the second region, the crack growth rate is stable and follows linearly with the ΔK om log-log plot and can be defined by Paris Law [84]:

$$\frac{d_a}{d_N} = C(\Delta K)^m \tag{2.47}$$

where, *C* and *m* are material constants.

In the third region, K_{max} finally approaches a critical value and ΔK achieves a critical value ΔK_{CR}. The crack propagates rapidly, and the crack growth rate is unstable.

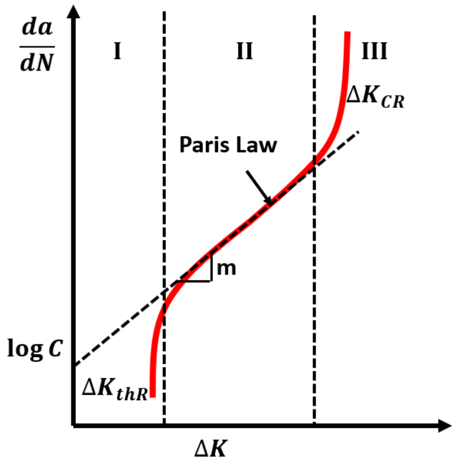

Figure 2.18. Crack growth rate with stress intensity range.

In LEFM, the energy release rate, *G* represents the rate at which potential energy is released from a elastic structure as a crack propagates. *G* is given by:

$$G = \frac{\pi\sigma^2 a}{E} \tag{2.48}$$

For a single fracture mode, the SIF can be related to *G* by:

$$G = \frac{K^2}{E} \tag{2.49}$$

The J-integral is one of the most widely used parameters in fracture mechanics. It represents an integral equation that quantifies the energy released per unit area as the crack surface extends. In the context of the first law of thermodynamics, when the system is in a static state at ambient temperature, the work performed by external forces equals the sum of the mechanical strain energy and the dissipated mechanical energy resulting from crack growth. By integral calculation [85], the J-integral can be determined. The J-integral can be applied in both linear elastic and elastic-plastic materials. It depends on quantifying the energy release rate, distinguishing it from SIF which can be obtained through different modes and possess directionality.

2.7.4 Effect of Stress Intensity Ratio, *R*

The crack growth rate may depends to the stress ratio, such that with same ΔK, an increase in the stress intensity ratio may cause a larger crack growth rate. The Paris Law, therefore, needs to be corrected for different stress ratios. One of the most widely used methods is the Walker equation [33]:

$$\Delta K_{eq} = \frac{\Delta K}{(1-R)^{1-\gamma}} \tag{2.50}$$

where, ΔK_{eq} is the equivalent stress intensity range when the stress intensity ratio $R = -1$.

The crack closure and opening concept was proposed by Elber [86] who suggested that cracks could propagate only when the corrected stress intensity range was larger than the crack opening stress intensity factor.

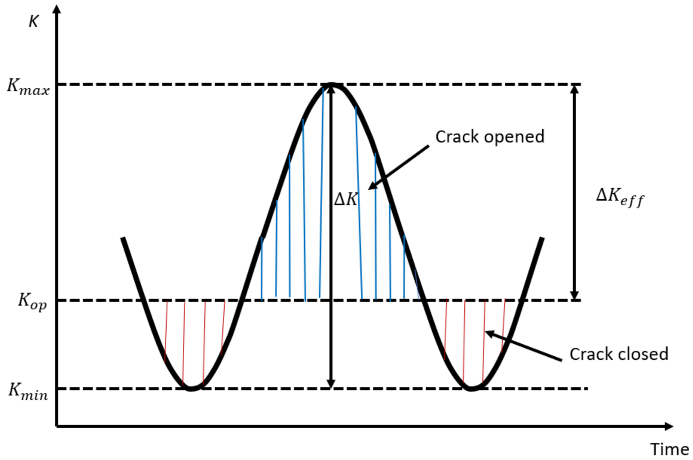

Figure 2.19. Definition of crack closure and opening.

In the crack closure concept, the effective stress intensity factor range (ΔK_{eff}) is obtained from ΔK by the U ratio of ΔK_{eff} and ΔK as:

$$U = \frac{\Delta K_{eff}}{\Delta K} = \frac{K_{max} - K_{op}}{\Delta K} \tag{2.51}$$

where, K_{op} is the crack opening stress intensity factor. In addition, according to the study of Elber, the value of U depends on R [87] and an improved function to relate U to R was proposed by Newman [88]. The effective stress intensity factor can be treated as a function of ΔK and R and the traditional $\frac{d_a}{d_N}$ against ΔK curves with different R can be replaced by a main curve.

Kujawski [89] addressed the crack closure effect by correlating the fatigue crack growth rate with a variable stress ratio R. The driving force for crack growth may depend on the material properties, temperature, and environment. For example, in a ductile material the driving force is dominated by ΔK, but in a brittle material it is controlled by K_{max}. Kujawski proposed a new form of crack driving force, K^*, combining ΔK and K_{max}:

$$K^* = (K_{max})^{\alpha}(\Delta K^+)^{1-\alpha} \tag{2.52}$$

where α is a correlation parameter, $\Delta K^+ = \Delta K$ when R≥ 0 and $\Delta K^+ = K_{max}$ when R< 0.

On this basis, the stress intensity factor range ΔK in the Paris equation is replaced by K^*, and the effect of R is incorporated by:

$$\Delta K = K^*(1-R)^{\alpha} \qquad \text{For } R > 0 \tag{2.53}$$

$$\Delta K = K^*(1-R) \qquad \text{For } R < 0 \tag{2.54}$$

and the Paris law is correlated as:

$$\frac{da}{dN} = C_{R=0}[\frac{\Delta K}{(1-R)^{\alpha}}]^{m_{R=0}} \qquad \text{For } R > 0 \tag{2.55}$$

$$\frac{da}{dN} = C_{R=0}[\frac{\Delta K}{(1-R)}]^{m_{R=0}} \qquad \text{For } R < 0 \tag{2.56}$$

2.7.5 Crack Tip Plasticity

Due to the high stress concentration induced by the crack tip, even though the remote stress is low, the high value of stress around the crack tip may cause plasticity. LEFM is only valid if the small scale yielding criterion is satisfied such that the crack tip plastic zone is much smaller than the crack size. Therefore, it is important to determine the plastic zone size. Irwin [90] assumed that in a plastic zone around the crack tip, the stress equals the yield stress of the material, and outside the plastic zone, the stress distribution is still elastic, as shown in Figure 2.20. In Irwin's model, the crack tip plastic zone is R_p and to calculate the value of R_p, a fictitious crack tip is proposed at x=η. The force represented by area A should be equal to the force represented by area B, so that the effect of the elastic-plastic stress zone around the real crack length a is also equivalent to that of the elastic stress zone around the fictitious crack length $a + \eta$ [91].

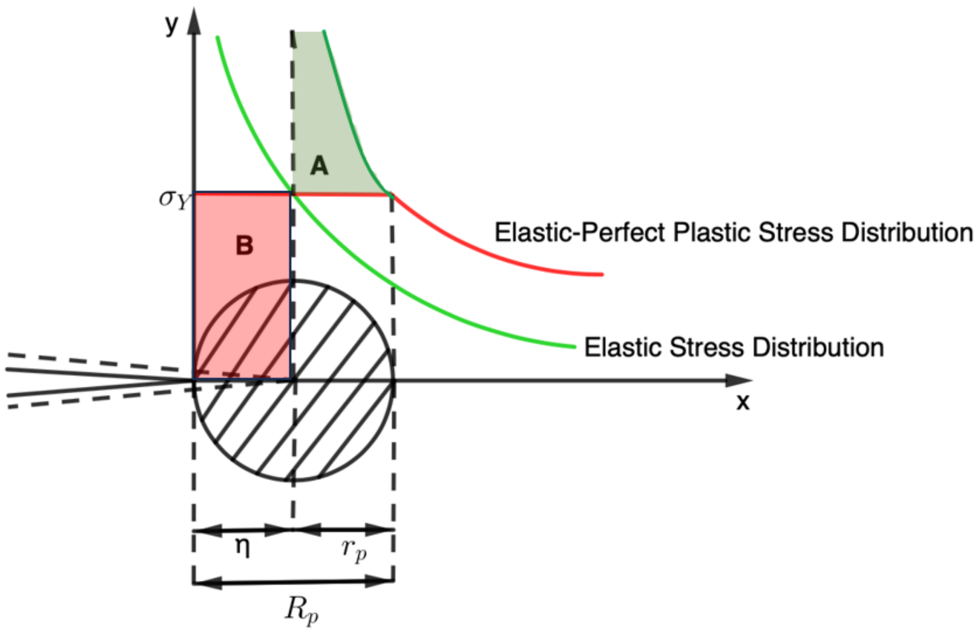

Figure 2.20. Crack tip plasticity region.

To calculate η, assuming the area of A is equal to that of B, an equation can be proposed as:

$$\int_0^{r_p} \sigma_{yy} dx - {\sigma_Y}^* r_p = \eta {\sigma_Y}^* \tag{2.57}$$

$$\sigma_{yy} = \frac{K_I}{\sqrt{2\pi x}}$$

For two conditions:

$$\sigma_Y{}^* = \begin{cases} \sigma_Y, & plane\ stress \\ \dfrac{1}{1-2\nu}\sigma_Y, & plane\ strain \end{cases} \tag{2.58}$$

Then r_p is solved as:

$$r_p = \frac{1}{2\pi}(\frac{K_I}{\sigma_Y{}^*})^2 \tag{2.59}$$

Meanwhile, we can also get $\eta = r_p$, and hence,

$$R_p = \eta + r_p = \frac{1}{\pi}(\frac{K_I}{\sigma_Y{}^*})^2 \tag{2.60}$$

Based on this theory, concepts of effective crack length (a_{eff}) and adjusted stress intensity factor were proposed by Irwin, who assumed the rule of small-scale plastic crack growth is the same as that in LEFM. Assuming inducing an effective crack length which equals the physical crack length plus the half size of the plastic zone (a+r_p):

$$K_{IP} = \sigma\sqrt{\pi a_{eff}} = \sigma\sqrt{\pi(a + r_p)} = \sigma\sqrt{\pi(a + \frac{1}{2\pi}(\frac{K_I}{\sigma_Y{}^*})^2)} \tag{2.61}$$

where, K_{IP} is the stress intensity factor determined from plasticity.

The shape plastic zone is different for different yield criteria and plane stress case or plane strain case. Based on (2.44), three principal stresses can be calculated as:

$$\begin{gathered} \sigma_1 = \frac{K_I}{\sqrt{2\pi r}}\cos\frac{\theta}{2}[1 + \sin\frac{\theta}{2}] \\ \sigma_2 = \frac{K_I}{\sqrt{2\pi r}}\cos\frac{\theta}{2}[1 - \sin\frac{\theta}{2}] \\ \sigma_3 = \begin{cases} 0, & Plane\ stress \\ 2v\dfrac{K_I}{\sqrt{2\pi r}}\cos\dfrac{\theta}{2}, & Plane\ strain \end{cases} \end{gathered} \tag{2.62}$$

According to the Tresca yield criterion and von Mises yield criterion, the plastic zone estimated by plane stress and plane strain can be shown in Figure 2.21 and Figure 2.22.

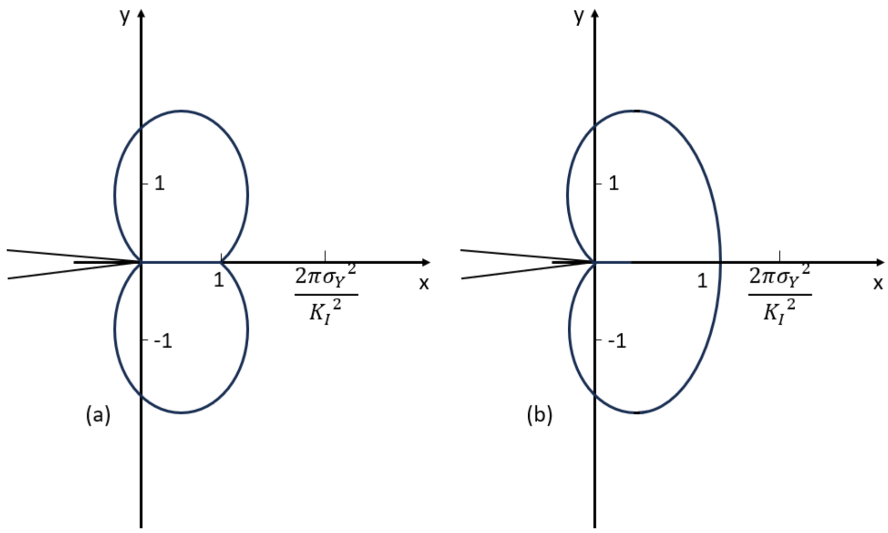

Figure 2.21. Plastic zone based on Plane stress (a) Tresca yield criterion (b) Von Mises criterion.

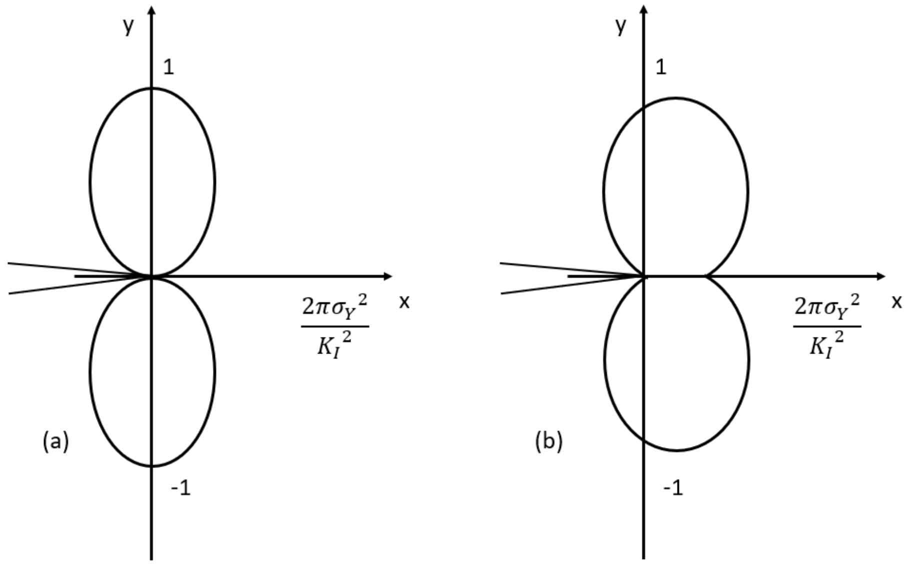

Figure 2.22. Plastic zone based on Plane strain (a) Tresca yield criterion (b) Von Mises criterion.

Chapter 3 Plasticity Modelling

3.1 Monotonic Stress-strain Curve

The monotonic stress-strain curve is a major fundamental graphical representation within the field of materials science and engineering to define the mechanical characteristics of materials under external forces. Materials deform under external forces in two main ways: elastic deformation and plastic deformation, as shown in Figure 3.1. Elastic deformation occurs when the stress is less than the yield stress, σ_Y and refers to the ability of a material to return to its original shape and size after being subject to a certain amount of deformation from external forces, making the process of elastic deformation reversible. In the elastic region, the response of strain to the tensile stress is linear, obeying Hook's law, therefore, the elastic deformation can be represented by a linear segment with a slope equal to the elastic modulus, E as shown in Figure 3.1. Plastic deformation occurs when the stress exceeds the yield stress, causing a material to be unable to fully return to its original shape and size. Unlike elastic deformation, plastic deformation is irreversible and results in permanent changes to the shape of the material. The response is nonlinear in the plastic region, and the strain in the curve increases faster than the stress, known as strain hardening.

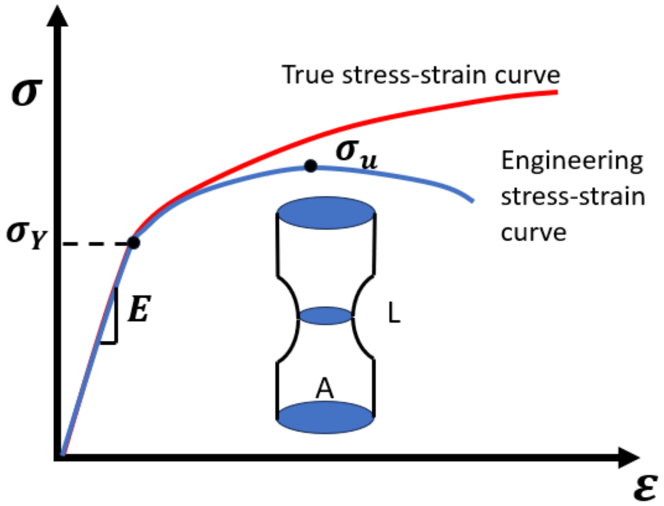

Figure 3.1. True stress-strain curve and engineering stress-strain curve.

The monotonic stress-strain curve is generated by tensile test. Engineering stress and strain are calculated based on the original specimen geometry as:

$$\sigma = \frac{P}{A_0} \tag{3.1}$$

$$\varepsilon = \frac{L - L_0}{L_0}$$

where, A_0 and L_0 are the cross-sectional area and length of the original specimen and L and A are the transient length and cross-sectional area, P is the tensile load.

However, since the length and cross-sectional area of the specimen are constantly changing during the tensile test, the engineering stress and strain cannot accurately reflect the true stress strain responses of the material during deformation. Therefore, the concept of true stress and strain is proposed. Since the volume of the specimen is constant, as $LA = L_0 A_0$, the true stress and strain can be calculated from the engineering stress and strain as:

$$\varepsilon_{true} = \ln(1 + \varepsilon) \tag{3.2}$$

$$\sigma_{true} = \sigma(1 + \varepsilon)$$

The difference between the engineering stress and strain and the true stress and strain is small unless the large deformation is considered. Therefore, in this thesis, only engineering stress and strain are considered.

3.2 Bauschinger Effect

The stress-strain response in the loading process is described by the line OAB in Figure 3.2. After extension to point B, the material is unloaded, and reloaded in the reverse direction to the opposite plastic region, shown as the BCD curve. After tensile or compressive deformation, the reversed load may cause the yield strength of the material to be lower than in continuous deformation. Here, the yield stress at the reverse yield point C is decreased to $\sigma_Y{}'$, compared with the tensile yield stress at point A. This phenomenon is the Bauschinger effect. To quantify the Bauschinger effect, the Bauschinger effect factor (BEF) is proposed to define the ratio of the reversed yield stress to the initial yield stress, which can be a function of plastic strain [92].

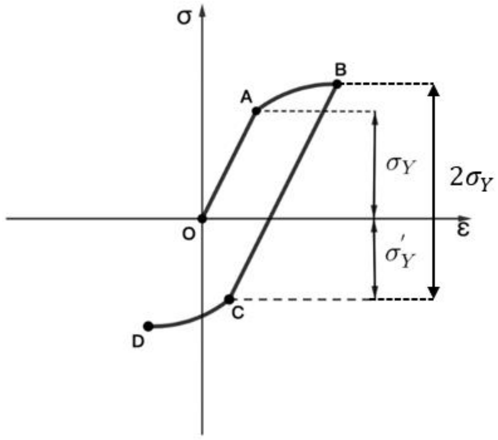

Figure 3.2. Engineering stress-strain curve with Bauschinger effect.

3.3 Cyclic Hardening and Softening of Metallic Materials

The stress-strain curve of a material under cyclic loading is called the cyclic stress-strain curve. This plays a vital role in describing the stress-strain behaviour of a structure under cyclic loading. When the stress-strain response on the material is within the elastic region of the material, there is no plasticity induced and, after unloading, no residual strain. However, when the external load on the material causes plastic deformation, the repeated cyclic loading can form a hysteresis loop, as shown in Figure 3.3.

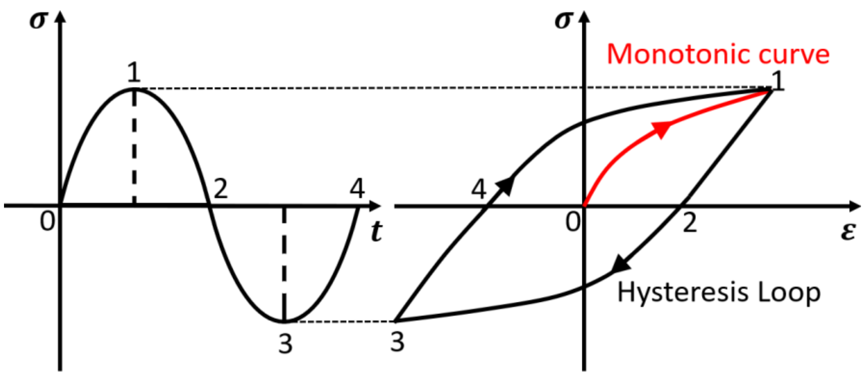

Figure 3.3. Stress-strain hysteresis loop for cyclic loading.

The shape of the hysteresis loop depends on the Bauschinger effect of the material and when cyclic load is applied to a material, causing plastic deformation, the plastic flow behaviour of the metal can be changed due to the repeated plastic deformations. This phenomenon can either increase or decrease the ability of material to resist deformation, known as cyclic hardening and softening.

The cyclic hardening or softening properties of materials can play a critical role in calculation of the fatigue life of cyclically loaded structures. Therefore, a large amount of work has been conducted to measure these properties. Manson and Hirschberg described the hardening or softening behaviour by the ratio of the ultimate tensile strength to the yield stress. If the ratio is larger than 1.4, the behaviour of metal is cyclic hardening and if the ratio is less than 1.2, the behaviour is cyclic softening[93]. Lopez and Fatemi tried to predict the cyclic softening behaviour from the ultimate strength and the hardness of steels. They found approximate 90% of steels with greater than 920 MPa tensile strength and 250HB hardness had softening behaviour, and proposed a method to predict the cyclic stress-strain behaviour from the monotonic stress-strain curve [94].

The behaviour of cyclic hardening and softening materials differs under stress-controlled cyclic loading and strain-controlled cyclic loading.

- Under stress-controlled cyclic loading, for cyclic hardening material, the strain range decreases, but for cyclic softening material, the strain range increases.
- Under strain-controlled cyclic loading, for cyclic hardening material, the stress range increases, but for cyclic softening material, the stress range decreases.

Commonly, the behaviour of cyclic hardening or softening of materials is significant at the beginning of the fatigue test, then gradually weakens and becomes stable. This phenomenon is seen in the shape of the hysteresis loop. The steady cyclic stress-strain curve of a material describes the stress-strain relationship when the transient behaviour reaches a relatively stable state, by connecting the cusps of the steady hysteresis loops at various strain-controlled levels, as shown in Figure 3.4.

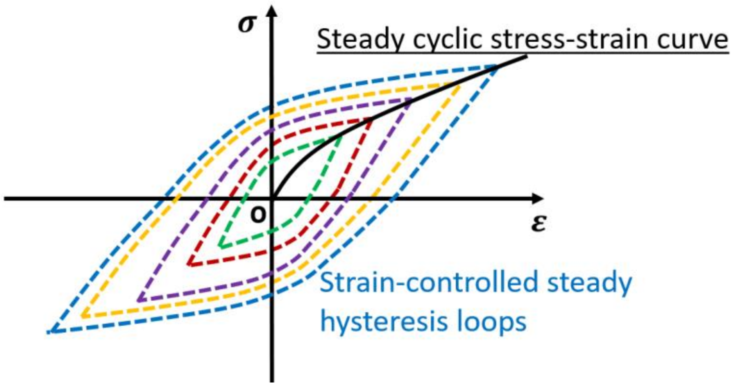

Figure 3.4. Steady cyclic stress-strain curve.

In contrast to the monotonic stress-strain curve, significant differences can be found in the two kinds of cyclic steady stress-strain curves as shown in Figure 3.5 where, for cyclic hardening material, the steady cyclic stress-strain curve is higher than the monotonic curve, but for cyclic softening material, the steady cyclic curve is lower than the monotonic curve. However, whether the material is cyclic hardening or softening, Young's modulus of the material in the elastic region of the cyclic curves are the same as the slope in the monotonic curve.

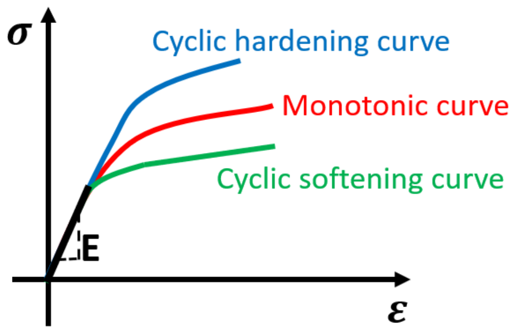

Figure 3.5. Cyclic steady stress-strain curves with monotonic stress-strain curve.

Compared to the steady cyclic stress-strain curve, the transient cyclic stress-strain curve is more complex because the shape of the hysteresis loop varies with the number of cycles until it stabilizes. To generate the transient cyclic stress-strain curve with different numbers of cycles, the yield stress is adjusted to describe the cyclic hardening and softening behaviour in each cycle. The Young's modulus and the curve in the plastic region can be assumed to be constant. As the number of cycles increases, the yield stress is adjusted to increase in hardening materials or decrease in softening materials [95].

3.4 Shakedown and Ratchetting

When subjected to cyclic loading above the yield point, a structure will not fail in the first load cycle as long as the induced plastic deformation is lower than the static failure threshold. However, additional plastic deformation may accumulate with each load cycle, leading to an expansion of the plastic zone. This increment of plastic deformation can eventually cause failure, which is commonly named as ratcheting, as shown in Figure 3.6 (a). If no increment plastic deformation is induced, two types of shakedown may occur: elastic shakedown and plastic shakedown.

For elastic shakedown, after the first few cycles, the structure exhibits a purely elastic response throughout the loading cycles in Figure 3.6 (b). In contrast, plastic shakedown occurs when the plastic deformation induced in the loading parts equals the reverse plastic deformation in the unloading parts within the cycle, resulting in a net zero plastic strain over subsequent cycles, as shown in Figure 3.6 (c).

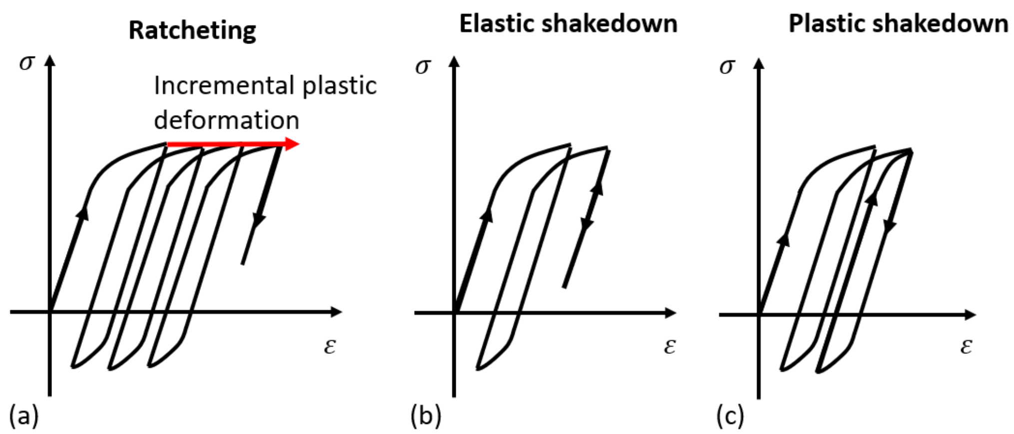

Figure 3.6. (a) Ratcheting response. (b) Elastic shakedown response. (c) Plastic shakedown response.

These states of structural responses under cyclic loading can occur under both thermo-mechanical load conditions and mechanical only conditions. For the situation of thermo-mechanical load, the Bree diagram can describe the states comprehensively where the structural responses are divided into different zones as pure elastic, elastic shakedown, plastic shakedown, ratcheting and plastic collapse. Through calculating the normalized cyclic thermal stress and the normalized constant mechanical stress, the unique zone for the states of structural responses can be obtained. For the conditions with both thermo-mechanical load and only mechanical loading, the states of structural responses can be determined by FEA as well. Based on the definition of these responses, the equivalent plastic strain is applied to be investigated in FEA to obtain the states as shown in Figure 3.7.

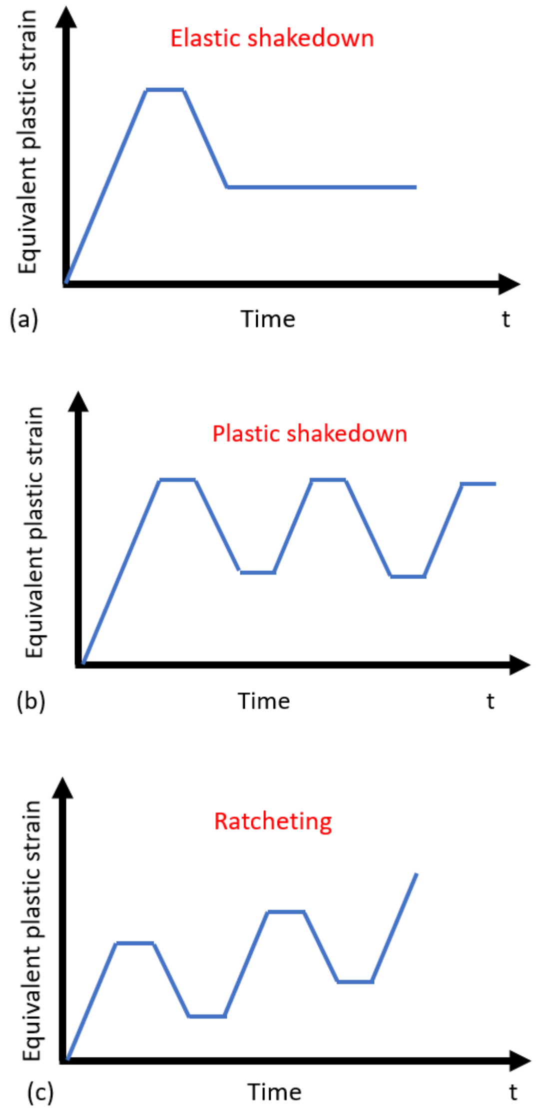

Figure 3.7. Time dependent equivalent plastic strain (a) Elastic shakedown (b) plastic shakedown (c) Ratcheting.

For elastic shakedown, as no plastic strain is induced after the first few cycles, therefore, the equivalent plastic strain is constant with time, as shown in Figure 3.7 (a). For plastic shakedown, the net plastic strain is zero, therefore, no additional equivalent plastic strain is induced, but for each loading and unloading process, the equivalent plastic strain changes as shown in Figure 3.7 (b). For ratcheting, the net equivalent plastic strain increases for each cycle as shown in Figure 3.7 (c). It is necessary to determine the states of structural responses by FEA since the residual stress distribution after the first cycle may be redistributed, which will be shown in the following section.

3.5 Constitutive Model

Constitutive model is a major area of interest within the field of materials science and mechanical engineering. It has been the subject of studies in describing the mechanical behaviour of materials under various loadings by a mathematical framework that relates stress and strain. The constitutive model plays a critical role in ensuring the accuracy of numerical analysis, so it is essential to use constitutive models tailored to specific materials. Since materials exhibit different characteristics on cyclic hardening or softening, a number of constitutive models are available. In this section, materials that dominate selection in pressure vessel manufacture are discussed. Among these materials, cyclic hardening is the most commonly investigated material behaviour under cyclic loading. According to the different hardening rules, constitutive models can be developed as isotropic hardening model and kinematic hardening model, and the most significant difference between these two constitutive modes is the evolution of the yield surface.

3.5.1 Isotropic Hardening Model

For the isotropic hardening model, as the post-yield load is increased, the yield surface remains the same shape, but expands with increasing stress as shown in Figure 3.8, where the yield surface expands from the initial red curve to the final blue curve and the value of yield stress also increases from σ_Y to $\sigma_Y{}'$ by adding σ_{iso}.

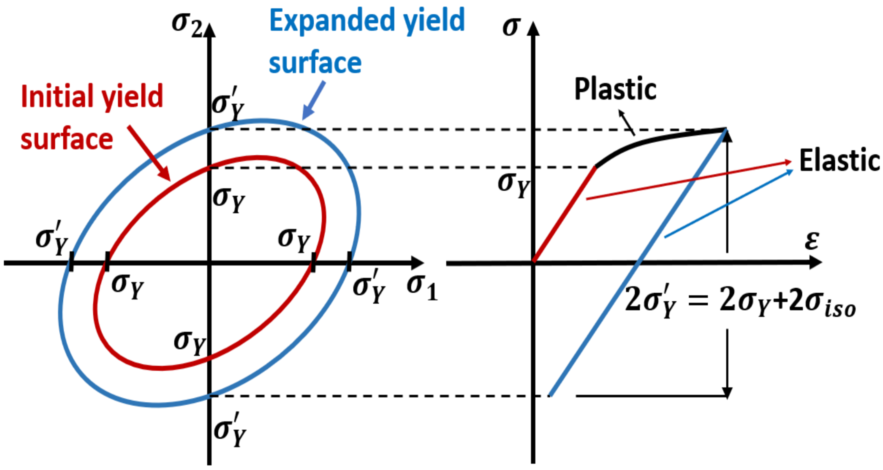

Figure 3.8. Yield surfaces in isotropic hardening.

The yield function is applied to describe the yield surface, as $f(\sigma) - K_h$, where K_h is a hardening parameter representing the expanded part of the yield surface. If only isotropic hardening model is applied in calculating the cyclic stress-strain loop, the hysteresis loop will expand due to the continuum expansion of the yield surface, as shown in Figure 3.9 (a). This behaviour is unrealistic. If the objective of FEA is to calculate the stress-strain response under static loading, or to predict the residual stress distribution after the first cycle only under without the consideration of the Bauschinger effect, isotropic hardening is acceptable. However, to predict the structural response under the continuum cyclic loading, the isotropic hardening model may not suitable, and the kinematic hardening in the Section 3.5.2 may be a more accurate selection.

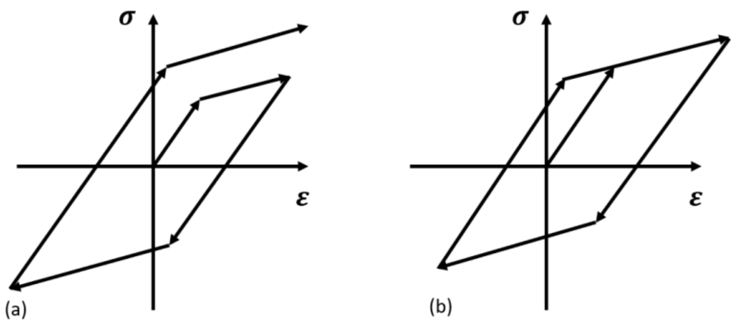

Figure 3.9. Cyclic stress-strain curve simulated by (a) Bilinear isotropic hardening model. (b) Bilinear kinematic hardening model.

3.5.2 Kinematic Hardening Model

In isotropic hardening, only the expansion of the yield surface is considered and the shape of the yield surface is constant. However, due to the Bauschinger effect, the yield surface cannot remain the same shape as shown in Figure 3.10 where the initial yield surface remains the same size, but transforms from the red curve to the blue curve. The yield function for the kinematic hardening model is then $f(\sigma - \alpha)$, where α is the back stress tensor, applied to describe the transformation of the yield surface. In the linear kinematic hardening material model proposed by Prager [96], the back stress tensor was related to the plastic strain as:

$$d\alpha = \frac{2}{3} C_h d_{\varepsilon_{pl}} \tag{3.3}$$

where, C_h is the initial hardening modulus and $d_{\varepsilon_{pl}}$ is the plastic strain tensor.

In FEA, two types of linear kinematic hardening models are included which are bilinear kinematic hardening model and multilinear kinematic hardening model, as shown in Figure 3.11. The distinction between them is that for the bilinear kinematic hardening model, the plastic curve after the yield point is described by a straight line with a tangent modulus, but for the multilinear kinematic hardening model, the plastic curve is represented by several lines. The accuracy of these two models is dependent on how well they fit the experimental plastic response of the material.

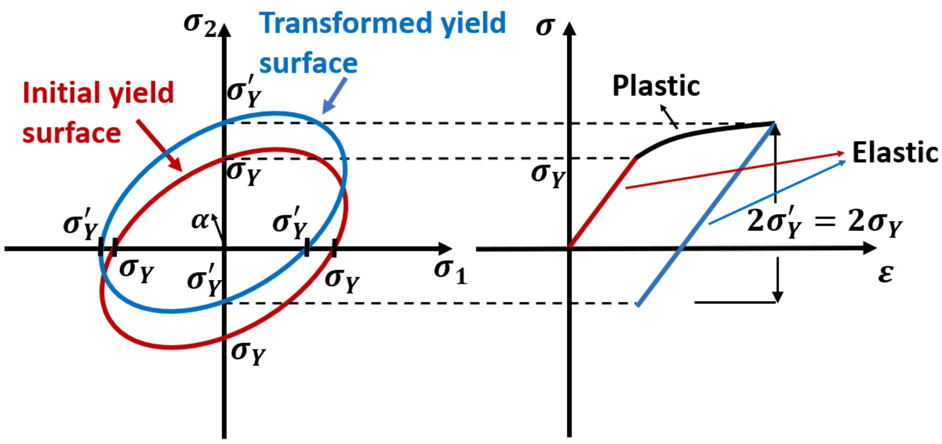

Figure 3.10. Yield surfaces in kinematic hardening model.

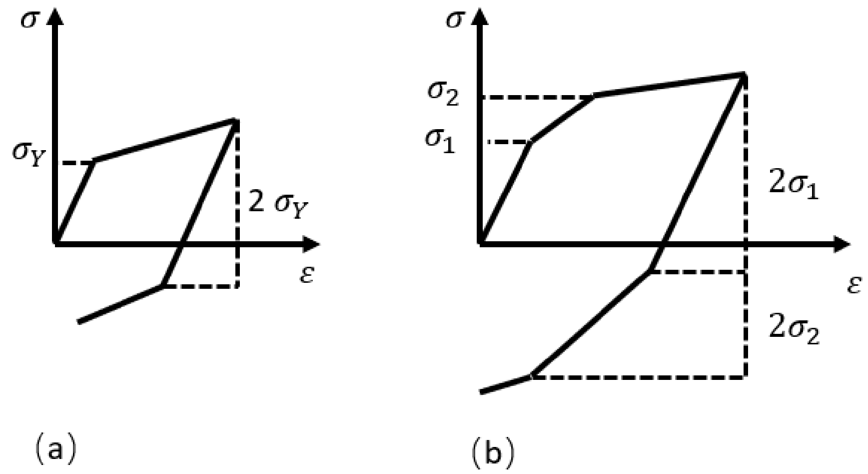

Figure 3.11. Linear kinematic model (a) Bilinear kinematic model (b) Multilinear kinematic model.

The bilinear and multilinear kinematic hardening models are commonly used to accurately represent the monotonic stress-strain curve and effectively simulate the stress and strain response following the first loading and unloading cycle. However, a limitation of the linear hardening model is its inability to predict ratcheting behaviour under uniaxial loading conditions as shown in Figure 3.9 (b) since the $d\alpha$ in (3.3) is proportional to the $d_{\varepsilon_{pl}}$ which means the back stress increases with the increase of plastic strain. Even under large cyclic loading conditions there is still no incremental plastic deformation, only plastic shakedown may occur.

The cyclic hardening behaviour of material is commonly strong at the first few loops, then gradually weakens and stabilizes until a hysteresis loop occurs. To reflect this phenomenon, Armstrong and Frederick [97] improved the Prager's model by proposing a fading memory term as:

$$d\alpha = \frac{2}{3} C_h d_{\varepsilon_{pl}} - \gamma_h \alpha d_{pl,acc} \tag{3.4}$$

where, γ_h is used to define the rate where the hardening modulus starts decreasing and $d_{pl,acc}$ is an increment of accumulated plastic strain that represents the development of plastic strain. With the development of the plastic strain and the accumulation of the plastic strain, the value of $d_{pl,acc}$ increases to modify the back stress.

By integrating the (3.4) with respect to $d_{\varepsilon_{pl}}$, the back stress can be calculated as:

$$\alpha = \varphi \frac{C_h}{\gamma_h} + \left(\alpha_0 - \varphi \frac{C_h}{\gamma_h}\right) \exp\left[-\varphi \gamma_h (\varepsilon_{pl} - \varepsilon_{pl0})\right] \tag{3.5}$$

where, φ defines the flow direction, for tension, φ is 1 and for compression, it is -1. Assuming zero initial plastic strain and zero initial back stress, the back stress becomes:

$$\alpha = \frac{C_h}{\gamma_h}\left[1 - \exp(-\gamma_h \varepsilon_{pl})\right] \tag{3.6}$$

Finally, through (3.6), for uniaxial loading case and non-initial plastic strain, the stress based on the nonlinear kinematic hardening can be calculated as:

$$\sigma = \sigma_Y + \frac{C_h}{\gamma_h}(1 - e^{-\gamma_h \varepsilon_p}) \tag{3.7}$$

For the case of cyclic loading, two cusps of the hysteresis loops shown in Figure 3.3 are applied, and the equation with stress amplitude σ_a and plastic strain amplitude ε_{ap} is as:

$$\sigma_a = \sigma_Y + \frac{C_h}{\gamma_h} \tanh\left(\gamma_h \varepsilon_{ap}\right) \tag{3.8}$$

According to the nonlinear kinematic hardening model proposed by Armstrong and Frederick, the saturation value of the back stress is given by C_h/γ_h. However, for some realistic materials, no saturation effect is observed with plastic strain. Therefore, Chaboche improved this model by introducing the back stress α through the superposition of M terms in (3.9) and for describing cyclic stress-strain curves. (3.8) then becomes:

$$\sigma_a = \sigma_Y + \sum_{i=1}^{M} \frac{C_i}{\gamma_i} \tanh(\gamma_i \varepsilon_{ap}) \tag{3.9}$$

The Chaboche kinematic model shown in (3.9) is applied in the following chapters to fit the cyclic stress-strain curves. However, when applying the Chaboche model to cyclic loading conditions, it has a property that the mean back stress tends to relax to zero to make the stress distribution stable [98-100]. This behaviour is purely mathematical. Actual material behaviour can show redistribution phenomena such as ratcheting and mean stress relaxation, which the standard Chaboche model may not properly predict. Consequently, numerous modifications to the Chaboche model have been proposed to capture these phenomena [101]. Therefore, for accurately capturing stress redistribution after autofrettage, more advanced models should be employed. While the Chaboche model can still provide a preliminary estimation, caution is advised in interpreting the results. The predictions may either be overly conservative, overestimating the redistribution, or non-conservative, underestimating it. This depends on the ratio between the initial yield stress and C_h/γ_h in the model, as well as the loading ratio of external loading.

3.5.3 Mixed Hardening Model

Cyclic hardening behaviour of most materials can be described by the superposition of isotropic and kinematic hardening rules, as shown in Figure 3.12, where the initial yield surface expands and moves. The Chaboche kinematic hardening model mentioned in Section 3.5.2 can be applied for the motivation of the yield surface. In addition, the expansion of the yield surface can be described by the nonlinear isotropic hardening rule as:

$$dR = b(R_\infty - R)dp \tag{3.10}$$

where, R_∞ is the saturation value of the yield surface and b is the speed of stabilization.

If R_∞ is negative, the initial yield stress will be reduced with plastic deformation which means that material softens. If it is positive, the initial yield stress will be increased with plastic deformation and material behaviour will harden.

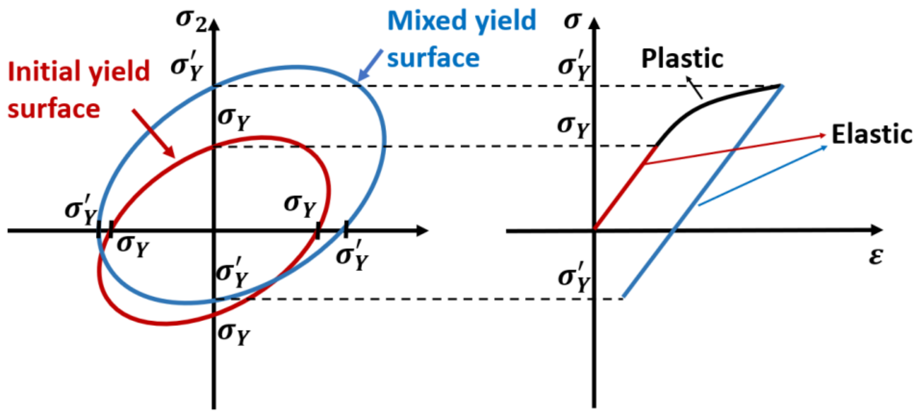

Figure 3.12. Yield surfaces in mixed kinematic hardening model.

The mixed kinematic model of the Chaboche kinematic model and the nonlinear isotropic model can be expressed as:

$$\sigma_a = k + R_\infty(1 - e^{-b.p}) + \sum_{i=1}^{M} \frac{C_i}{\gamma_i} \tanh(\gamma_i \varepsilon_{ap}) \tag{3.11}$$

where, k is the initial yield stress and p is the accumulated plastic strain by the integral calculation of the incremental plastic strain.

Assume the monotonic stress-strain curve and the stable cyclic stress-strain curve are obtained by tests, the following procedures can be applied to determine the parameters in the mixed hardening model.

- The initial yield stress, k, can be assumed to be constant, the value of $k + R_\infty(1 - e^{-b.p})$ should be adjusted as small as possible in the stable cyclic stress-strain curve.
- The parameters included in the Chaboche kinematic hardening model (M=3) can be determined based on decomposed back stresses α_1 and α_2 which have the same strain ranges as the stable loop as shown in Figure 3.13 by:

$$\frac{C_1}{\gamma_1} + \frac{C_2}{\gamma_2} + \sigma_Y = \sigma_a - C_3 \cdot \varepsilon_{ap} \tag{3.12}$$

where, γ_1 is typically determined between 2000 and 10000, and the experimental data of plastic strain range, $\Delta\varepsilon_p$in the domain 0.02% to 1% is employed to obtain C_1, C_2 and γ_2 [102]. The third back stress α_3 can be linear and pass the original point [103].

- After determining the parameters in the kinematic model, the parameters included in the isotropic model can be obtained by plotting the normalized maximum stress as a function of *p*, as shown in Figure 3.14.

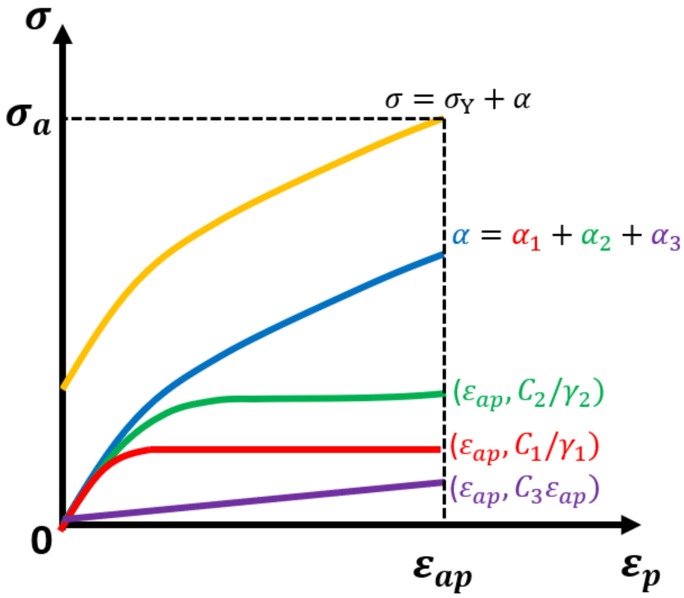

Figure 3.13. Parameters of Chaboche kinematic hardening model (M=3).

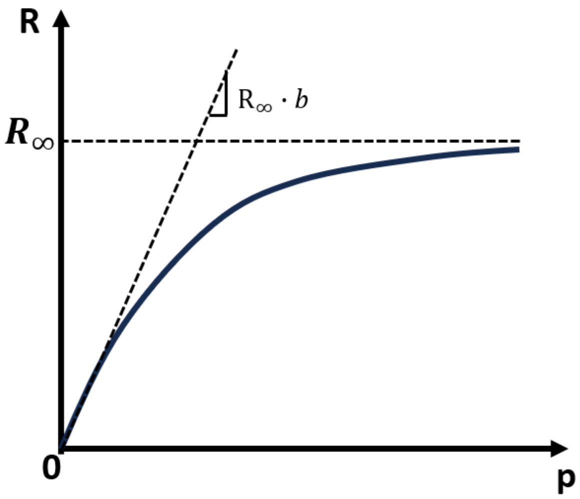

Figure 3.14. Parameters of nonlinear isotropic hardening model.

Chapter 4 Fatigue Life Assessment with Residual Compressive Stress

The fatigue life of components subject to repeated or cyclic loading can be enhanced by inducing compressive residual stress in regions prone to fatigue crack initiation and propagation. This can be achieved by several different mechanical processes, such as shot peening, laser peening, low plasticity burnishing, swaging and autofrettage [104-107] mentioned in Section 2.1. These processes result in a self-equilibrating residual stress system in the component at zero load, with compressive residual stress at critical locations. The resulting increase in fatigue life can be described in terms of *inter alia* the stress life analysis and fracture mechanics approaches to fatigue.

Traditionally, low cycle fatigue of components is assessed using the strain-life method, while high cycle fatigue is evaluated using the stress-life method. For autofrettaged components, high cycle fatigue is more common. Therefore, the stress-life method, which depends on linear elastic calculation of nominal stress at the point of investigation and fatigue data in the form of *S-N* curves, is employed. To account for notch effects, methods such as Neuber's rule, Peterson's method, and the Theory of Critical Distances (TCD) discussed in Section 2.4.2 are utilized. However, when a component has been subject to autofrettage prior to operation, the compressive residual stress changes the stress gradient at the notch. Consequently R varies over the characteristic length and the TCD approach is not directly applicable [108].

Therefore, methodology presented here offers a new approach the fatigue analysis of notched components with compressive residual stress. It combines smooth fatigue specimen *S-N* data, a fracture mechanics crack growth model, and Finite Element Analysis through the ANSYS SMART crack growth modelling tool and so on. The method uses three Finite Element Analysis, FEA, models as shown in Figure 4.1.

The first stage in the analysis is to determine the residual stress distribution in the component after autofrettage. This is done using FEA Model 1, which has an elastic-plastic material model based on a monotonic material stress-strain curve. The calculated residual stress distribution is then exported as an initial stress state to two other finite element models.

Model 2 is an elastic-plastic model based on a cyclic stress-strain curve. This is used to calculate the stress amplitude, σ_a, resulting from the combined applied pressure and residual stress, and mean stress correction is applied to determine the equivalent stress amplitude, σ_{ar}. The fatigue assessment point is identified as the location of the maximum value of σ_{ar}, where of crack initiation is assumed to occur.

Model 3 is used to analyse crack propagation from the identified initiation location using the ANSYS SMART crack growth tool. SMART is used to calculate stress intensity ranges with increasing crack length a with and without residual stress. A superposition method is then applied to calculate the stress intensity range for the applied pressure, ΔK_{app} and the residual stress SIF, K_{rs}, from which the effective stress intensity range, ΔK_{eff} is calculated.

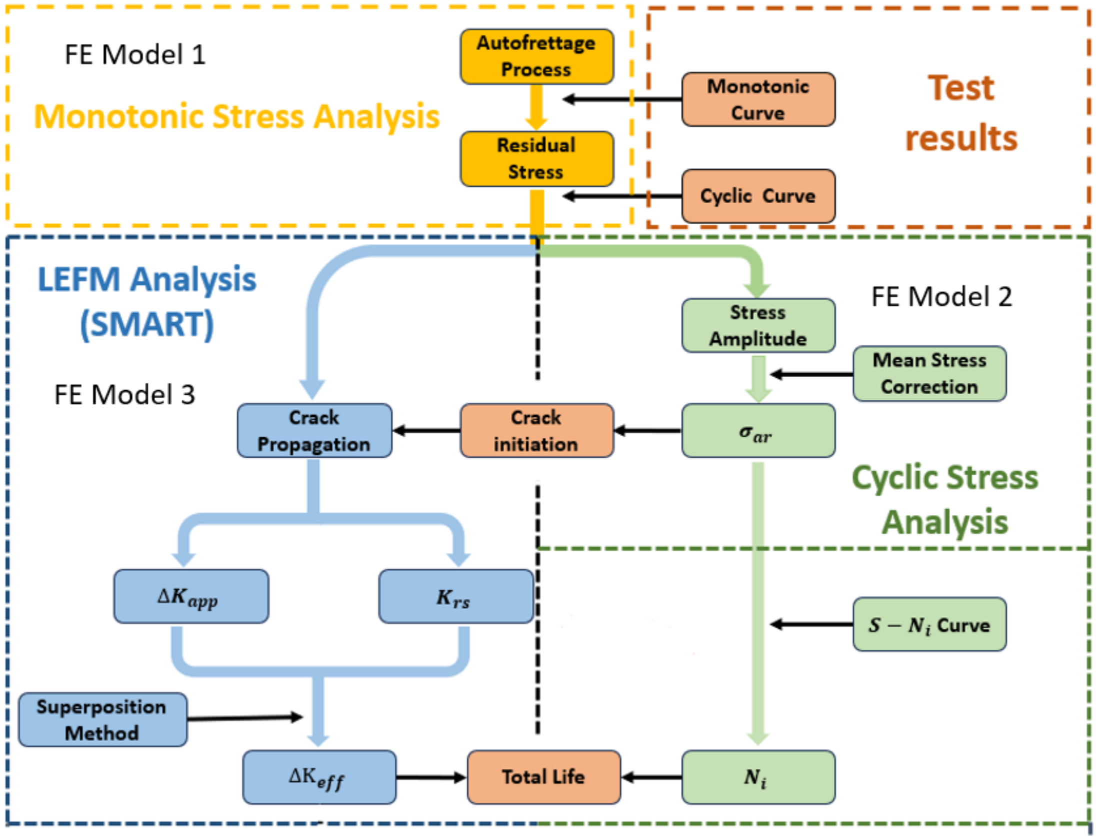

Figure 4.1. Flow diagram of analysis methodology.

For the life prediction, the methodology assumes a crack initiation length based on the material's average grain size. A stress-crack initiation life curve is then developed based on this assumed crack initiation length, allowing for the calculation of the crack initiation life. By adding the numerical results obtained from the crack propagation simulation, the method successfully predicts the total fatigue life of the specimens. Compared with the traditional stress-life method used in fatigue analysis, this methodology considers the influence of compressive residual stress more adequately by applying fracture mechanics by advanced simulation tools to provide an entire framework for predicting the fatigue life of notched components, making it available for the fatigue design and assessment of such structures.

4.1 Calculating the S-N_i Curve by SMART Crack Growth Tool

Several approaches have been proposed to estimate the crack initiation life from various factors such as strain [109], stress [110], a combination of strain range with crack length [111] and shear stress range [112]. Here, a new method is proposed, where the crack initiation life is determined by a stress-life method based on a derived stress vs number of cycles to crack initiation, S-N_i , curve for smooth fatigue specimens. A conventional *S-N* curve defines the total number of cycles to specimen failure, encapsulating the crack initiation life and crack propagation life. Here, the crack initiation life is determined by subtracting the calculated crack propagation life, considering an assumed initial crack length, from the total fatigue life. The crack propagation life is calculated by finite element method by ANSYS shown in the next sub-section.

4.1.1 Crack Growth Simulations by SMART

Numerical modelling of crack propagation can be achieved within a Finite Element environment, using methods such as Cohesive Zone Modelling (CZM) [113], Extended Finite Element Method (XFEM) [114, 115], and Ansys Separating Morphing and Adaptive Remeshing Technology (SMART) [116-119]. In CZM, the crack growth path must be predetermined by adhesive attachment between two surfaces. XFEM allows for crack growth by splitting existing elements, which increases the number of elements and consequently slows down the simulation, causing computational inefficiencies. SMART is the newest tool innovated by Ansys.

Compared with XFEM, the Unstructured Mesh Method utilized in SMART can regenerate the meshes on the crack front during crack growth to save computational effort.

In the SMART crack growth tool, either stress intensity factors or J-integrals can be calculated, As the mode-I K_I and mode-II K_{II} can not be distinguished in a single value of J-integral, stress intensity factors are used as fracture criteria here. In SMART, the stress intensity factors of two modes are obtained by interaction integral method which includes the application of an auxiliary field on the J-integral [120].

4.1.2 Calculating the S-N_i curve of 316l Stainless Steel

AISI 316L stainless teel is selected for an example of the calculation of the S-N_i curve. In the context of AISI 316L stainless steel, the average size of two grains can be selected as the crack initiation length based on experimental observations from [74]. As a result, the initial crack length is assumed to be $200\mu m$, a value also consistent with the TCD methodology [6], where cracks are assumed to emanate from a length equal to two material characteristic lengths ($224\mu m$ for AISI 316L). Additionally, 0.2mm assumed crack initiation length is also suitable to the low carbon steel [121].

Huang et al. [122] performed fatigue tests for 316L with load ratio $R = 0.2$, using a plain cylindrical tensile test specimen following ASTM E466 [123]. The results were presented in the form of a maximum stress (S_{max})-total fatigue life (N_t) curve. From the data, a corresponding S-N_i curve is derived for a $200\mu m$ crack initiation length by calculating the crack growth life using the ANSYS SMART tool.

A finite element model of the test specimen of Huang et al. created in ANSYS Workbench is shown in Figure 4.2. An initial semi-elliptical crack of length $200\mu m$ is located in the gauge section. From previous investigations of the shape of surface cracks in round bars under constant axial loading [124, 125], the crack minor to major axis aspect ratio was defined as 0.6. The entire model is meshed by SOLID 187 with 33283 nodes and 20991 elements. The material properties were Young's modulus E =200GPa, Poisson's ratio $\nu = 0.3$ and Paris Law constants $C =$

$5.61\text{x}10^{-9}\ \frac{\text{mm / cycle}}{(MPa\sqrt{\text{m}})^m}$ and $m = 3.25$ [56]. The specimen is fixed at the bottom end and uniformly distributed cyclic force is applied at the top end as 70MPa.

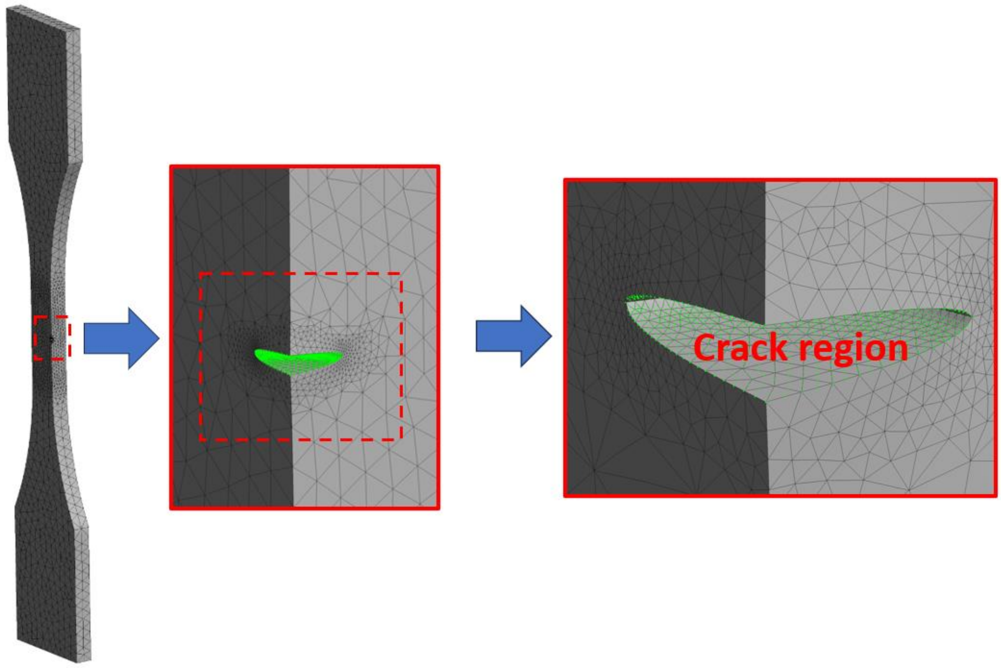

Figure 4.2 Finite element model of cracked smooth specimen, showing the overall finite element mesh and zoomed view of the crack region.

The SMART facility was used to compute the number of cycles from the assumed initial crack length to the final failure (N_g) during the process of crack growth under an axial cyclic stress $\Delta\sigma_n$. Subsequently, N_i was determined from the S_{max}-N_t curve provided in [29], such that $N_i = N_t - N_g$. To generate the S-N_i curve, multiple SMART analyses were conducted for various load magnitudes. Alternatively, a more computationally efficient approach involves performing a single SMART analysis to capture the evolution of the stress intensity factor range ΔK with increasing crack length a for a nominal stress range $\Delta\sigma_n$. ΔK can then be defined as a continuous function of a by fitting a polynomial equation of order n to the numerical results, such that:

$$\Delta K = f(a) = A_n a^n + A_{n-1} a^{n-1} + \cdots + A_0 a^0 \tag{4.1}$$

where $A_{\mathrm{n}}, A_{n-1}, \dots, A_o$ are constants. A corresponding function for configuration factor Y is thus defined as:

$$Y(a) = \frac{1}{\Delta\sigma_n\sqrt{\pi a}}\, f(a) \tag{4.2}$$

The fatigue life for any stress range $\Delta\sigma$ can then be determined analytically from the Paris law in the form:

$$\frac{da}{dN_g} = C(\Delta K_{\Delta\sigma})^m \tag{4.3}$$

where

$$\Delta K_{\Delta\sigma} = \; Y(a)\, \sqrt{\pi a}\, \Delta\sigma \tag{4.4}$$

The crack growth life N_g for stress range $\Delta\sigma$ is thus:

$$N_g = \int_{a_0}^{a_f} \frac{1}{C(K_{\Delta\sigma})^m} \tag{4.5}$$

where a_0 and a_f are initial crack length and final crack length respectively.

N_i is plotted against the corresponding maximum stress in Figure 4.3. It is seen that with the proportion of crack initiation life to total life declines with increasing of maximum stress. This trend agrees with results from Santus and Taylor, who calculated the N_i through physically short crack propagation in several metals [71]. From this trend, $\log(N_i)$ can be assumed to vary linearly with maximum stress in the high cycle fatigue range.

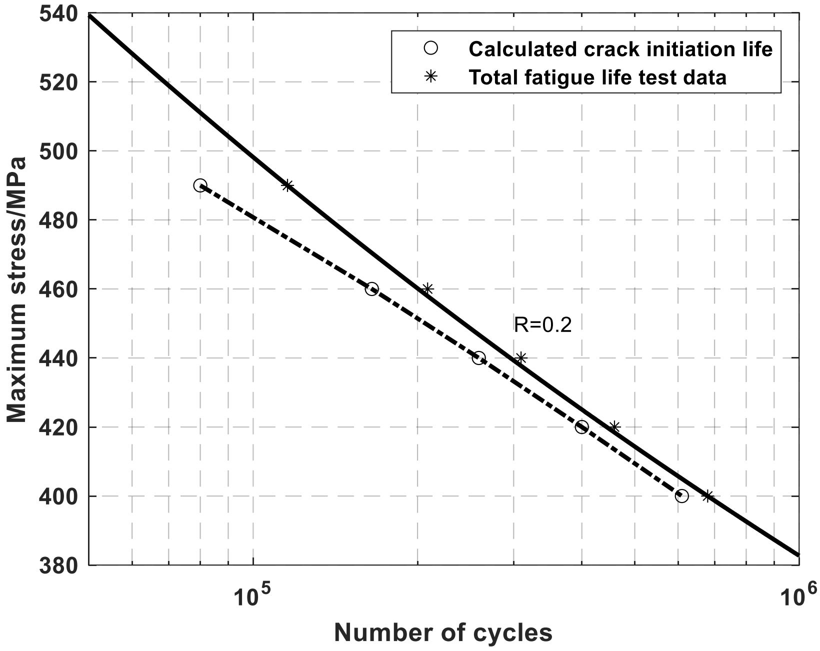

Figure 4.3. Total life curve (R=0.2) and proposed stress-crack initiation life of 316L.

The same method can also be applied to other materials. Pegues et al [126] investigated micro-cracks in 304L stainless steel by interrupted high cycle fatigue tests, under a fully reversed load with a stress amplitude of 330MPa. Tests were interrupted every 10,000 cycles to observe nucleation of micro-cracks by scanning electron microscope (SEM), and then interrupted every 3000-5000 cycles to investigate the propagation of MSC until cracks were approximately $200\mu m$, where the crack nucleation and MSC growth were completed. Results showed a total fatigue life N_t of around 5×10^5 cycles, and a combined life of nucleation and MSC crack growth, here taken to be the initiation life N_i, of around 1×10^5 cycles.

In the present investigation, the specimen from [126] was modelled in ANSYS Workbench using the SMART crack growth method to simulate crack growth. The results showed that when Y is taken as 0.65, the predicted initiation life N_i is approximately 1.7×10^5, which is close to the value given in [126].

The same procedures are also applied to S355 low carbon steel to generate the S-N_i curve as shown in Figure 4.4.

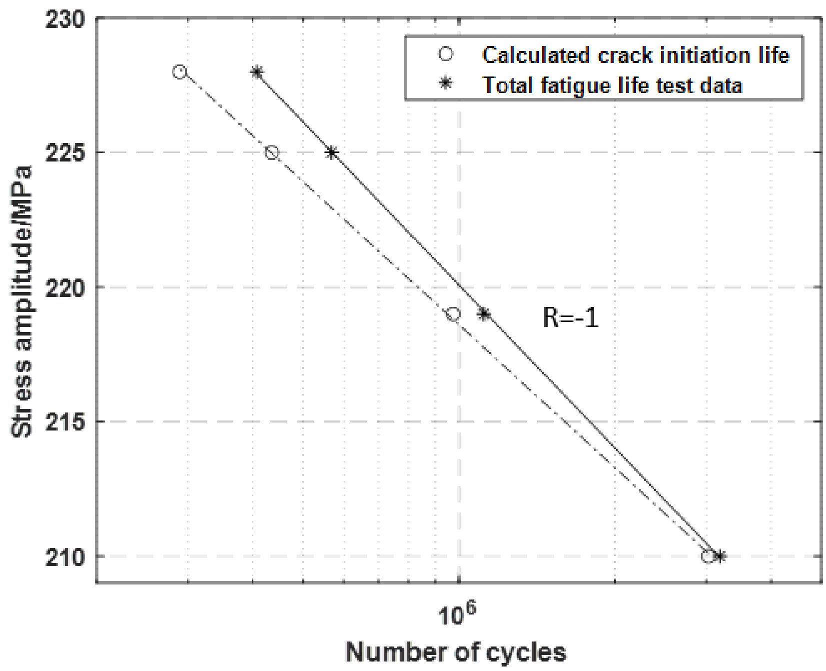

Figure 4.4. Total life curve (R=-1) *and proposed stress-crack initiation life of S355.*

4.1.3 Influence of Physically Small Crack

If the long crack (LC) growth is directly linked to microstructurally small crack (MSC) growth, the development of physically small cracks (PSC) is included in the LC. However, it's important to note that the crack growth rate in PSC cannot be characterized using the same Paris law parameters typically used for LC growth. Therefore, the influence of PSC on the total life is discussed here.

When considering the influence of PSC, the threshold of PSC ($\Delta K_{th,a}$) is induced in the Paris Law as:

$$\frac{da}{dN} = C(\Delta\mathrm{K} - \Delta K_{th,a})^m \tag{4.6}$$

When the PSC regime is neglected, the variable threshold of PSC in (4.6) can be replaced by the constant intrinsic threshold ΔK_{dR}. Santus and Taylor [71] constructed multiple curves for the propagation of PSC and crack initiation with stress amplitudes based on the Chapetti model. In this context, the curves for Ti-6Al-4V at a stress ratio of 0.1 are selected to exemplify the impact of PSC life on crack initiation life. The material properties utilized for calculating PSC propagation life are provided in Table 4.1.

Table 4.1. Material properties of Ti-6Al-4V (R=0.1).

d_1/mm	d_2/mm	C/$\frac{m/cycle}{MPa\sqrt{m}^m}$	m	$\Delta K_{th,R}/\ MPa\sqrt{m}$
0.02	0.2	2.7e-9	1.54	4.3

The results of PSC propagation life and crack initiation life from [71], the calculated PSC propagation life and the calculated life neglecting PSC are shown in Figure 4.5.

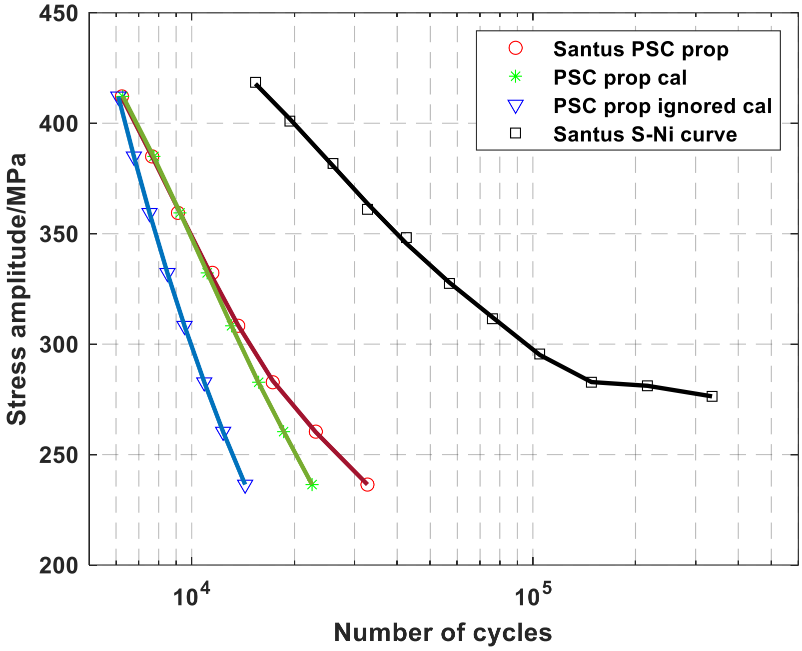

Figure 4.5. Predicted propagation life with and without PSC against initiation life compared with [71].

The calculated PSC propagation life in Figure 4.5 is similar to the results of Santus and Taylor, and shows that the difference in calculated fatigue life with and without the PSC increases with reducing stress amplitude. The maximum difference of 8,190 cycles, 2.4% of the corresponding crack initiation life, is relatively small. This indicates that the S-N_i curve created by assuming the PSC is included in the LC is acceptable.

4.2 Residual Stress Effect

Two approaches have been proposed in the literature to represent the influence of K_{rs} on crack propagation: the crack closure method [86, 127-131] and the superposition method [132, 133]. Here, the superposition method is utilised. The total stress intensity factor, K_{tot}, is typically decomposed into two components: the applied stress intensity factor, K_{app}, and the residual stress intensity factor, known as K_{rs}. The maximum stress intensity factor, $K_{max,tot}$, and minimum stress intensity factor $K_{min,tot}$ are thus:

$$K_{max,tot} = K_{max,app} + K_{rs} \tag{4.7}$$

$$K_{min,tot} = K_{min,app} + K_{rs} \tag{4.8}$$

The total stress intensity factor range ΔK_{tot} is therefore:

$$\Delta K_{tot} = K_{max,tot} - K_{min,tot} = K_{max,app} + K_{rs} - K_{min,app} - K_{rs}$$

which is independent of the residual stress and equal to ΔK_{app}:

$$\Delta K = K_{max,app} - K_{min,app} = \Delta K_{app} \tag{4.9}$$

The effective stress intensity ratio R_{eff} can then be obtained as:

$$R_{eff} = \frac{K_{min,tot}}{K_{max,tot}} = \frac{K_{min,app} + K_{rs}}{K_{max,app} + K_{rs}} \tag{4.10}$$

According to the Paris Law and the superposition method, the crack growth rate can be defined as a function of ΔK_{eqv} and R_{eff}:

$$\frac{da}{dN} = C_{R_{eff}} \left(\Delta K_{eff}\right)^{m_{R_{eff}}} \tag{4.11}$$

where $C_{R_{eff}}$ and $m_{R_{eff}}$ are the Paris law parameters corresponding to stress ratio R_{eff}.

The value of R_{eff} varies throughout the process of crack growth, requiring the determination of Paris law parameters for different R values. In the SMART crack growth method, the Walker equation is employed to establish a correlation between the Paris law and R, calculating the ΔK_{eff} from ΔK_{app} while disregarding the effects of crack closure. However, when including the impact of compressive residual stress, it is important to note that the values of R_{eff} in the compressive residual stress region turn negative. In such cases, the values of K_{max} provide a more suitable representation of the crack closure and opening effects when compared to ΔK based on the crack closure concept.

Kujawski's equations consider the crack closure effect. Following Kujawski's equations, two additional equations are proposed to estimate crack growth life which include the values of K_{app} and K_{rs} while considering various ranges of R. To determine the crack growth rate in the presence of induced residual stress, ΔK_{app} from equation (4.9) and R_{eff} from equation (4.10) can be substituted into equations (2.55) and (2.56).

The number of cycles to grow a crack from the initial length a_0 to final length a_f is thus:

$$N = \int_{a_0}^{a_f} \frac{1}{C\left(\frac{\Delta K}{(1-R)^{\alpha}}\right)^{m}} = \int_{a_0}^{a_f} \frac{1}{C\left(\frac{K_{app}}{\left(1-\frac{K_{rs}}{K_{app}+K_{rs}}\right)^{\alpha}}\right)^{m}} \qquad R > 0 \qquad (4.12)$$

$$N = \int_{a_0}^{a_f} \frac{1}{C(\frac{\Delta K}{(1-R)})^{m}} = \int_{a_0}^{a_f} \frac{1}{C(\frac{K_{app}}{\left(1-\frac{K_{rs}}{K_{app}+K_{rs}}\right)})^{m}} \qquad R < 0 \qquad (4.13)$$

4.3 Determining K_{rs} and ΔK_{eff}

Several models have been proposed for crack growth analysis in the presence of induced residual stress. These approaches mainly focus on determining the stress intensity factor for the residual stress field, K_{rs} [132, 134, 135].

K_{rs} may be calculated by a weight function approach, proposed by Buechner [136] as:

$$K_{rs} = \int_{x=0}^{x=a} \sigma_{rs} m(x,a) dx \tag{4.14}$$

where, σ_{rs} is residual stress and $m(x,a)$ is the weight function. The basis of the weight function method is to calculate the stress intensity factors directly from the stress distribution around the crack, rather than the remote loading. Weight function for edge cracks [137] or a corner crack [138] can be obtained by constant and linear crack face pressure fields, and weight functions for different combinations of cracks and structures have been obtained [139-141].

As the weight function method is difficult to apply in complex 3D models, therefore, the effect of induced residual stress on crack growth is determined using the superposition method here. This requires the evaluation of $\Delta K = \Delta K_{app}$ (4.9) and R_{eff} (4.10). a numerical method based on the superposition method is proposed to calculate K_{rs}.

The residual stress distribution in the component under investigation is evaluated by elastic-plastic FEA for a given initial autofrettage overload. As the SMART tool is restricted to linear elastic material behaviour, it cannot be applied in a plastically deformed model. However, the effect of residual stress on crack propagation can be represented by importing the calculated residual stress distribution into a similar linear elastic model as an initial state of stress.

Two linear elastic models with identical meshes are used to determine the stress intensity factor of the residual stress K_{rs}. The first model considers the component with no autofrettage. The elastic model is subject to an applied cyclic load P_{app}, representing the operating conditions of the component. The stress intensity range calculated with increasing crack length using this model is ΔK_{app}. In the second condition, the residual stress calculated in the elastic-plastic solution is imported into the elastic model as an initial state of stress, and cyclic load P_{app} applied. The stress intensity range calculated by this model is $\Delta K_{app} + K_{rs}$. The variation of the stress intensity of the residual stress K_{rs} with crack length a is then evaluated by stress superposition, by subtracting ΔK_{app} from the second condition results.

After determining the K_{rs}, the R-ratio correction method proposed by Kujawki and Dinda [89] was applied to calculate the ΔK_{eff}. This R-ratio correction method is based on the crack closure concept, in this method, the crack driving force as the K^* is dominated by either ΔK or K_{max}, and ΔK_{eff} can be calculated as shown in (4.15).

$$\Delta K_{eff} = K^* = \frac{\Delta K}{(1 - R_{eff})^{\alpha}} \qquad \text{For } R_{eff} > 0 \tag{4.15}$$

$$\Delta K_{eff} = K^* = K_{max} = \frac{\Delta K}{(1 - R_{eff})} \qquad \text{For } R_{eff} < 0$$

Chapter 5 Fatigue Life of Double Notch Specimens

The proposed procedure for calculating the fatigue life and the fatigue limit in a notched component with an induced residual stress system is shown schematically in Figure 4.1. The effectiveness of this approach is demonstrated through experimental investigation of the fatigue life and fatigue limit of preloaded double-notch uniaxial test specimens made from AISI 316L austenitic stainless steel and S355 low carbon steel.

The test specimens incorporate a feature where compressive residual stress can be induced in the notched region through limited axial overloading prior to fatigue testing. This preloading results in a localized compressive stress distribution at the notch intersections, resembling the stress distribution typically found at stress raisers in pressure components after autofrettage processes.

Crack propagation in notched elastic components with no residual stress can be calculated directly by FEA SMART analysis, in the same way as the plain fatigue specimen of Chapter 4. When more than one load level is considered, separate SMART analyses can be performed for each load level considered. Alternatively, a polynomial representation of the stress intensity range (4.1) can be determined from a single SMART analysis and a continuous function for configuration factor (4.2) obtained. This can then be substituted into the Paris law (4.12) and (4.13) and integrated for each individual stress range considered. The latter approach requires less FEA computing resource and is used here to determine the fatigue life in regions of compressive residual stress.

5.1 Notched Specimen and Material Properties

The geometry and dimensions of the square cross-section specimens are shown in Figure 5.1 and Table 5.1. The double-notch specimen is more representative of the 3D stress distribution in pressure components with local stress raisers, such as pressure vessels, pump bodies and valve housings, than a single notch specimen. It can also be designed to include a larger stress concentration factor, leading to higher residual stress when experimentally investigating the influence of residual stress on fatigue life. Two types of double-notched tensile test specimens, Type A and Type B are considered [108, 142]. Among these, Type A in [142] is designed and tested by author. The geometry and dimensions of the specimens are shown in Figure 5.1. For specimen type A, *W* is 14mm and *L* is 150mm and for specimen type B, *W* is 21mm, *L* is 180mm.

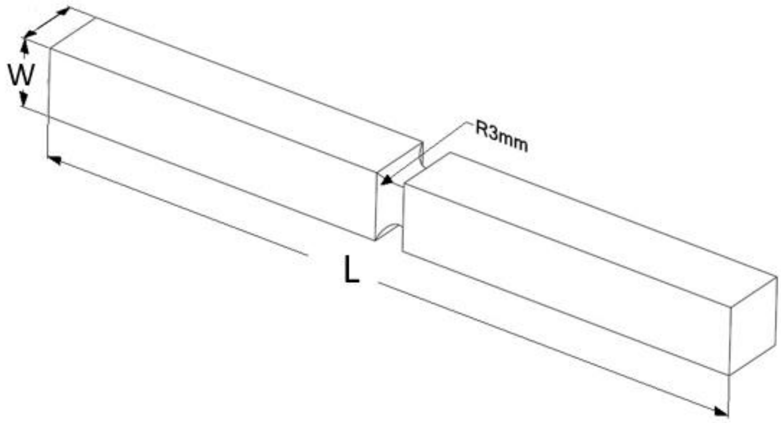

Figure 5.1. Double-notch fatigue test specimen.

Table 5.1. Double notch specimens dimensions.

Dimension	Type A	Type B
W	14mm	21mm
L	150mm	180mm
Radius of notch	3mm	3mm

A monotonic stress-strain curve for the 316L material was obtained by tensile test. Following ASTM E8 [143], the tensile test specimen was designed as shown in Figure 5.2. Two monotonic stress-strain curves were obtained by two standard specimens without heat treatment, as shown in Figure 5.3.

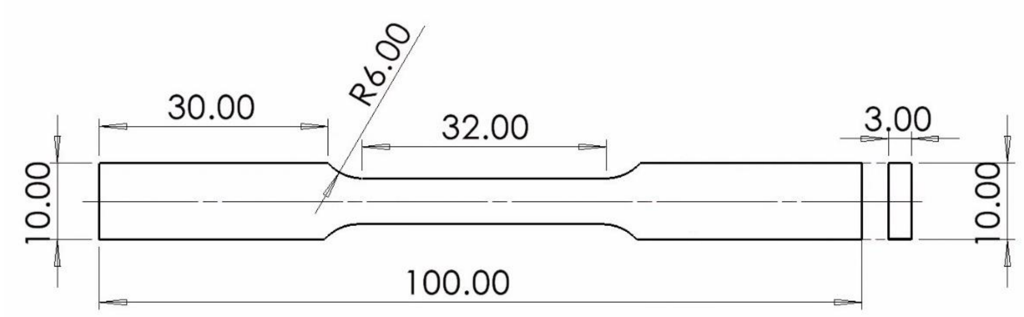

Figure 5.2. Tensile test specimen geometry [mm].

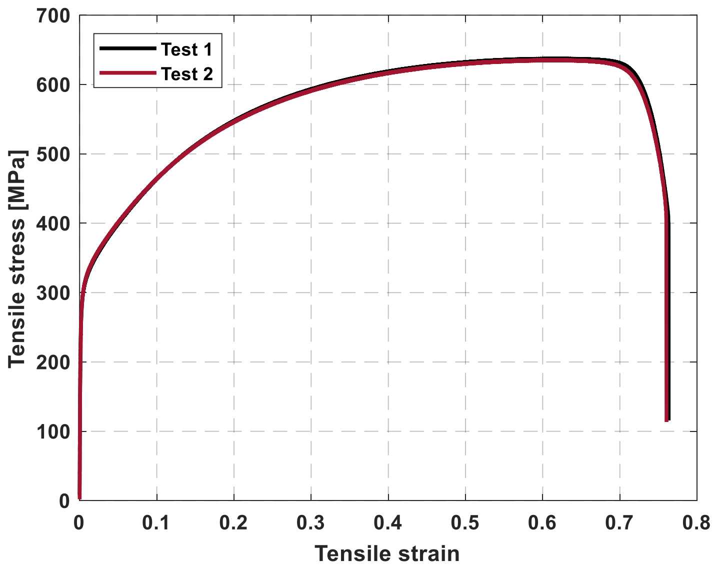

Figure 5.3. Monotonic stress-strain curves for two 316L specimens.

Figure 5.3 shows the 316L stainless steel exhibits continuous yielding. As such, there is no distinct yield point and yield stress is usually defined with reference to a specific plastic strain offset, such as the 0.2% proof stress used in general engineering. The 0.2% offset definition is not suitable for a detailed elastic-plastic analysis as presented here [144]. Alternative definitions of the offset strain [145-147] have been reviewed by Abdel-Karim, ranging from 0.01% to 0.1% [148]. In the present study, to identify the plastic behaviour more accurately, 0.01% offset strain was selected, giving a yield stress of 225MPa. Young's Modulus was obtained as 200GPa.

To calculate the crack initiation life in the presence of compressive residual stress, the cyclic stress-strain curve for the material is required for use in FEA. Here, the

Chaboche model parameters (3.9) are determined from data from stable cyclic stress-strain tests of Dutta et al [149]. The four red data points used to fit the model are shown in Figure 5.4, along with the monotonic stress-strain curve from the present investigation (Figure 5.3). Comparison of the monotonic and cyclic stress-strain data illustrates the cyclic hardening behaviour of 316L stainless steel [150]. This hardening phenomenon can also be investigated in S355 low carbon steel as shown as the blue points and line in Figure 5.4 representing the stable cyclic stress-strain data and the monotonic stress-strain curve.

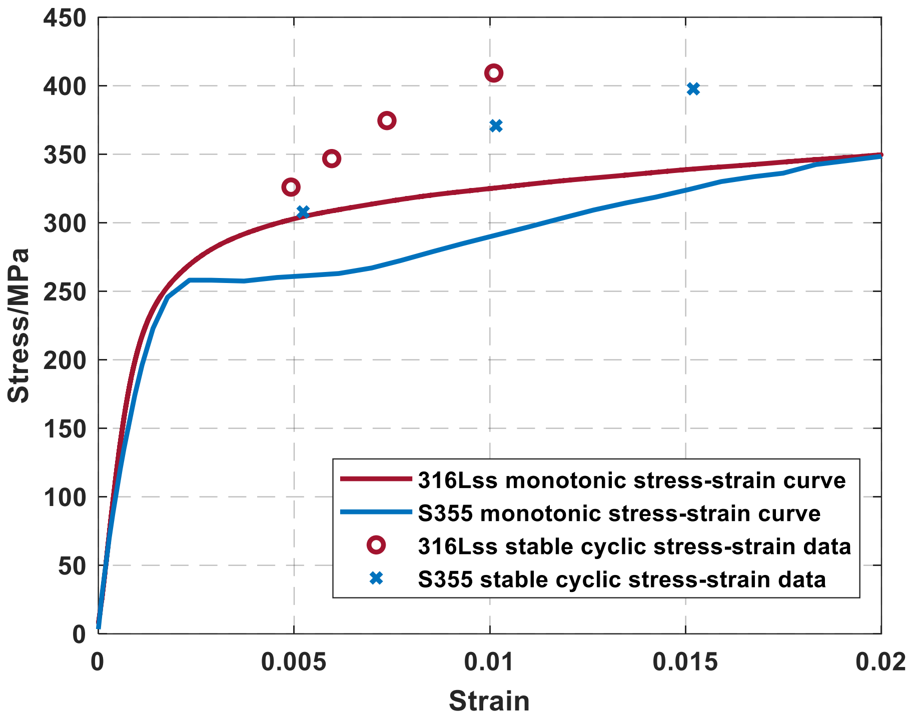

Figure 5.4. 316L monotonic stress-strain curve and cyclic stress-strain data from [149], *showing material cyclic hardening.*

As shown in the Figure 5.4, the yield stress and the Young's modulus of these two steels are similar. The material properties of these two materials are summarized in Table 5.2.

Table 5.2. Material properties of two stainless steels.

Material	S355 low carbon steel	316L stainless steel
Young's Modulus /Pa	2×10^{11}	2×10^{11}
Poisson's ratio	0.3	0.3
Yield stress/ MPa	255	255
Paris Law parameter *C* (reference unit m)	1.43×10^{-11}	5.61×10^{-11}
Paris Law parameter m	2.75	3.25
Chaboche material constant C_1/MPa	30489	63400
Chaboche material constant γ_1	135.41	303.41

The preload force and working force amplitude applied to the models correspond to the full-specimen test values given in Table 5.3.

Table 5.3. Preloads and working cyclic loads $(R = 0)$ *for specimen Types A and B.*

	Preload kN	Working Force Amplitude kN
Specimen A	21	7.5, 8, 8.5, 9
Specimen B	75	21, 22, 23, 24, 25

5.2 Notched Specimen without Residual Stress

The double-notch specimen was modelled in ANSYS Workbench using the SMART crack growth tool, using SOLID 187 10 node tetrahedral structural solid elements with the mesh refined towards the crack front. The crack initiation can be determined by experiments. Figure 5.5 illustrates the comparison between the intact specimen and half of the fractured specimen in which the crack initiation can be investigated on the notch root.

An initial semi-elliptical crack with an aspect ratio of 0.6 located at the intersecting notch root of the model was considered, as shown in Figure 5.6. A coordinate system defined at the crack has X in the direction of the crack path and Y perpendicular to the crack surface.

Preliminary finite element investigations showed a lengthwise quarter-symmetry model of the specimen gave similar results to a full model with the same mesh density for the crack growth range considered. With the same crack growth length, the results obtained based on these two models are close when the mesh size is same. A quarter model was therefore used in the analysis to reduce computing requirements.

The material properties were as given in Section 4.1.2 for the smooth fatigue specimen model. The quarter-model was fully fixed at one end and symmetry boundary conditions were applied on the planes of symmetry. Cyclic axial force varying between zero to a maximum value was applied to the free end of the model. Analysis was performed for three maximum force values, corresponding to 8kN, 8.5kN and 9kN as shown in Table 5.3 on a full test specimen.

A convergence study was performed by investigating the effect of mesh density on the calculated configuration factor Y, (4.2). Results of Y distribution for two mesh densities are shown in Figure 5.7: Mesh 1 had 28525 elements (42727 nodes) and Mesh 2, shown in Figure 5.8, had 14532 elements (22580 nodes). Figure 5.7 shows that the values of Y calculated for a range of relative crack depths are similar for both meshes. Mesh 2 was therefore selected for analysis to minimise computing requirements.

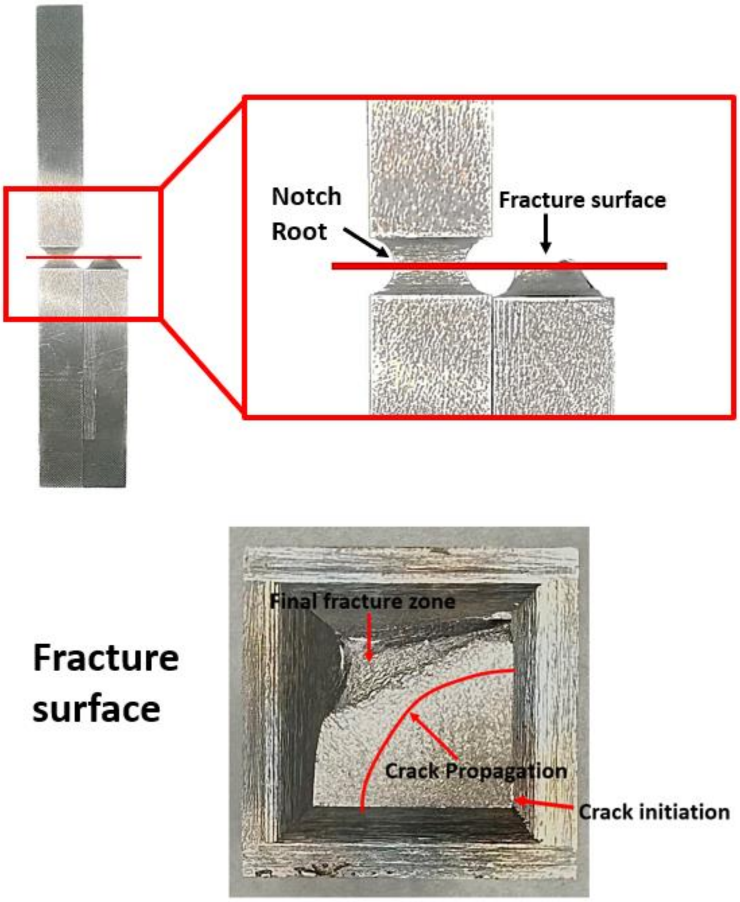

Figure 5.5. Comparison of intact specimen with fractured specimen.

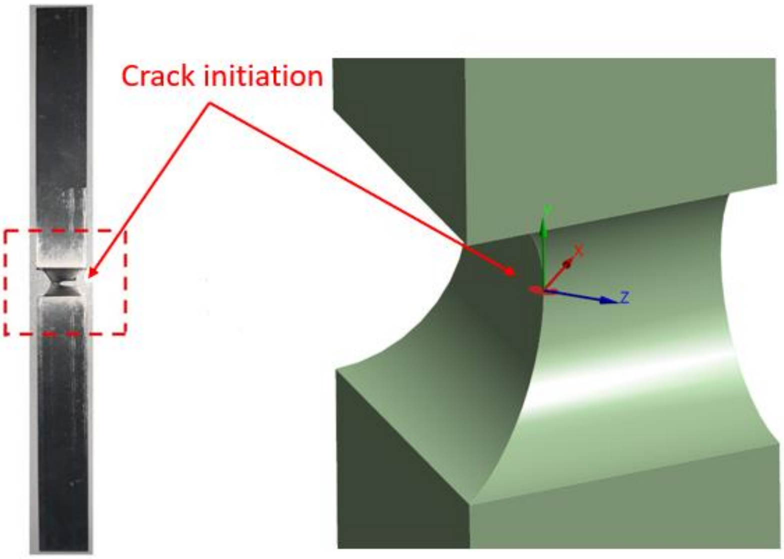

Figure 5.6. Failed test specimen and quarter symmetry model showing the location of crack initiation.

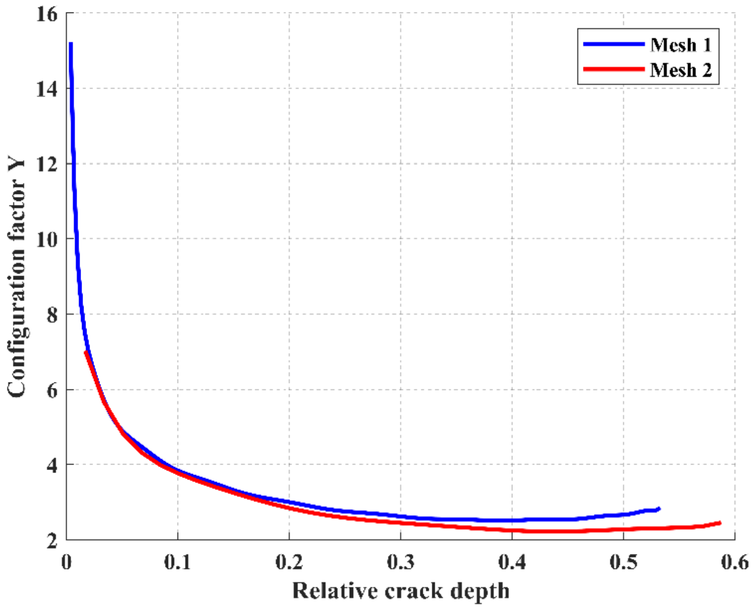

Figure 5.7. Configuration factor Y for a crack in the double-notch specimen for two different mesh densities.

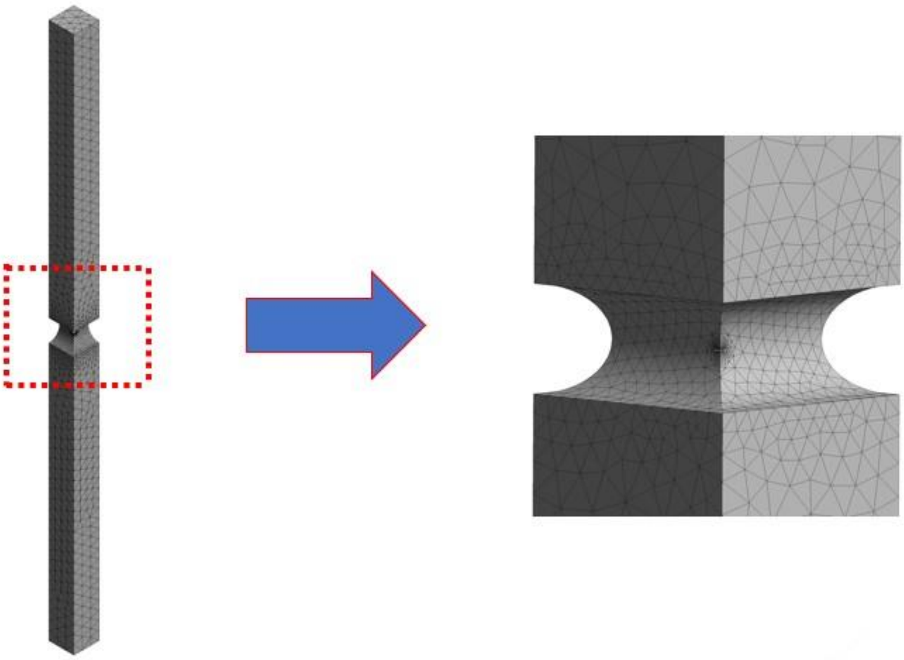

Figure 5.8. Finite element mesh used in analysis (Mesh 2).

Figure 5.7 shows that in the notched specimen Y decreases with increasing crack size, possibly due to the stress gradient, and then has a slight increase at the end. As the stress decreases with distance from the notch root, the nominal stress $\Delta\sigma_n$ in (4.2) varies with crack propagation and must be updated. The trend of Y in Figure 5.7 is similar to that of Schijve [151], who determined the stress intensity factor of cracks at notches by considering the influence of the stress concentration factor.

The same procedures are applied to the type B specimens with the loadings shown in Table 5.3 as well. The numerical results for ΔK_{app} obtained for the applied loads are shown in Figure 5.9. As the values of ΔK_{app} are thus determined, the crack growth life without the residual stress can be calculated from the Paris law.

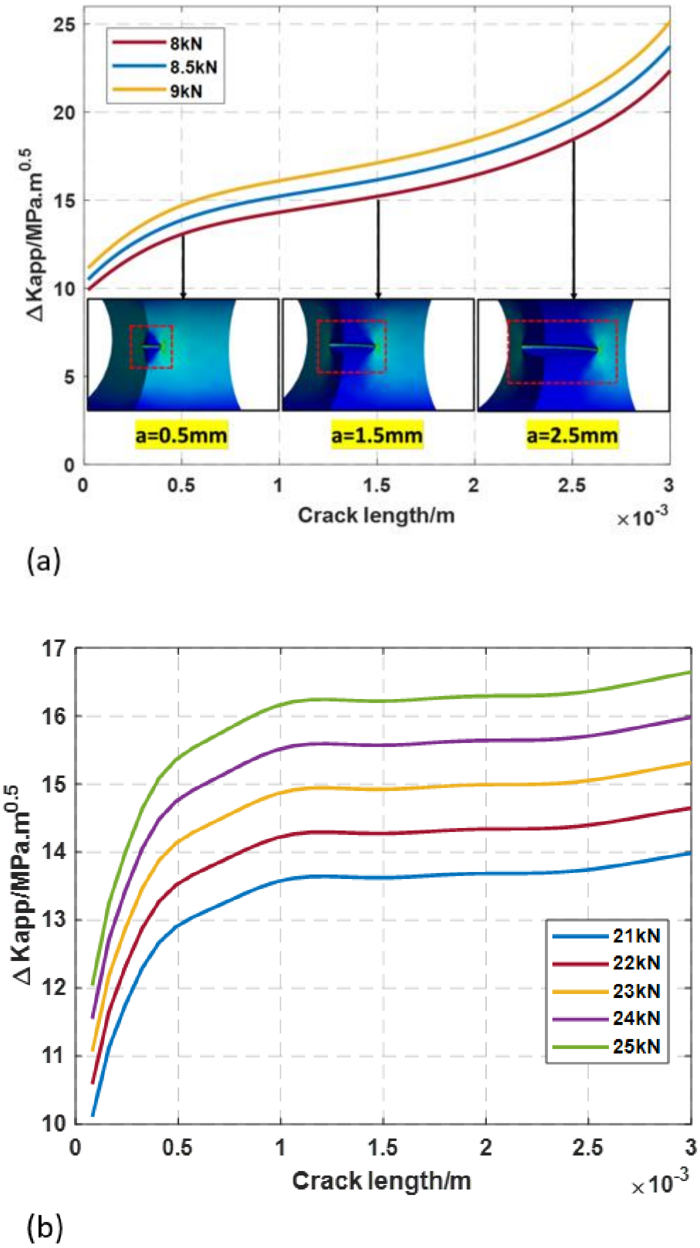

Figure 5.9. Variation in of stress intensity factor range ΔK_{app} with increasing crack length a) type A b) type B.

5.3 Notched Specimen with Residual Stress

Residual stress can be induced in double-notch specimens by tensile preloading prior to fatigue testing, causing local plastic deformation at the notch root on loading and inducing compressive residual stress on unloading.

5.3.1 Residual Stress Calculation

The notch root residual stress was calculated by elastic-plastic Finite Element Analysis in ANSYS workbench. A quarter-symmetry finite element model was used, with a mesh similar to the crack growth model of Section 4 prior to insertion of the SMART crack. A multilinear kinematic hardening plasticity material model based on the monotonic stress-strain curve of Figure 5.3 was used. The finite element model was fully fixed at one end and symmetry boundary conditions were applied on the planes of symmetry. The preload was simulated by applying a uniformly distributed axial tensile force equivalent to 21kN on a full specimen to the free end of specimen A and 75kN to specimen B, then reducing the force to zero.

When the axial force was applied, plastic deformation occurred locally at the notch root. When the force was then reduced to zero, a compressive residual stress system was established at the notch root due to elastic recovery of the elastically deformed regions of the specimen. The distribution of minimum principal residual stress in the notch region and along the predicted crack path are shown in Figure 5.10.

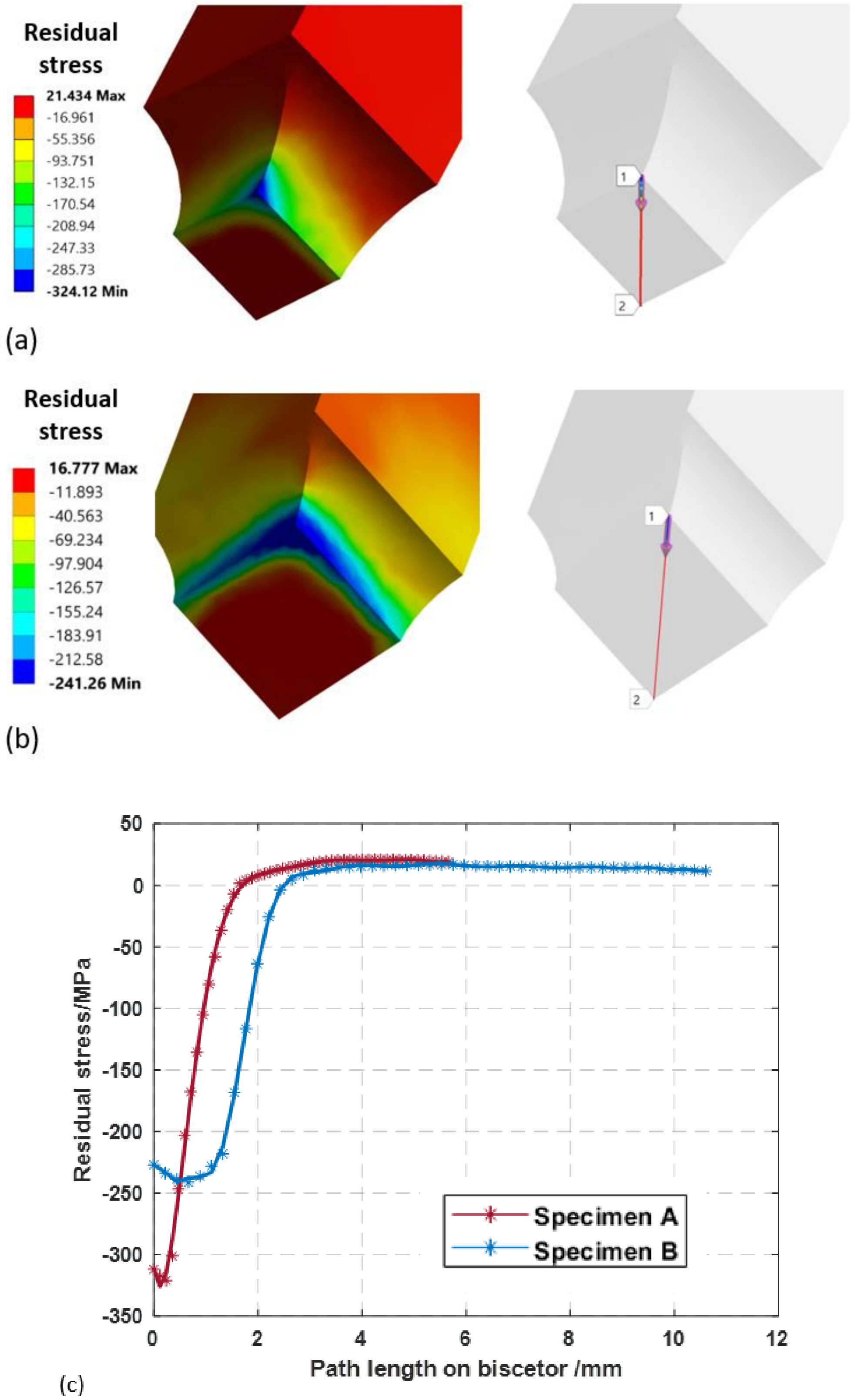

Figure 5.10. Minimum principal stress distribution (residual stress) at the notch root after preloading and local distribution along the crack path [MPa] a) type A b) type B. (c) Residual stresses along the bisector.

5.3.2 Stress Intensity Factor of Residual Stress

When the distribution of residual stress is known, K_{rs} can be calculated by treating the residual stress field as an initial condition in Finite Element Analysis. Here, a superposition method is proposed to calculate the K_{rs}, using the SMART crack growth method. First, the calculated residual stress distribution is exported from the elastic-plastic solution and imported into a similar LEFM model as an initial state of stress prior to SMART crack growth simulation. The initial crack cannot propagate with only residual stress, so crack propagation is simulated using an applied arbitrary axial load. With the arbitrary load, the value of $\Delta K_{app} + K_{rs}$ with changing crack length a is obtained and based on the superposition method, the value of K_{rs} can be determined by subtracting ΔK_{app}. The calculated variation of K_{rs} with crack length is shown in Figure 5.11. The values of K_{rs} can also be represented by a polynomial equation (4.1), and combined with the values obtained for ΔK_{app} (Figure 5.9) to determine the crack growth life with induced residual stress from equations (4.12) and (4.13).

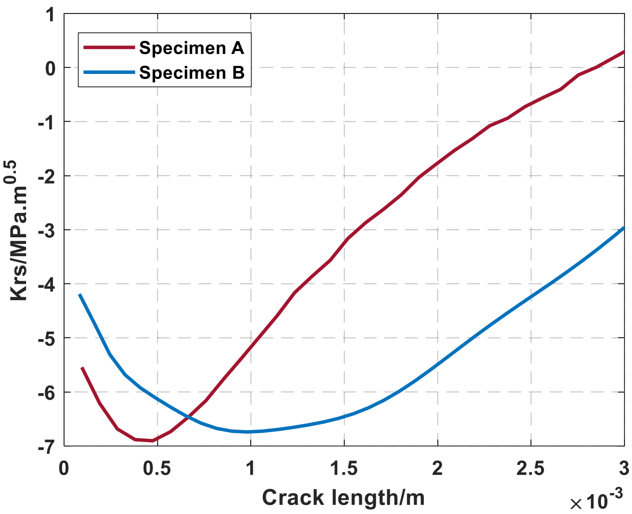

Figure 5.11. Stress intensity factor of residual stress against the crack length.

5.3.3 Crack Initiation Life Prediction

Both specimen Type A and specimen Type B are discussed in this section, the Type A is taken for an example to show the procedures to predict the crack initiation life. The crack initiation life is determined from the stress-crack initiation curve shown in Figure 4.3 by calculating the equivalent stress amplitude experienced by the specimen during cyclic loading. The equivalent stress is calculated from a FEA model similar to the preload model, but with a Chaboche kinematic hardening plasticity material, obtained by curve-fit of the cyclic stress-strain data of Figure 5.4. For specimen A with a preload-induced residual stress field, the residual stress distribution is exported from the original preload elastic-plastic finite element model and imported into the cyclic load model as an initial stress condition. Three different cyclic axial force amplitudes of 8kN, 8.5kN and 9kN were applied to investigate the cyclic stress behaviour for specimens.

Results for 8kN force amplitude with and without residual stress are shown in Figure 5.12. The maximum stress amplitude of 240.1MPa occurs at the notch root. The mean stress for the non-preloaded specimen is 74.4MPa. When the preload is included, this reduces to -0.1MPa. In the stress-life method, the decrease in mean stress leads to a lower equivalent stress amplitude, increasing the calculated fatigue life of the specimen.

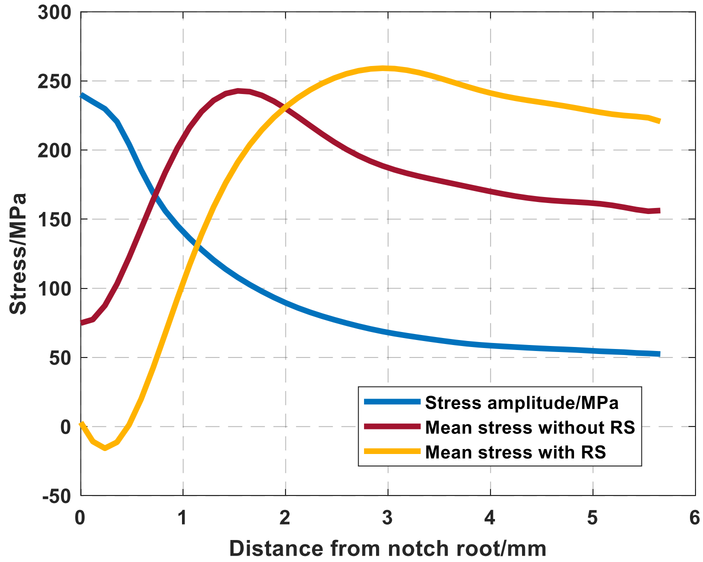

Figure 5.12. Stress amplitude and mean stress in notch region.

For no residual stress, the equivalent stress is calculated using the maximum stress amplitude shown as the red line in Figure 5.12. When residual is present, the mean stress shown as the yellow line in Figure 5.12 is used. The crack initiation life is calculated from a proposed crack initiation S-N_i curve in Figure 4.3, based on von Mises equivalent stress amplitude. Considering the multiaxial fatigue, the effective mean stress is assumed to be proportional to the hydrostatic stress [56]. The stress amplitude σ_a and effective mean stress σ_m can be calculated by (5.1) and (5.2).

$$\sigma_a = \frac{1}{\sqrt{2}}\sqrt{(\sigma_{xa} - \sigma_{ya})^2 + (\sigma_{ya} - \sigma_{za})^2 + (\sigma_{za} - \sigma_{xa})^2 + 6({\tau_{xya}}^2 + {\tau_{yza}}^2 + {\tau_{xza}}^2)} \tag{5.1}$$

$$\sigma_m = \sigma_{xm} + \sigma_{ym} + \sigma_{zm} \tag{5.2}$$

The Walker Equation (2.11) is used to correlate the influence of mean stress. The calculated σ_{ar} for force amplitude of 8kN, 8.5kN and 9kN are then substituted into S-N_i curve to obtain the crack initiation life with and without induced residual stress. Similar procedures are applied to specimen B.

5.4 Experimental Investigation

Three 316LSS double-notch specimens with no induced residual stress and 5 specimens with a 21kN preload were tested under 8kN, 8.5kN and 9kN force amplitude (R=0) cyclic loads on a 100kN servo-hydraulic fatigue testing machine as shown in Figure 5.13. All tests were under force control at 20 Hz. The test fatigue life results for the specimens with induced residual stress are shown in Figure 5.14, along with the fatigue life calculated using the proposed method.

In traditional stress-life fatigue analysis, prediction is based on stress at a point. Averaged or nominal stress may be used at notch locations to account for stress gradient effects, but it is difficult to determine the appropriate characteristic length to obtain the average stress when residual stress is present, due to the variation in stress ratio. In such cases, the maximum stress is selected for substitution into the *S-N* curve, rather than an average stress. If the maximum stress amplitude is directly substituted into Huang's *S-N* curve, the predicted life is calculated as shown in Figure 5.14.

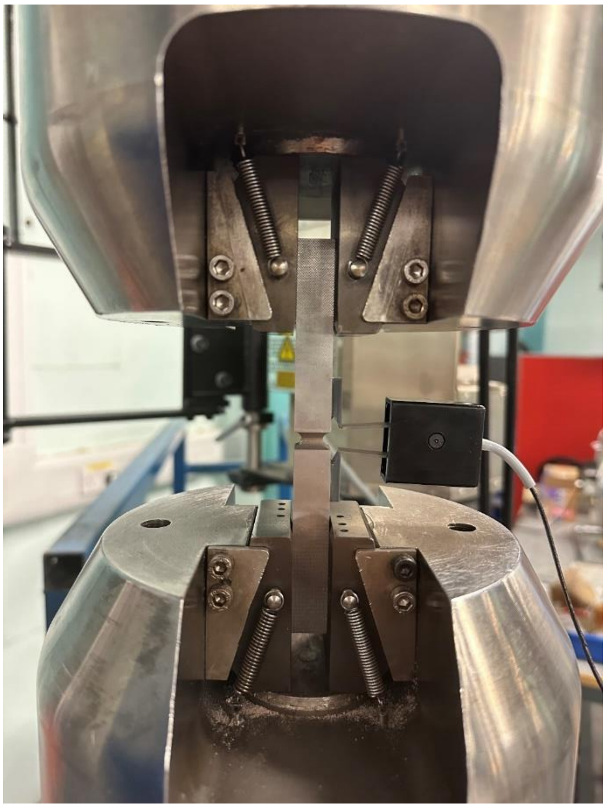

Figure 5.13. Fatigue tests by 100kN servo-hydraulic fatigue testing machine.

Both the proposed method and conventional stress-life method were also applied to the fatigue life evaluation of specimens without residual stress. The numerical and experimental results are shown in Figure 5.15, which illustrates the beneficial effect of induced compressive residual stress on the fatigue life of the specimens. All numerical and experimental results are summarized in Figure 5.16, which shows that the traditional stress-life method results in underestimation of fatigue life and the proposed fracture mechanics method gives a closer approximation of the measured fatigue life.

The experimental results for type A are tested by author [142] and type B are collected from [108], These results show good agreement between experiment and prediction based on S355 low carbon steel shown in Figure 5.17, indicating that the numerical fracture method based on ANSYS SMART crack growth simulation is suitable for calculating high cycle fatigue life with induced residual stress.

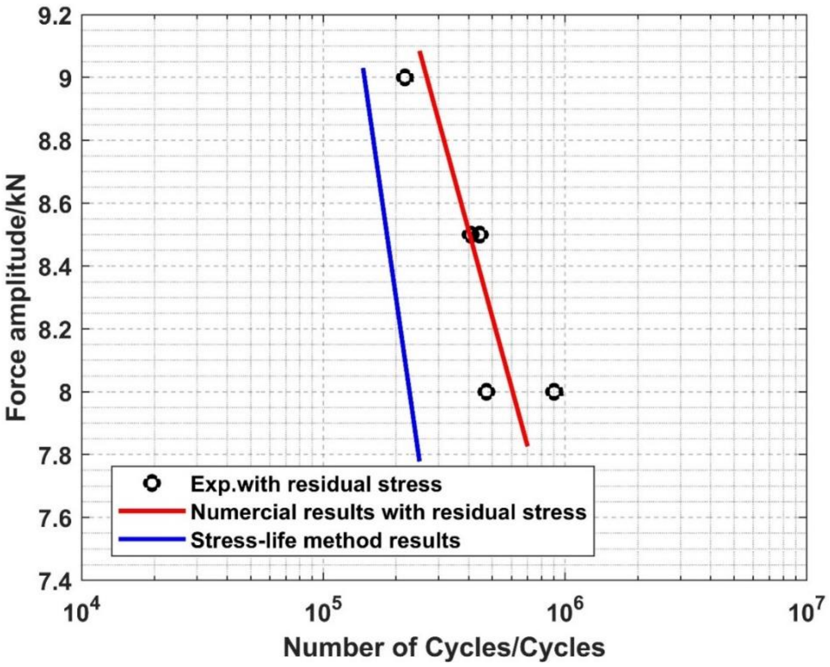

Figure 5.14. Calculated and experimental fatigue life for double-notch specimen with induced residual stress for type A.

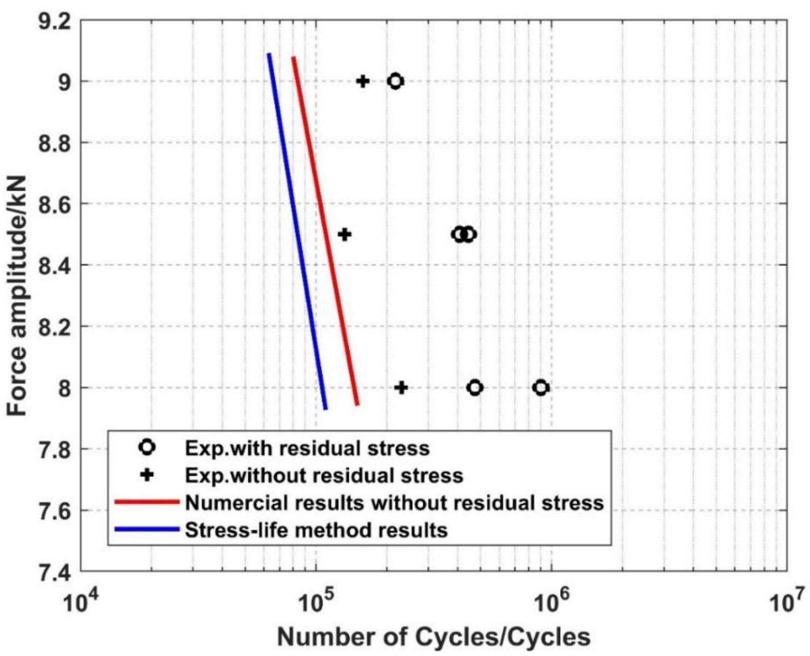

Figure 5.15. Calculated and experimental fatigue life for double-notch specimens with and without induced residual stress for type A.

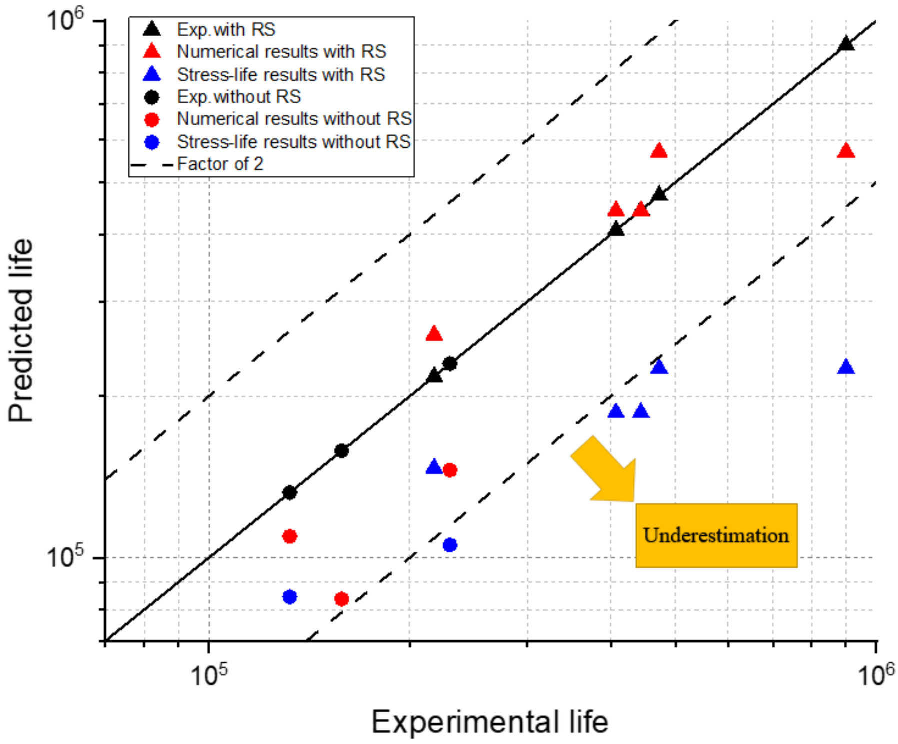

Figure 5.16. Comparison of calculated and experimental fatigue life results for type A.

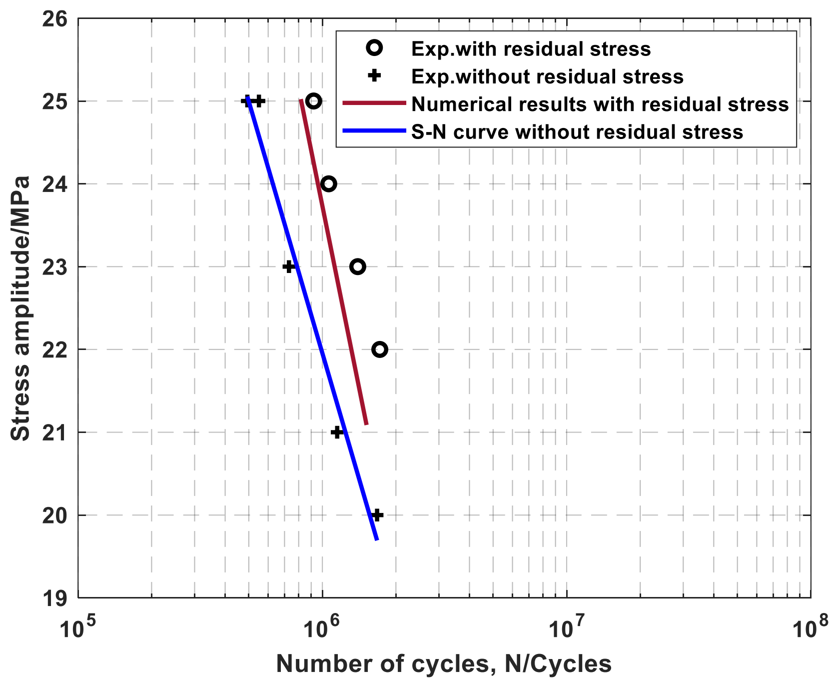

Figure 5.17. Calculated and experimental fatigue life for double-notch specimen including S-N curve of type B.

5.5 Discussion of Fatigue Life Prediction Method

In the present experimental investigation, consideration is limited to 316L stainless steel and S355 low carbon steel. However, the method extends established fracture mechanics methods and is therefore expected to be appropriate for a high cycle fatigue analysis of other materials under a cyclic loading regime where LEFM is valid. The analysis procedure requires definition of a material dependent initial crack length, proposed to be equivalent to the length of two material grains. For steels, this length was assumed to be $200\mu m$. The assumed crack initiation length for other materials will vary depending on material grain size but may be defined in a similar manner.

The method currently incorporates Physically Short Crack growth in the Long Crack growth model. More detailed consideration of the PSC would be expected to improve crack initiation life prediction. A further area for investigation is the use of polynomial equations to define variation in stress intensity factors with crack length. This approach enables a relatively simple application of the superposition method when calculating crack growth life for a varying stress ratio. However, minor differences in fracture parameters in the compressive residual stress region can significantly affect the calculated fatigue life, and further work is required to investigate the most appropriate fitting technique and to investigate the validity of the method when applied to other materials and component configurations.

Chapter 6 Fatigue Life Assessment of 3D Components

This section focuses on validating the accuracy of the proposed method by modifying the autofrettage loading from a tensile loading, as seen in the double-notched specimen, to an internal pressure which is common in industrial components. In addition, the validation process also incorporates considerations of the material. Furthermore, for complex components, more details such as the redistribution of the residual stress, the structure response after autofrettage and the influence of the crack tip plasticity will be discussed. Likewise, the calculated total fatigue life includes the crack initiation life and the crack growth life and the fatigue life obtained by the proposed method is compared to the tested results to investigate the accuracy of the method.

6.1 High-cycle Fatigue Life Estimation of Autofrettaged Blocks

The structural configuration of many valve and pump bodies can be simplified to a solid block of material with intersecting cross bores. Therefore, cross-bore blocks can be selected as a suitable instance to apply the methodology. Furthermore, the geometry of these blocks can also resemble the valve body or pump body. Therefore, the tested notched blocks shown in [31] is employed to validate the proposed method.

6.1.1 Notched-blocks and Material Properties

The geometry of the tested blocks in [31] is shown in Figure 6.1, which is a fluid end of a pump. There is a cross bore inside the block where the stress distribution is similar to it in double-notched structure as well. The critical point is located at the cross bore intersection where the highest stress concentration factor is. The component is made of 4340 austenitic steel, which is high strength steel used in the manufacturing of pressure vessels, aircraft landing gear, etc. The monotonic stress-strain curve of 4340 steel is fitted by the Ramberg-Osgood equation [152]. The material properties of 4340 austenitic steel [31, 153] are summarized in Table 6.1.

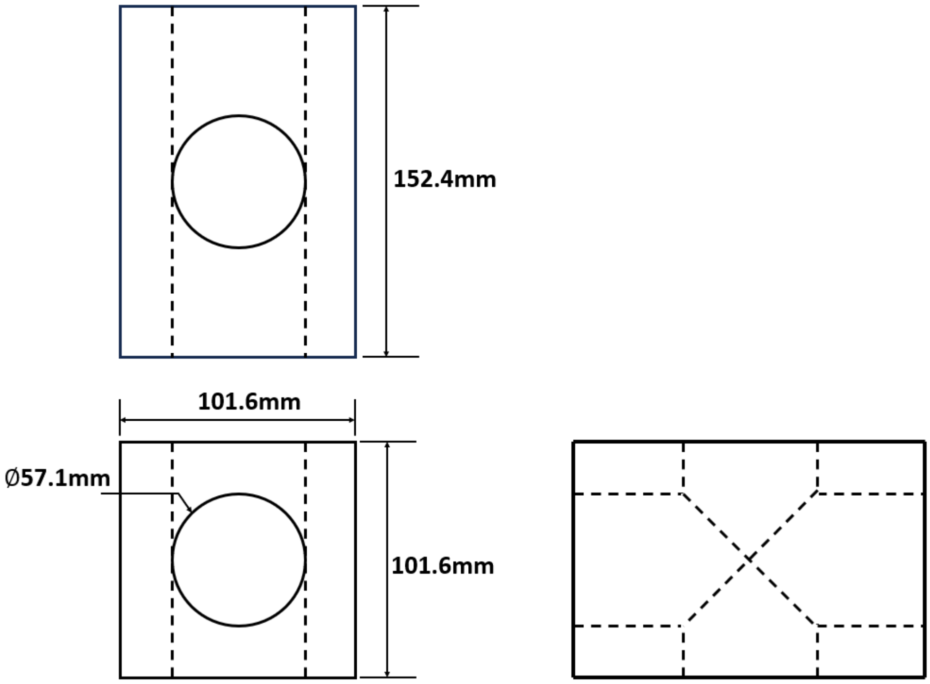

Figure 6.1. The geometry of the notched blocks [31].

Table 6.1. Material properties of 4340 steel.

	4340 steel
E/MPa	202462
σ_Y/MPa	620
σ_u/MPa	790
n'	0.07
K'	881
$C/\frac{mm/cycle}{(MPa\sqrt{m})^m}$	3.7×10^{-8}
m	2.5

6.1.2 Residual Stress Distribution and K_{rs}

Two autofrettage pressures, 103MPa and 122MPa, are considered to assess their impact on fatigue life. The compressive residual stress at the critical point on the cross bore intersection is calculated using FEA. A quarter of the component with symmetry boundary conditions is considered. The mesh and boundary conditions are shown in Figure 6.2 (a), where the mesh around the notch is refined by smaller elements. As only a quarter of the component is considered, frictionless supports are applied on the symmetry surfaces. The displacement Y on the bottom surface is 0 and the internal pressures are the autofrettage pressures, which are 103MPa and 122MPa. A multilinear kinematic hardening material model is employed, and the results of residual stress distribution are shown in Figure 6.3.

The maximum compressive residual stress under both autofrettage pressures considered is located at the notch root, with value 532.06MPa for a pressure of 122MPa and 355.17MPa for a pressure of 103MPa. After elastic-plastic analysis, the calculated residual stress distribution is exported to the crack propagation model.

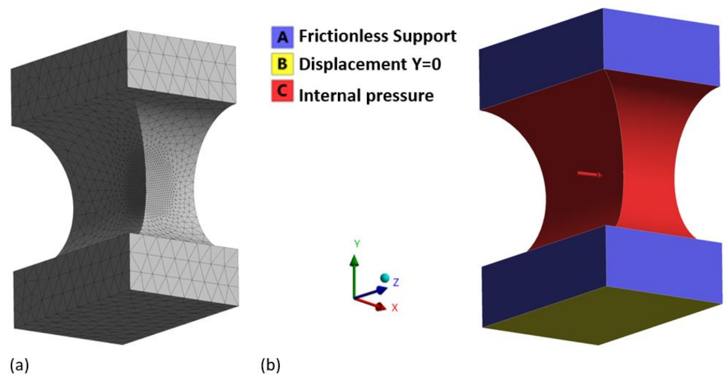

Figure 6.2. A quarter of notched-block. (a) Mesh results (b) Boundary conditions.

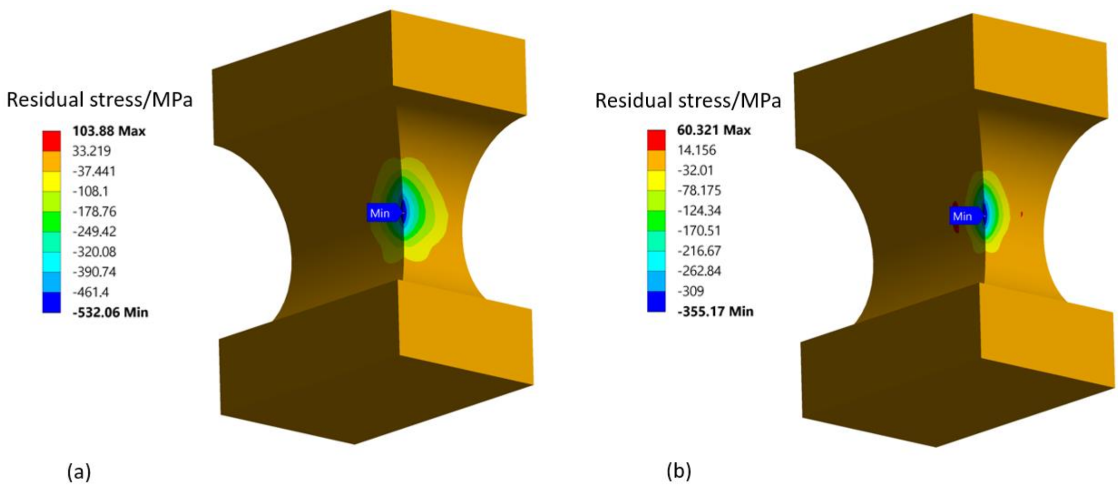

Figure 6.3. Residual stress (Normal stress on Y direction) distribution with different autofrettage pressure. (a) 122MPa (b) 103MPa.

Crack growth simulation is performed using the SMART crack growth tool. A 0.2mm crack initiation length is assumed at the notch root. An arbitrary internal pressure is applied, and the values of $\Delta K_{app} + K_{rs}$ calculated. Then, by the superposition method proposed in Section 4.3, the values of K_{rs} can be obtained by subtracting the results of ΔK_{app} (4.9) from the $\Delta K_{app} + K_{rs}$ and fitted by a crack length by polynomial function. The calculated results of K_{rs} for the two applied autofrettage pressures are shown in Figure 6.4. With varying autofrettage pressures, the minimum value of K_{rs} also varies. At an autofrettage pressure of 103MPa, the minimum value of K_{rs} is observed when the crack length is approximately 2mm. However, with an increase in autofrettage pressure to 122MPa, the minimum value occurs at a crack length of approximately 3mm. The calculated values of K_{rs} can thus be applied to calculate the crack growth life with the induced residual stress.

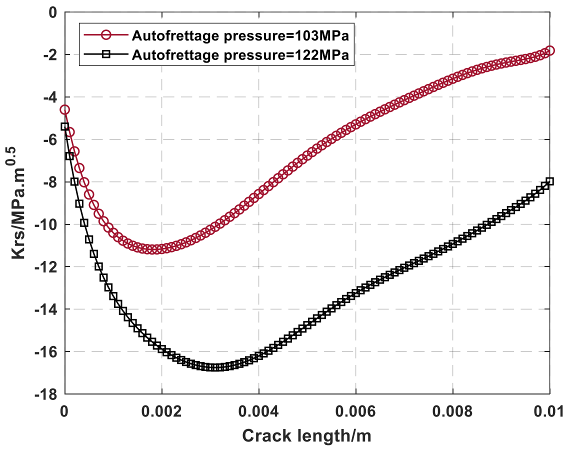

Figure 6.4. The results of K_{rs} with crack length under different autofrettage pressures.

6.1.3 Crack Growth Simulation and ΔK_{app}

The applied working pressure on the blocks after autofrettage is from 0 to 68.91MPa. The same procedures used in double-notched specimens in Chapter 5 is applied in this section to calculate ΔK_{app}. The coordinate system is created on the crack plane to determine the direction of the crack growth. The boundary conditions shown in Figure 6.2 (b) are also employed in crack growth simulation. The variation in ΔK_{app} with crack length is shown in Figure 6.5. As the crack propagates, the value of ΔK_{app} initially increases rapidly, followed by a slower rate of increase. Combining the results of K_{rs} obtained in Figure 6.4, the crack growth life with different autofrettage pressures can be calculated from (4.12) and (4.13).

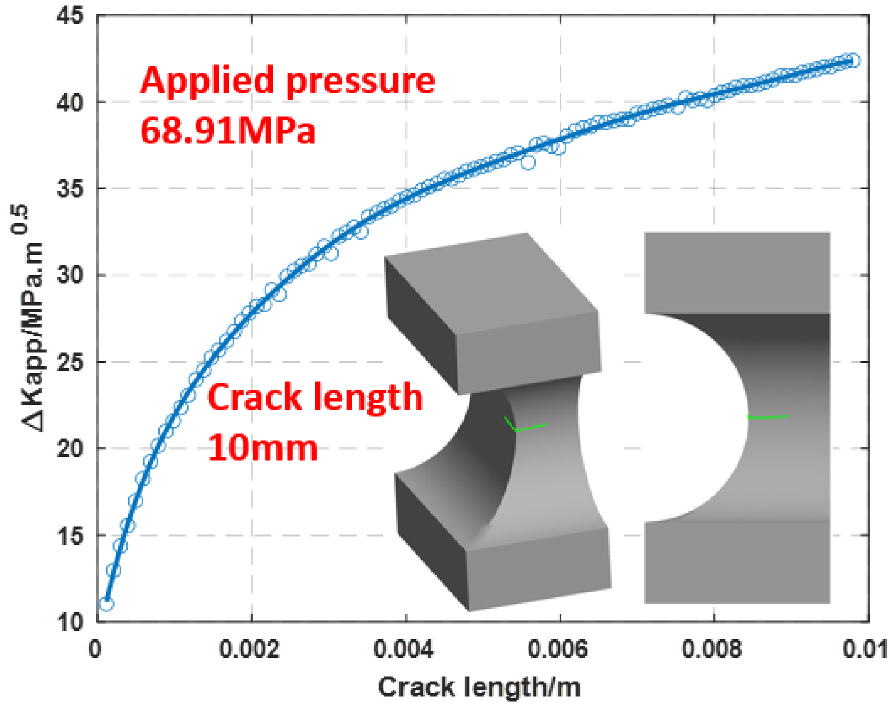

Figure 6.5. Calculated ΔK_{app} of 68.91MPa applied pressure.

6.1.4 Crack Initiation Life with Residual Stress

The crack initiation life with induced residual stress is calculated by a $S - N_i$ curve, which is created by the crack growth simulation described in Chapter 4. Based on an assumed crack initiation length, the crack growth life for different loads on a smooth standard tensile specimen can be calculated by FEA. The crack initiation life corresponding to the crack initiation length can then be determined by subtracting the crack growth life from the total life. The $S - N_t$ curve of 4340 steel based on the standard tested specimens is taken from Dowling [56], as shown as the solid line in Figure 6.6. The crack initiation life is calculated from the FEA and shown in Figure 6.6. The $S - N_t$ curve can be fitted by the Basquin equation (2.7) with $\sigma_f{}' = 907.5786\text{MPa}$ and $b = -0.066$.

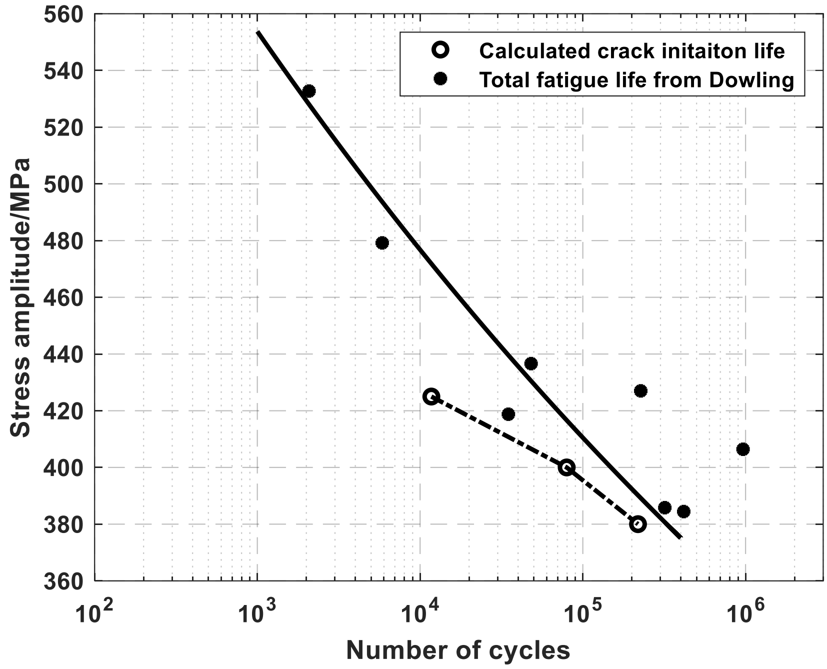

Figure 6.6. Crack initiation life and total life of 4340 steel.

The values of stress amplitude and mean stress for the different autofrettage pressures and single operating pressures and the experimental results of the total fatigue life are given in Table 6.2. Mean stress correction is performed using the Walker equation (2.11) to calculate the equivalent stress amplitude, which is substituted into Figure 6.6 to calculate the crack initiation life.

Table 6.2. Tested total fatigue life from [31].

Autofrettage Pressure/MPa	Operating Pressure/MPa	σ_a/MPa	σ_m/MPa	N_f
103	68.91	413.47	13.78	246,313
103	68.91	413.47	13.78	283,181
122	68.91	413.47	-80.90	422,426

6.1.5 Calculation of the Total Life

The crack propagation life with different autofrettage pressures is obtained by combining the results of K_{rs} shown in Figure 6.4 and ΔK_{app} in Figure 6.5. The total fatigue life is determined by adding the crack initiation life from Section 6.1.4. Results for the calculated life, including the crack initiation life and the crack growth life, are shown in Table 6.3. For 68.91MPa operating pressure, when the autofrettage pressure is 103MPa, the calculated total life based on the proposed method is around 259,600 cycles. Comparing this with the experimental results provided in Table 6.2, where the experimental results range between 246,313 cycles and 283,181 cycles, the calculated result falls within this range. The errors are 5.39% and 8.33% respectively, both of which are small in the estimation of fatigue life. Only one test is reported for autofrettage pressure 122MPa, resulting in a tested fatigue life of 422,426 cycles. The calculated fatigue life is 502,170 cycles with an error of 18%. Although this error is larger than when the autofrettage pressure is 103MPa, the scatter factor is only 1.2 which is less than 2 and still acceptable for fatigue life prediction.

Table 6.3. Calculated total life by proposed method.

Autofrettage Pressure/MPa	Operating Pressure/MPa	N_g	N_i	N_t
103	68.91	190,600	69,000	259,600
122	68.91	402,170	100,000	502,170

6.1.6 Discussion of the Notched Block Fatigue Life Prediction

In this section, the proposed method applied for the double-notched specimens is employed to predict the fatigue life of autofrettaged notched blocks made of 4340 steel. For a constant 68.91MPa operating pressure, the fatigue life is obtained for two autofrettage pressures, and the calculated fatigue lives have good agreement with the experimental results. Therefore, the feasibility of the proposed method discussed in Section 5.5, including the assumption of crack imitation, the determination of the stress intensity factor of residual stress and its influence on the stress ratio, can be validated. Additionally, due to the universality of the geometry of the notched block, the proposed method can be used in many industrial structures with notches, such as pumps, valves and pipes.

All of the analyses are based on the realm of high cycle fatigue, with a specific emphasis on elastic shakedown. After autofrettage, the structure response under subsequent cyclic loading may be either ratcheting or shakedown.

Thus far, the analysis has been assumed elastic shakedown. The following section will consider both elastic shakedown and plastic shakedown, which means the structure response will be considered with more complex components.

6.2 Fatigue Life Estimation of Autofrettaged Injection System Components

In industrial equipment such as injection pumps and engines, injection systems are widely used under high cyclic injection pressure. Once the injection pressure is determined, the structure must be designed to meet the fatigue life requirements under these cyclic pressures. If the shape and material of a component, and no additional methods are employed to enhance its fatigue resistance, then the fatigue life and limit are constant. Therefore, since no structure changes can be made, autofrettage is applied to injection system component to increase the fatigue life and the proposed method can then be employed to estimate the fatigue life.

6.2.1 Injection System Component and Material Properties

An injection system component for a diesel engine [107] is considered to validate the proposed fatigue life method. The component is simplified as shown in Figure 6.7.

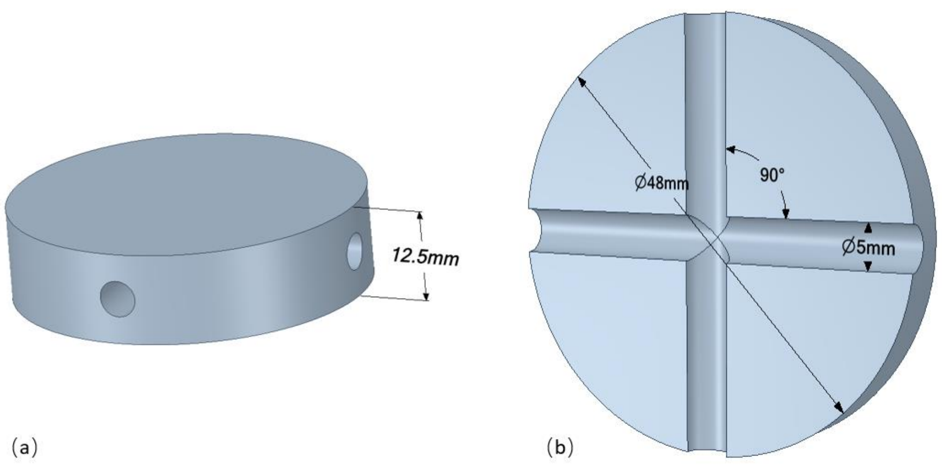

Figure 6.7. (a) The geometry of the entire component. (b) The geometry of the half of the component.

The component material is 42CrMo4. A mixed hardening model (3.11) is applied for cyclic stress-strain analysis. The mixed hardening model consists of nonlinear isotropic hardening model and Chaboche kinematic hardening model (3.9). The material properties of 42CrMo4 under room temperature [107] applied in the constitutive model are shown in Table 6.4.

Table 6.4. Material properties of 42CrMo4.

	42CrMo4
Isotropic elasticity	
E	200 GPa
v	0.3
Nonlinear isotropic hardening	
k	910 MPa
R_∞	-283.17
b	11.527
Chaboche kinematic hardening	
C_1	6.758×10^{-6} MPa
γ_1	5123
C_2	9303 MPa
γ_2	1281
C_3	80269.9
γ_3	320
C_4	4.589×10^{-4} MPa
γ_4	80
C_5	12295.6
γ_5	20

6.2.2 Autofrettage and Residual Stress Distribution

The autofrettage pressure applied to the structure is 850 MPa. During loading, plasticity is induced in the high stress concentration area identified in Figure 6.8. The residual stress distribution on unloading is simulated using FEA. Subsequently, the component is subjected to cyclic working pressure ranging from 350 MPa to 5 MPa.

One sixteenth of the component, with appropriate symmetry boundary conditions, is modelled to calculate the compressive residual stress. The structure is meshed using tetrahedral elements, with refined meshing around the notch root area, which is the high stress concentration region. The mesh comprises 8685 elements and 15334 nodes, as shown in Figure 6.8.

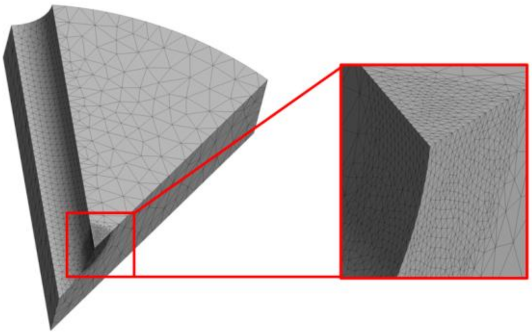

Figure 6.8. Mesh results of one sixteenth of the structure.

Symmetry boundary conditions are applied on three surfaces of the model, with the autofrettage pressure applied on the internal surface, as shown in Figure 6.9.

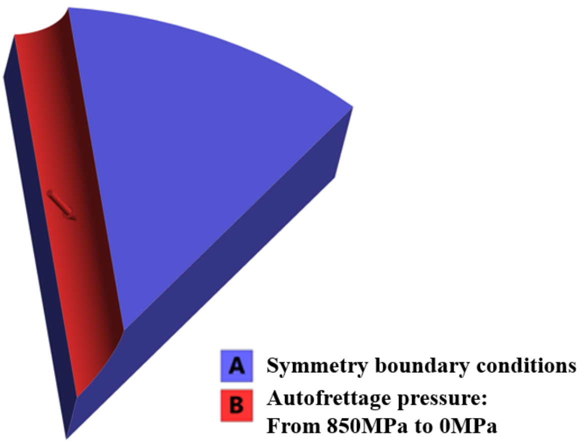

Figure 6.9. Boundary conditions of one sixteenth structure.

The compressive residual stress is represented by the normal stress perpendicular to the crack surface. The residual stress of the entire model after the 850 MPa autofrettage is shown in Figure 6.10 (a). The residual stress distribution around the notch root, along the expected crack path from point 1 to point 2 is shown in Figure 6.10 (b).

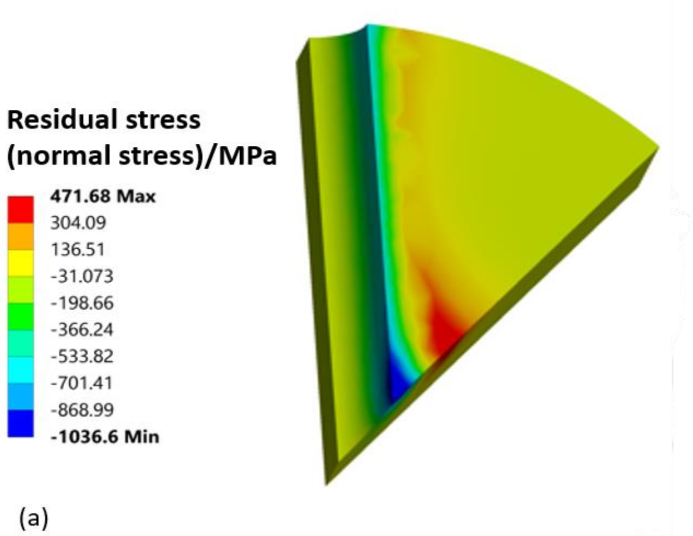

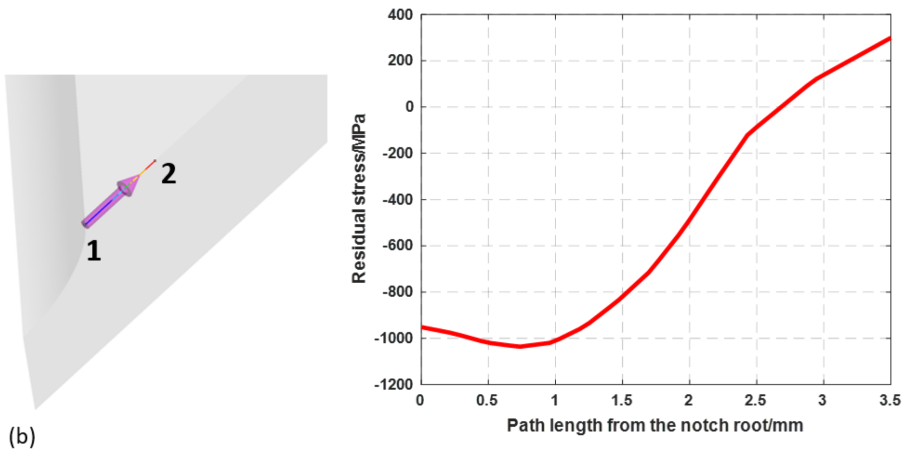

Figure 6.10. Residual stress (Normal stress perpendicular to the section) distribution due to autofrettage pressure. (a) Residual stress on the entire structure. (b) residual stress along the path.

As shown in Figure 6.10, compressive residual stress is distributed around the notch root, with a value of 951.55 MPa at the critical point (point 1). Tensile residual stress is then distributed away from the notch root to balance the compressive stress distribution.

6.2.3 Residual Stress Redistribution

After autofrettage, the structure's response to cyclic loading, with the induced compressive residual stress, can be classified as elastic shakedown, plastic shakedown, or ratcheting, as discussed in Section 3.4. If plastic shakedown occurs, redistribution of residual stress must be considered, and the redistributed compressive residual stress can be assumed as the compressive stress of the stable hysteresis loop. To determine whether such redistribution should be accounted for, the plastic strain state is a crucial factor for assessment. If the plastic strain remains constant under subsequent cyclic loading following autofrettage, the structural response can be assessed as elastic shakedown, as illustrated by the blue line in Figure 6.11. When the subsequent cyclic loading range is from 5MPa to 100MPa, the equivalent plastic strain is constant after the autofrettage. However, when the subsequent cyclic loading range is from 5MPa to 350MPa, the plastic strain varies in each step in the first few cycles, as shown by the red line in Figure 6.11. Plastic shakedown may then occur in the following cycles. Therefore, to obtain the redistributed residual stress, stress-strain analysis needs to be applied for more load cycles.

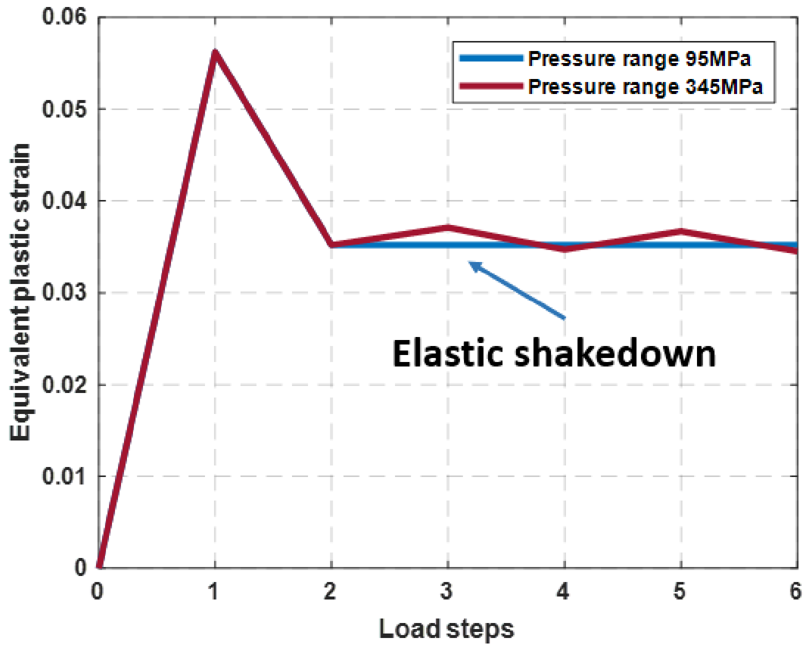

Figure 6.11. Equivalent plastic strain with various pressure ranges.

The autofrettaged structure is subjected to subsequent cyclic pressure ranging from 350 MPa to 5 MPa for a total of 250 cycles. The results of redistributed residual stress on the critical point for each load step are shown in Figure 6.12, where the residual stress becomes stable after around 50 cycles. In addition, the results of residual stress along the path after various cycles are also shown in Figure 6.13. The compressive residual stress on the critical point decreases from the original 951.55MPa to 786.81MPa after 250 cycles, and the redistributed residual stress is also different. After 20 cycles, the redistributed compressive residual stress is around 800MPa and be stable with the increasing of the cycles. The residual stress becomes stable after approximately 100 cycles. Therefore, the redistributed residual stress after 100 cycles can be used for the following fracture mechanics analysis when the pressure range is from 5MPa to 350MPa.

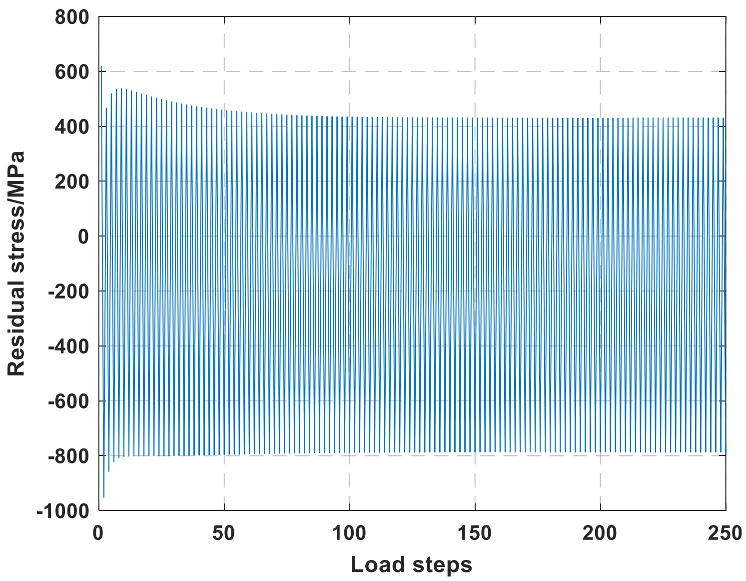

Figure 6.12. Residual stress on the critical point for each step.

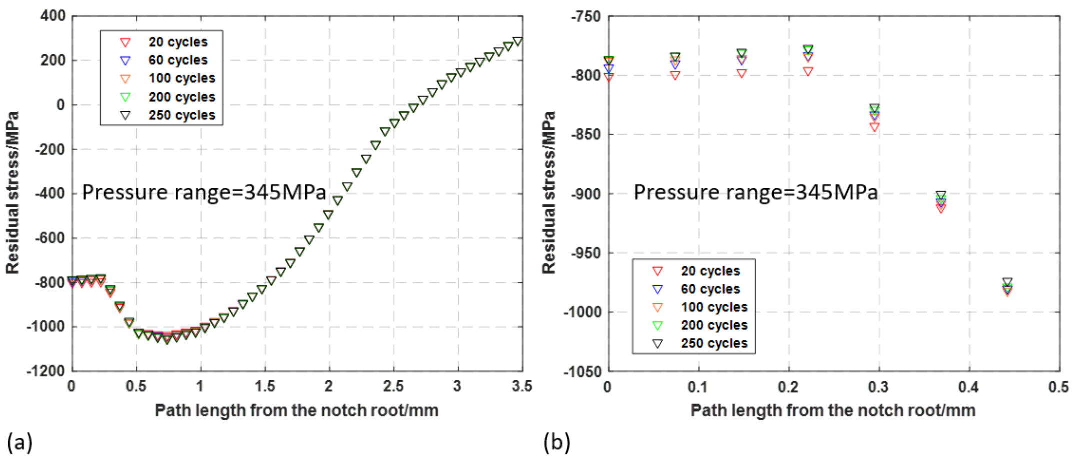

Figure 6.13. Residual stress redistribution after various cycles. (a) Path length to 3.5mm. (b) Path length to 0.5mm.

With different pressure ranges, the calculated compressive residual stress at the critical point also varies. The results of the redistributed residual stress along the path after 250 cycles under three pressure ranges are shown in Figure 6.14. The stable compressive residual stress at the critical point increases with the increasing pressure ranges after 250 cycles. Residual stress distributions around the notch root vary under different pressure ranges within 0 to 0.8mm along the path, but beyond approximately 1mm, the residual stress gradually converges to the same value.

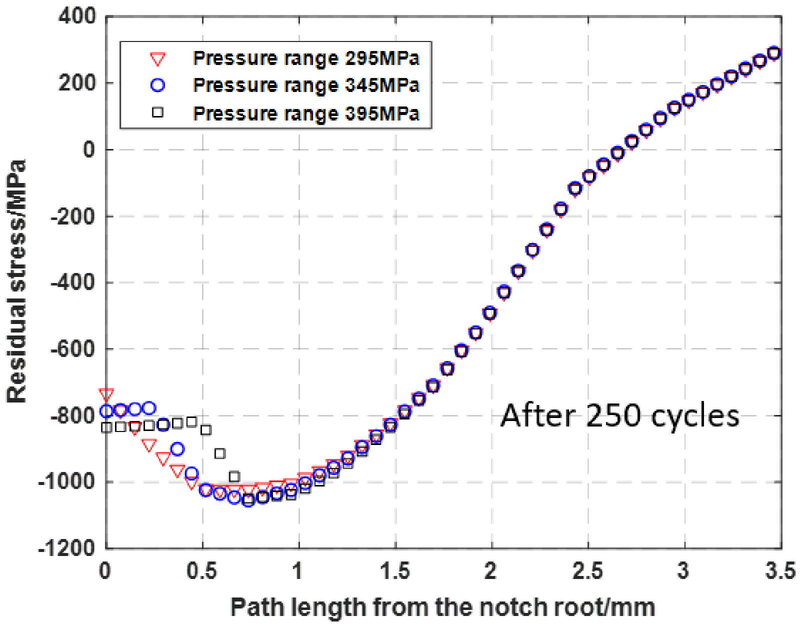

Figure 6.14. Redistributed residual stress after 250 cycles with various pressure ranges.

The determined redistributed residual stress is then applied in the following crack growth simulation.

6.2.4 Stress Intensity Factor of Applied Pressure

The SMART tool is used to simulate crack growth, employing a quarter of the component for this purpose. An assumed initiation crack, inserted as a semi-elliptical crack with a length of 0.2mm, is placed at the notch root. A quarter of the component is meshed using tetrahedral elements, with refinement around the crack front as shown in the Figure 6.15. The mesh includes 30643 elements with 44705 nodes.

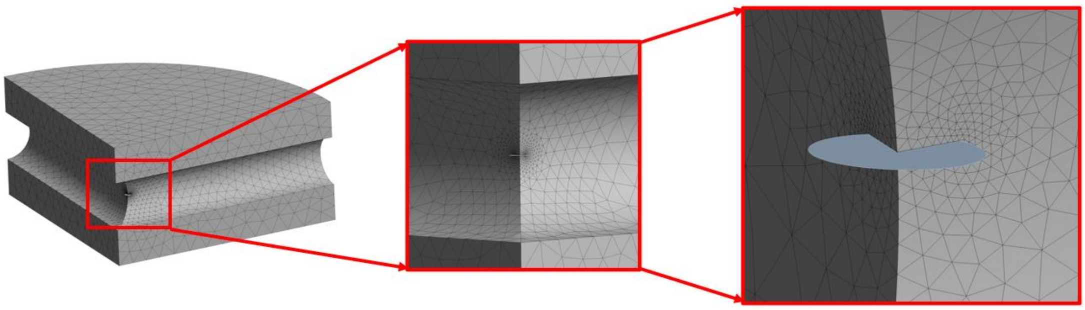

Figure 6.15. Mesh results of a quarter of the structure with crack initiation.

As a quarter of the structure is modelled, with appropriate symmetry boundary conditions, and internal pressure applied. In addition, displacement constrain is imposed on the bottom plane as Y=0. All boundary conditions are shown in Figure 6.16.

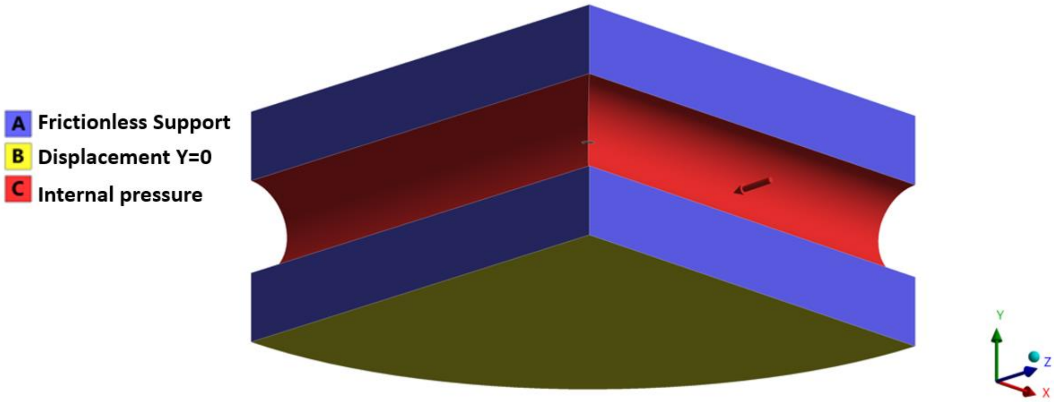

Figure 6.16. Boundary conditions of quarter of the structure.

Several internal pressures are applied to the model for crack growth simulation to calculate the results of stress intensity factors, as shown in Figure 6.17. Although, stress intensity factors may vary with changes in internal pressures, the configuration factor Y remains constant and is dependent only on the geometry of the structure. Consequently, Y can be employed to assess mesh sensitivity and, once obtained, can be applied to calculate the SIFs for any internal pressure. The values of Y with crack length based on the mesh results shown in Figure 6.15 are shown in Figure 6.18. Although, the pressures applied to the structure are different, the calculated results of Y are same. A second mesh with different refinement is analysed to evaluate mesh sensitivity by comparing the values of Y. Since increasing mesh density also leads to longer computational times, the comparison is conducted only for crack lengths ranging from 0.2mm to 1mm. The results of Y obtained based on different mesh densities are shown in Figure 6.19.

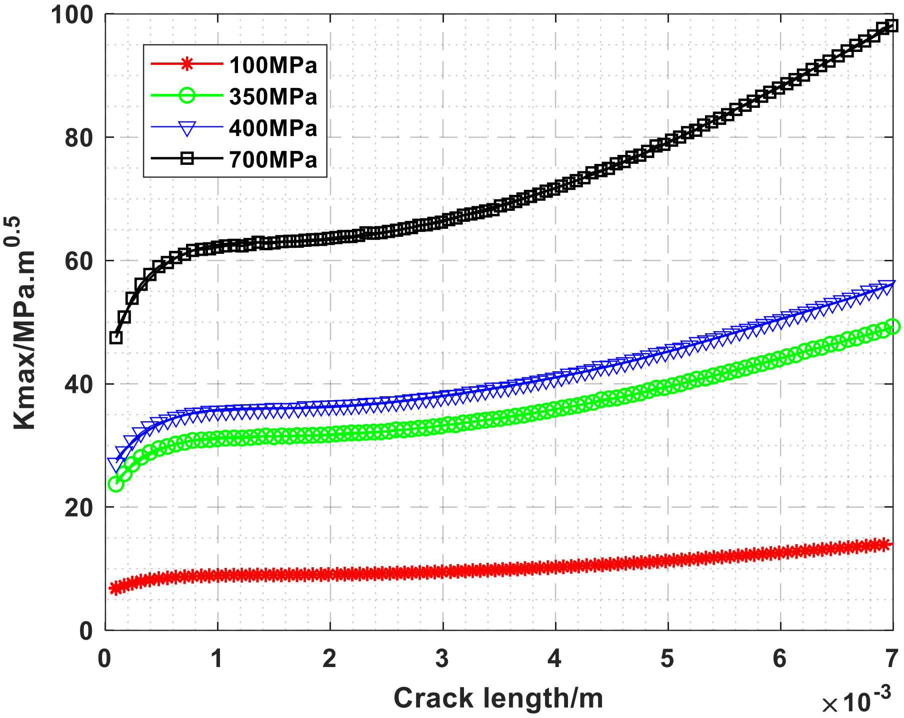

Figure 6.17. Stress intensity factors of various internal pressures.

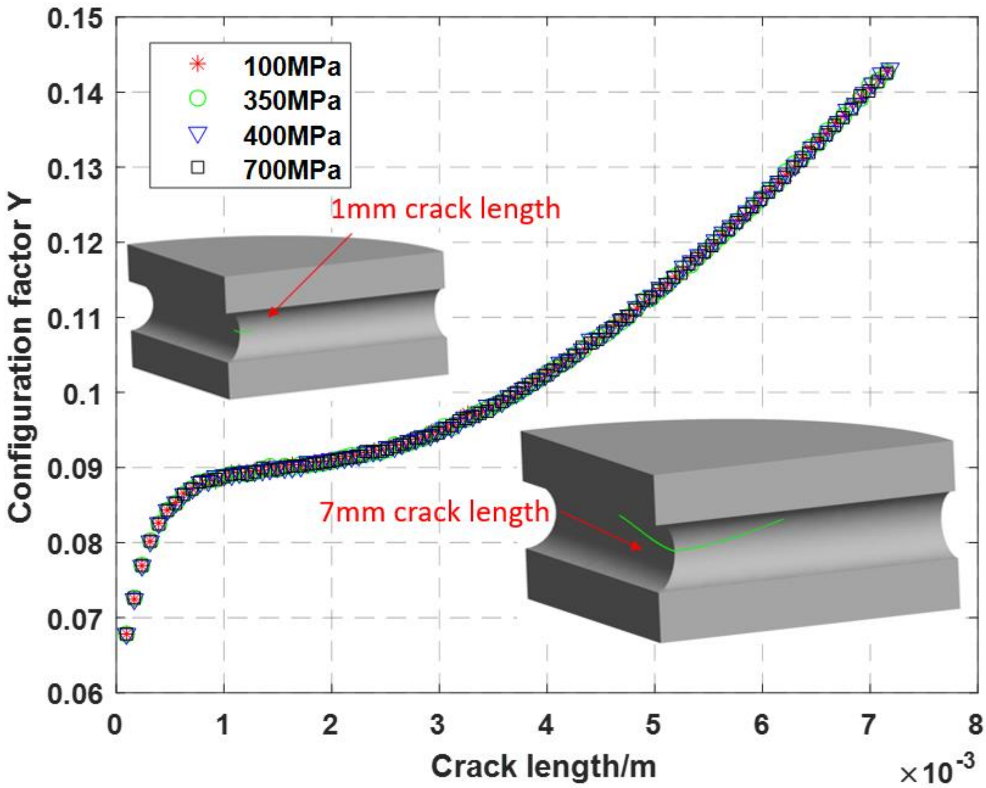

Figure 6.18. Configuration factor Y with crack length.

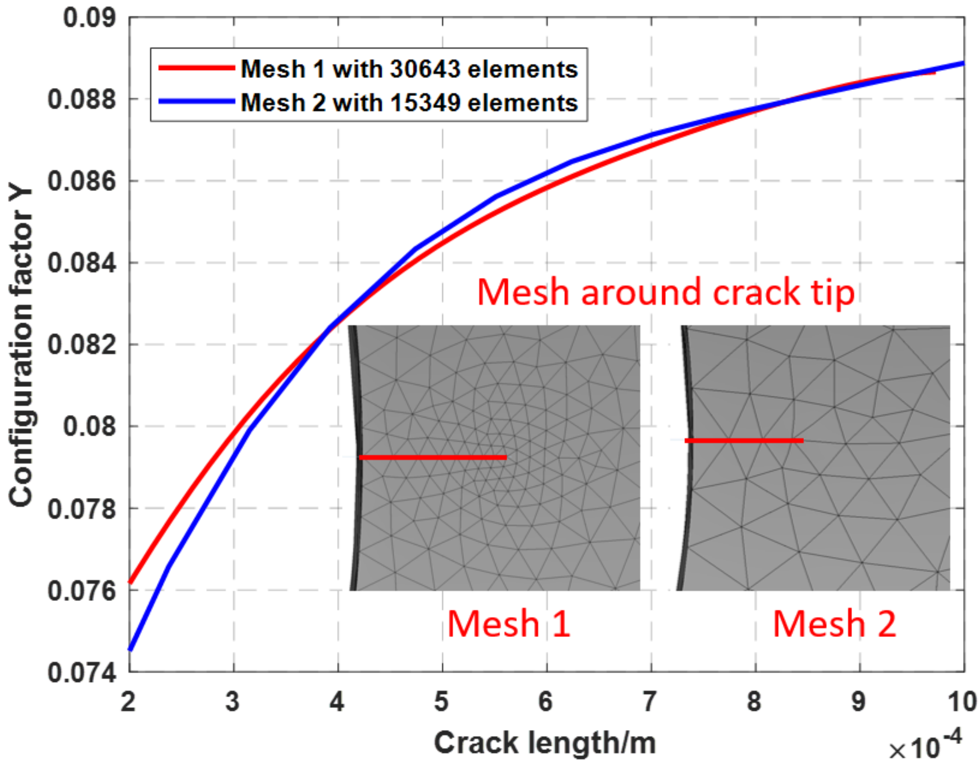

Figure 6.19.ConfigurationfactorY with different mesh densities.

As shown in Figure 6.19, the mesh around the crack tip is refined leading to an increase in the number of elements from 15349 in Mesh 2 to 30643 in Mesh 1. Initially, there is a small difference in the results of Y, but with the growth of the crack initiation, the difference diminishes and finally two lines representing Y converge into one line after approximately 0.8mm. Considering the insensitivity of Y values to mesh density and the significant increase in computational time, the mesh with 15349 elements is employed in the subsequent analysis.

6.2.5 Crack Tip Plasticity Correction

The SMART crack growth tool in ANSYS is employed to simulate the crack growth and calculate the applied stress intensity factors. It is based on the LEFM, which assumes small scale yield (Section 2.7.5). In the small scale yield assumption, the plastic zone at the crack tip should be much smaller than the crack length itself. To define this “much smaller” assumption, the minimum required dimensions of the crack, according to Dowling [56] and ASTM standard [154], is:

$$a, (W-a), h \geq \frac{4}{\pi}\left(\frac{K}{\sigma_Y}\right)^2 \ or \ \frac{4}{\pi}\left(\frac{K_{max}}{\sigma_Y}\right)^2 \tag{6.1}$$

where, a is crack length, $W-a$ is ligament length, and h is height. In this component, only one dimension, crack length, is considered as the SIFs are already correlated to the crack length by fitting functions. (6.1) can then be solved to find the minimum crack length to satisfy the small scale yield assumption. The solutions of the minimum crack length with various maximum applied pressures are shown in Table 6.5.

Table 6.5. Calculated minimum crack length with applied pressures.

Applied pressure/MPA	400	350	300	250	200	150
Calculated Crack length/mm	1.3	1	0.7	0.44	0.2	0.11

As shown in Table 6.5, the calculated minimum crack length decreases with the decrease of the applied pressure. Since, the SMART crack growth is based on the LEFM, to investigate the plastic zone induced with plasticity, the FEA of elastic-plastic fracture mechanics is employed. However, unlike the SMART crack growth tool which can simulate the process of crack propagation continuously, incorporating plasticity into the calculation does not allow continuous simulation. The stress distributions around the crack tip depicted by the equivalent stress under 400 and 200 maximum applied stress are illustrated respectively as Figure 6.20. The description of the plastic zone obtained by the plastic material model when the maximum applied pressure is 200MPa is shown in Figure 6.20 (a). Compared to the Figure 6.20 **(c)**, determined by the 400MPa, the plastic zone under 200MPa is smaller.

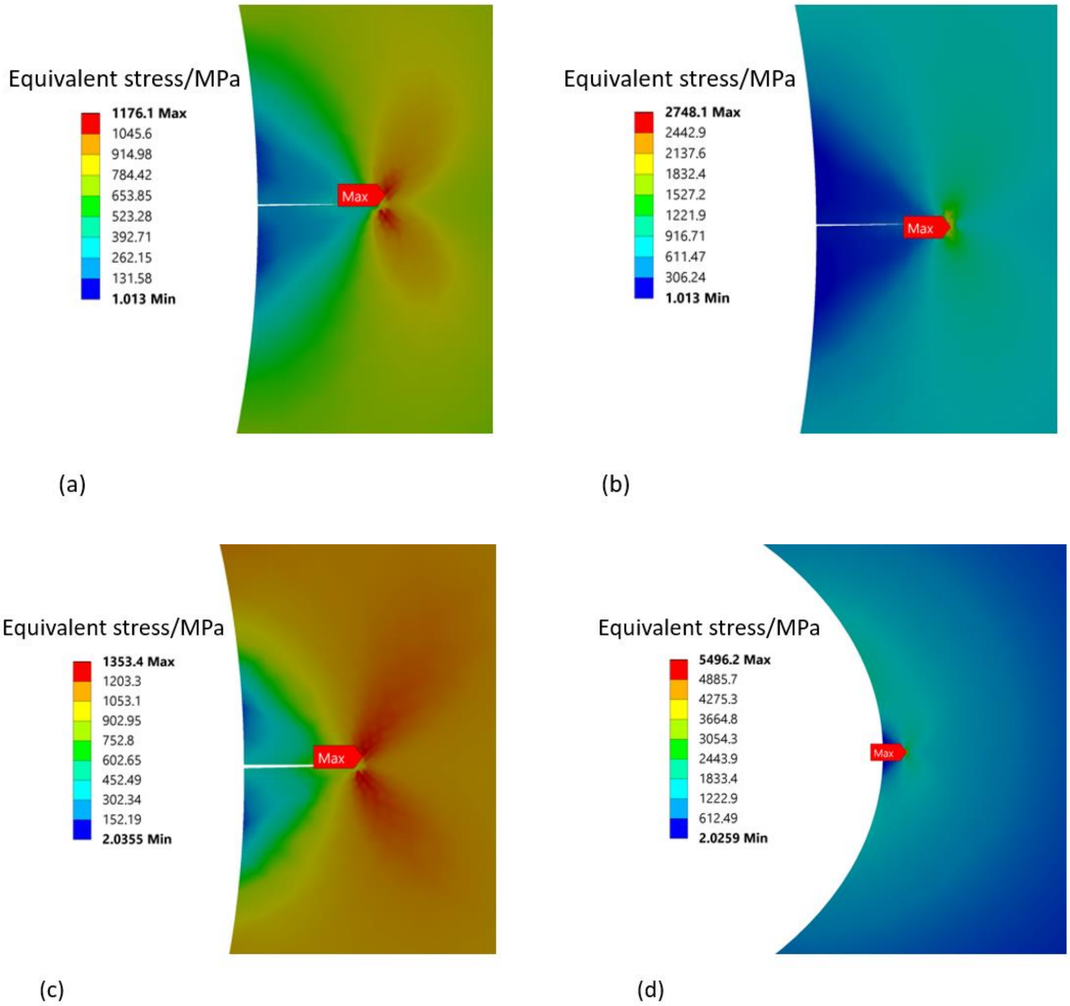

Figure 6.20. Stress distributions described by equivalent stress (a) 200MPa, plasticity (b) 200MPa, elasticity (c) 400MPa, plasticity. (d) 400MPa, plasticity (magnified displacement view).

In addition, when the applied pressure is 200MPa, although, the value of the calculated equivalent stress under the elastic material model is different from that under the plastic material model, the shape and size of plastic zones in different loads are similar, as shown in Figure 6.20 (a) and (c). However, in the same situation, the result of the plastic zone with 400MPa applied pressure in plastic model has a significant difference compared to the stress distribution in the elastic model, as shown in Figure 6.20 (b) and (d).

The structure response under the various applied pressures in Table 6.5 is determined from the equivalent plastic strain. As mentioned in Section 3.4, if there is no net increment in the plastic strain, the structure response can be defined as a shakedown.

If the plastic strain is constant during any loading steps, the stress-strain response is termed as elastic shakedown, and if the plastic strain varies under loading and unloading steps, but the net plastic strain is zero, the stress-strain response is identified as a plastic shakedown. The calculated equivalent plastic strain under various applied pressures are shown in Figure 6.21. When the applied pressure is 200MPa, following autofrettage, the equivalent plastic strain remains constant during subsequent loading, indicating that the structure's response is characterized by elastic shakedown. However, as the applied pressure increases to either 300MPa or 400MPa, plastic shakedown occurs.

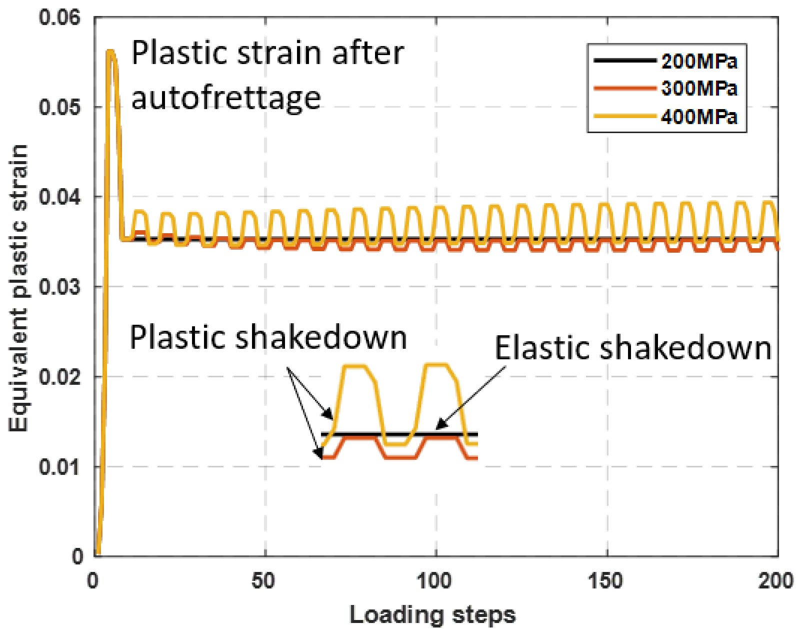

Figure 6.21. Equivalent plastic strain with applied pressures.

Considering the results shown in Table 6.5, the calculated minimum crack length is small (around 0.2mm) when the structure response is an elastic shakedown. As the length of assumed initiation crack is 0.2mm, the plastic influence on the simulated stress intensity factors can be ignored when elastic shakedown occurs. However, if plastic shakedown occurs, the calculated minimum crack length is larger than 0.7mm, which is larger than the assumed crack initiation length. The plasticity influence should hence be considered for the crack propagation from the 0.2mm crack initiation length to the calculated minimum crack length. However, as the SMART crack growth tool in ANSYS is based on the LEFM, other methods need to be employed. Here, the stress intensity factor with plasticity is determined by multistep analysis that the process of crack growth before the minimum crack length is divided into several steps, for each step, the SIF is calculated independently. For instance, if the minimum crack length is larger than 0.2mm, the crack growth path between 0.2mm and the minimum crack length are divided by multistep and the value of SIF of each step is calculated based on elastic-plastic material model. Then, the SMART crack growth tool is employed until the 0.2mm crack initiation grows to the minimum crack length.

To determine the range of stress intensity factors, the minimum SIFs obtained by the minimum pressure 5 MPa are calculated based on the configuration factor shown in Figure 6.19, as in (4.2) in Section 4.1.2. Several ranges of SIFs under various ranges of applied pressures are then calculated, as shown in Figure 6.22.

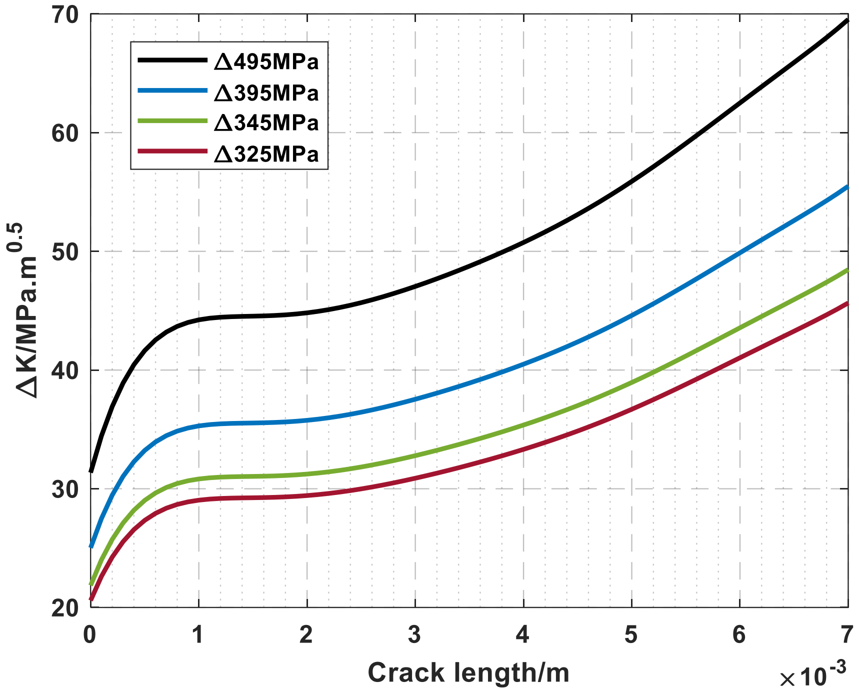

Figure 6.22. Range of stress intensity factors with minimum pressure 5 MPa.

6.2.6 Stress Intensity Factor of Residual Stress

As noted in Section 4.3, the stress intensity factor of residual stress, K_{rs} can be determined by the weight function method, which is the method applied in [107].

However, this is difficult to apply in 3D models. Therefore, the FEA method based on the superposition method of Section 5.3.2 is applied to determine K_{rs}.

The redistributed residual stress is exported from the mixed hardening material model and employed as the initial stress state for the crack simulation. An arbitrary pressure, sufficiently large to induce crack growth with the residual stress, is applied to the structure. Following the crack growth simulation, the values of $\Delta K_{app} + K_{rs}$ are determined along with the crack length a. Additionally, another crack growth simulation is conducted with only the same arbitrary pressure applied to obtain the values of ΔK_{app}. Consequently, the results of K_{rs} can be determined by subtracting ΔK_{app} from $\Delta K_{app} + K_{rs}$. The value of K_{rs} can then be calculated as shown in Figure 6.23.

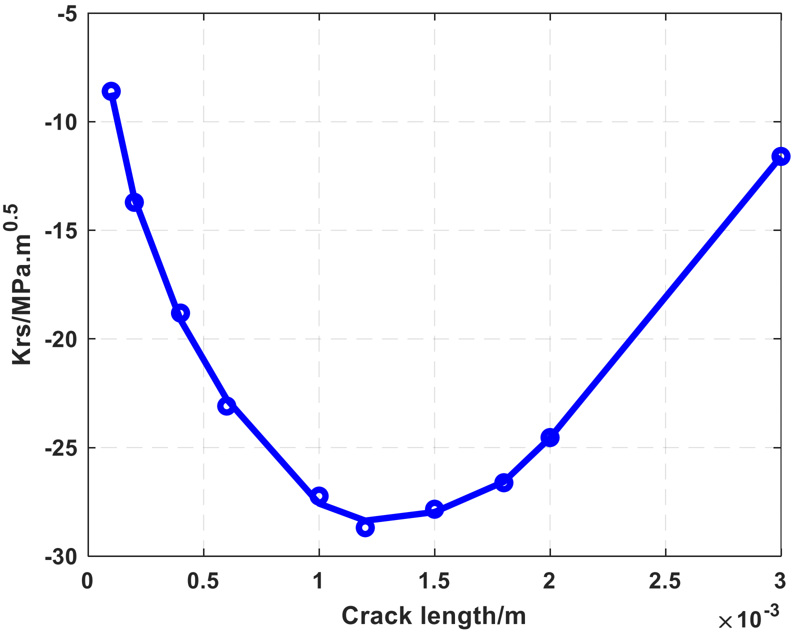

Figure 6.23. K_{rs} with crack length.

6.2.7 Calculation of Crack Initiation Life with and without Residual Stress

To calculate the crack initiation life, the methodology shown in the Section 4.1 is applied. The stress-total fatigue life curve is collected from the reference [155]. Assuming a 0.2mm crack initiation length, the crack growth life for the smooth specimen illustrated in Figure 4.2 is calculated based on Paris law (4.5) with the Paris law parameters for 42CRMo4, where C is 6.08×10^{8} MPa$\sqrt{m}$ and m is 2.3

[156]. Finally, the crack initiation life based on the assumed crack initiation length for the smooth specimen is calculated for different applied stresses and a stress-crack initiation life, $S - N_i$, curve for 42CrMo4 is generated, as shown in Figure 6.24.

With the stress amplitude obtained from the FEA, the crack initiation life is determined by applying the calculated stress amplitude to the $S - N_i$ curve. After autofrettage and 250 working load cycles, the stress state response is as shown in Figure 6.25. The results of equivalent stress amplitude after mean stress correction based on several cyclic loading are summarized in Table 6.6.

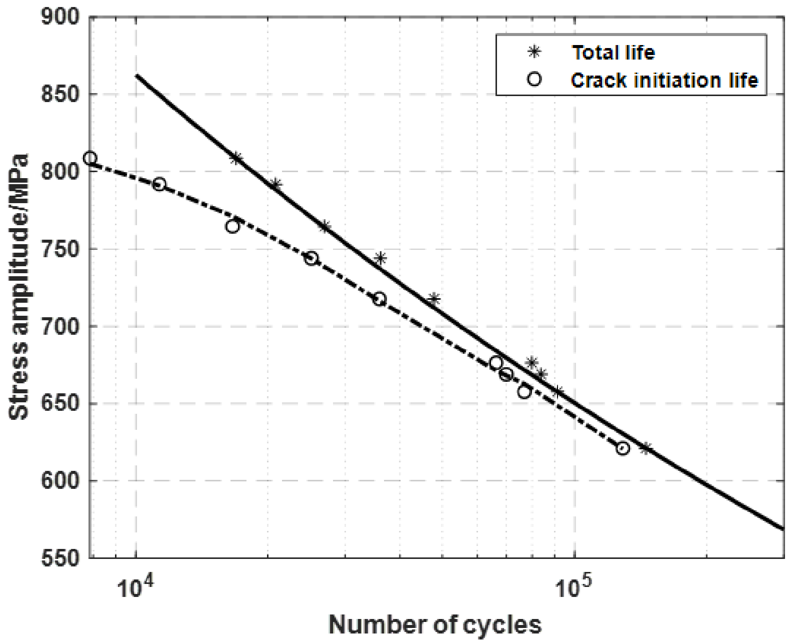

Figure 6.24. Crack initiation life of 42CrMo4 under various stress amplitude.

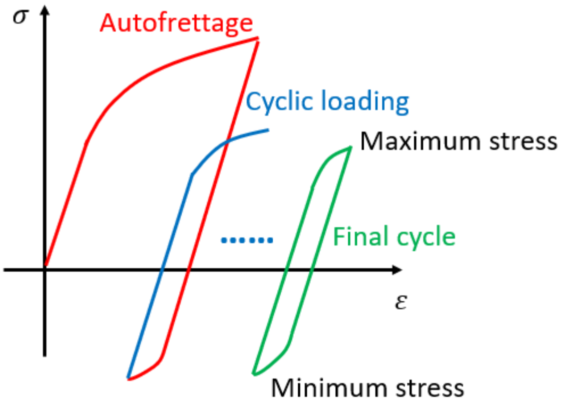

Figure 6.25. Illustration of stress response due to autofrettage and cyclic loading.

Table 6.6. Calculated equivalent stress amplitude with residual stress by FEA.

Cyclic pressure range/MPa	Equivalent stress amplitude/MPa
400	817.02
375	792.74
350	767.36

Without autofrettage, the stress state response to applied pressures can be either elastic shakedown or plastic shakedown. The results of equivalent stress amplitude corresponding to the applied pressures and stress-stain states are summarized in Table 6.7.

Table 6.7. Calculated equivalent stress amplitude without residual stress by FEA.

Cyclic pressure range/MPa	Equivalent stress amplitude/MPa
300	928.78
200	681.9
150	595.5

6.2.8 Calculation of Crack Growth Life with and without Residual Stress

Equations (4.12) and (4.13) are applied to calculate the crack propagation life considering residual stress. ΔK_{app}, K_{rs} and R_{eff} are functions of crack length, enabling calculation of crack propagation life by integrating over crack length. Three maximum working pressures ranging from 5 MPa to 405MPa, 380MPa and 355MPa are applied. The range of SIFs for the applied pressures, ΔK_{app}, are obtained from the configuration factor shown in Figure 6.18. The results of crack propagation life without the residual stress can be calculated directly by ΔK_{app} from (4.5) and by combining the values of K_{rs} and the influence of R_{eff}, the results of crack propagation life can be calculated. These results are then combined with the crack initiation life determined in Section 6.2.7 to calculate the total fatigue life with and without residual stress.

The comparison of the total life results considering residual stress obtained by the proposed method with the results included in the Reference [107] is illustrated in Figure 6.26. In [107], a strip yield model incorporating plastic effect is employing the concept of a fictitious crack tip, is applied to estimate the crack growth life. The results of predicted fatigue life based on this model are shown as the red line in Figure 6.26. The results of fatigue life obtained by LEFM calculation and experiments [107] are shown as the blue line and green line respectively. The fatigue life results obtained by the proposed method, shown as the black symbols in Figure 6.26, are between the linear calculation and the strip yield model. Compared to the weight function method, the determination of K_{rs} in the proposed method is significantly easier in 3D model and with plasticity correction on the proposed method, the FEA results can also provide closer results on the fatigue life compared with LEFM.

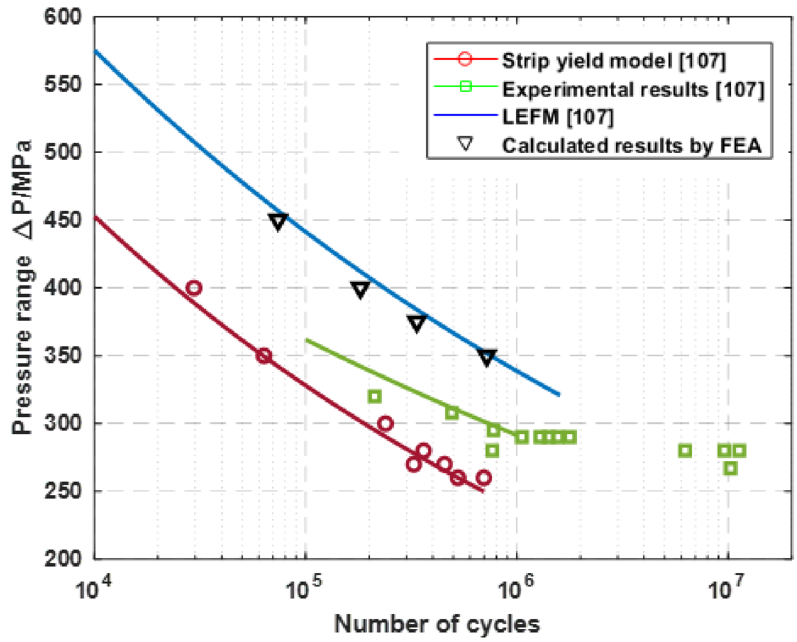

Figure 6.26. Prediction of total fatigue life with residual stress by various methods.

The results of total life without the residual stress are shown in Figure 6.27. The calculated fatigue life by strip yield model, linear calculation and FEA method proposed are included. The calculated results by FEA without the residual stress are also seen to give good agreement with experimental results.

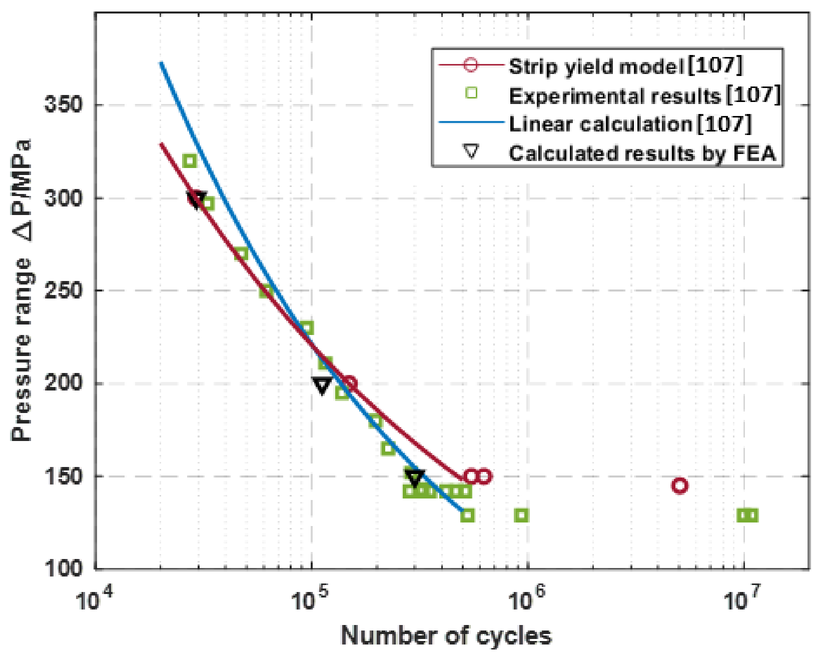

Figure 6.27. Prediction of total fatigue life without residual stress by various methods.

6.2.9 Discussion

The method proposed in Chapter 4 to assess fatigue life with induced residual stress through the crack growth model with an assumed initial crack was applied to double-notched specimens of 316L stainless steel and low carbon steel in Chapter 5. As the redistributed residual stress varies after initial cyclic loadings before stabilizing, the residual stress after approximate 100 cyclic loadings is taken as the final redistributed residual stress. The crack initiation length is assumed as 0.2mm. Based on the assumed crack initiation, the values of SIF under various applied pressures are determined by the SMART crack growth tool. However, the small scale yield assumption in LEFM may not be satisfy before the 0.2mm assumed crack initiation length is established. The minimum crack length required to satisfy the small-scale yield assumption varies with different applied pressures and corresponds to the structure's response. In cases where the structure response is identified as a plastic shakedown, the minimum crack length satisfying the assumption is larger than approximately 0.7mm. However, under the condition of elastic shakedown, the minimum crack length is approximately 0.2mm, which aligns with the length of the assumed crack initiation. Therefore, when the response of a structure is elastic shakedown, if the crack initiation length is 0.2mm, the influence of plasticity on the crack tip can be ignored, but for the plastic shakedown, the plasticity should be considered in the calculation of SIF. Here, the SIF with plasticity is calculated by multistep analysis of the initial crack length and SMART crack growth is applied after the minimum crack length.

Based on the assumed crack initiation length, the $S - N_i$ curve of 42CrMo4 can be generated. Same procedures included in the proposed method in Figure 4.1 are applied. By adding the crack initiation life, the total life is obtained as shown in Figure 6.26 and Figure 6.27. For the situation with the residual stress, the deviations between the calculated fatigue life and experimental results are close for both the strip yield model and LEFM calculation method. The calculated life using the proposed method closely resembles the LEFM calculation, but with less deviation. For the situation without the residual stress, compared with the strip yield model, the results from the linear calculation can have less deviation and the calculated life by the proposed method can provide a good agreement as well.

Chapter 7 Crack arrest

From a design perspective, the aim of autofrettage for a given working load cycle may be to achieve a specific finite fatigue life, typically 10^6 to 10^7 cycles for high cycle fatigue, or infinite fatigue life. The minimum autofrettage pressure required to achieve this aim can be determined by applying a stress life or fracture mechanics methodology to a component with induced compressive residual stress, calculated by elastic-plastic analysis. Here, a method is proposed to determine the minimum autofrettage pressure according to crack arrest analysis. The calculated ΔK_{eff} (4.15) is compared with a crack threshold model to determine if the crack will propagate or be arrested as shown in Figure 7.1. The minimum autofrettage pressure can be determined at which the crack arrest occurs.

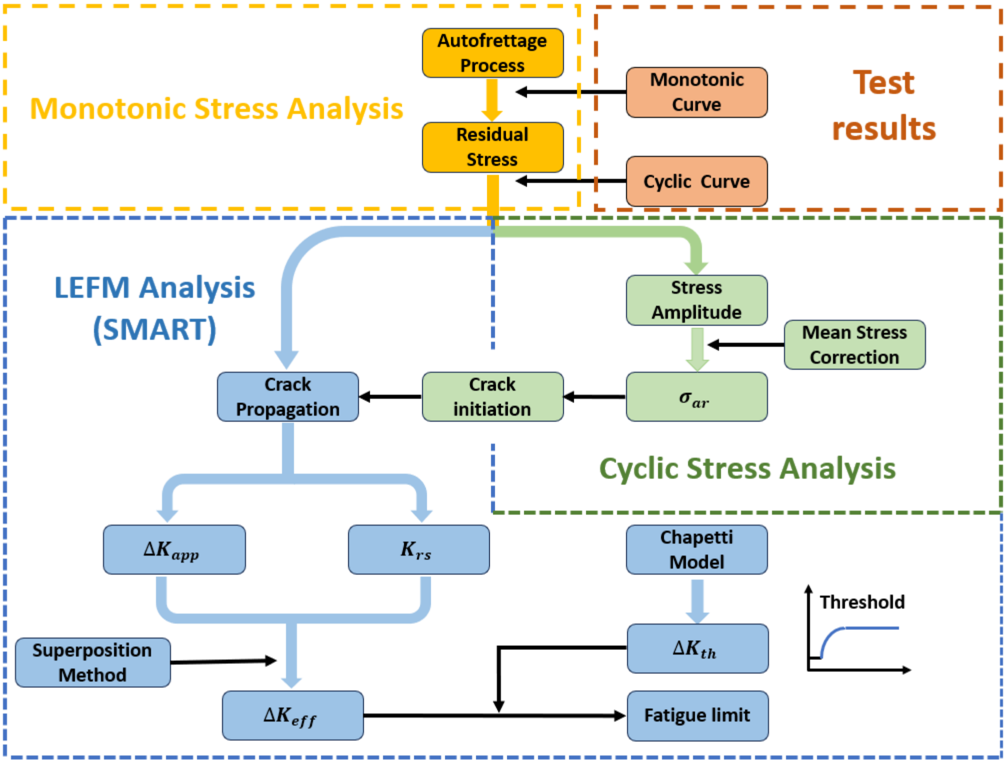

Figure 7.1. Flow diagram of crack arrest analysis.

This chapter investigates the incorporation of the crack arrest models and the threshold of EI Haddad [79] and Chapetti [82] in the methodology. Both models are initially considered in fatigue analysis of double notch tensile test specimens with compressive residual stress induced by initial tensile overload. Results are compared with fatigue test results from the literature and experiments. The procedure with the Chapetti crack arrest model is then applied to a complex 3D valve body with autofrettage residual stress, previously considered by Sellen et al.[157]

7.1 Crack Arrest Theory

Crack arrest analysis can be applied for the assessment of autofrettage to make sure the preload in the autofrettage process can improve the total fatigue life larger than at least 10^6 cycles. The crack arrest analysis can be employed by comparing the SIFs with the thresholds mentioned in Section 2.7.2. Crack arrest analysis based on the EI Haddad and Chapetti models has been considered in several investigations. Arau ĵo and Nowell [80] and de Pannemaecker [81] adopted the EI Haddad model for crack arrest analysis in fretting fatigue. Chapetti [158] assessed fatigue strength by comparing the threshold curve with ΔK. Chapetti assumed a semicircular crack, with $Y = 0.65$. Santus and Taylor [71] have proposed a semi-ellipse form where Y is dependent on the aspect ratio, with $Y = 0.746$ assumed for an aspect ratio of 0.8. A similar IBESS approach [159] was proposed for the fatigue assessment of welding structures.

Crack arrest analysis taking account of autofrettage pressure was investigated for cruciform specimens by Thumser et.al [160] in terms of ΔK_{dR}. This applies to cracks within the MSC region, but when defining crack arrest in general it is necessary to consider variation in the PSC threshold with a, $\Delta K_{th,a}$, as illustrated in Figure 2.16. Even if ΔK exceeds ΔK_{dR}, there is still a possibility of arresting the crack by increasing $\Delta K_{th,a}$.

7.2 Crack Arrest Assessment on Double-notched Specimens

Two types of double-notched specimens shown in Figure 5.1 are investigated. The material properties required to calculate the thresholds are summarized in Table 7.1.

Table 7.1. Experimental and collected material properties of 316L and S355 (R=0) [56, 108, 142, 161, 162].

Material	σ_Y (MPa)	E (GPa)	$\Delta\sigma_{eR}$ (MPa)	ΔK_{thR} $(MPa\sqrt{m})$	d_1 (mm)	ΔK_{dR} $(MPa\sqrt{m})$	k (mm^{-1})
316L	255	200	292	5.5	0.024	1.64	4.46
S355	255	200	344	8	0.055	2.94	2.64

The EI Haddad (2.39) and Chapetti (2.42) fatigue threshold models for 316L and S355 determined from the material properties of Table 7.1 are shown in Figure 7.2, where ΔK_{th} for the Chapetti model assumes $Y = 0.65$.

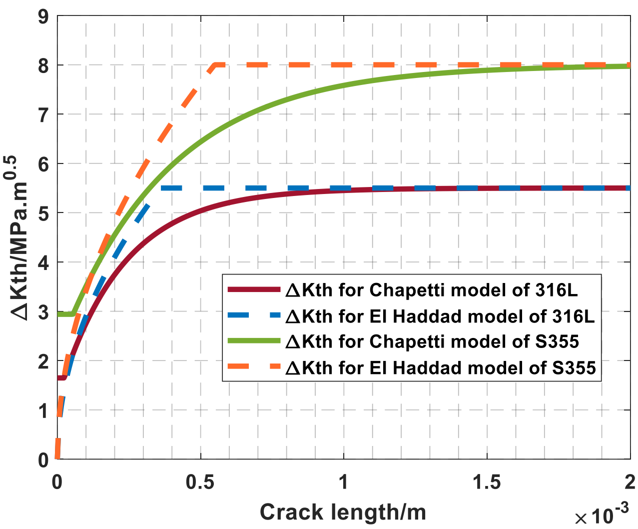

Figure 7.2. Calculated fatigue threshold models for 316L and S355.

As a PSC develops from an MSC, crack arrest will occur if the effective SIF range ΔK_{eff} for a given crack length a is below the corresponding fatigue crack threshold ΔK_{th}. The effective SIF range for Specimens A and B can be determined from the numerical results for ΔK_{app}, K_{rs} and R_{eff}, ΔK_{eff} calculated from (4.15).

The threshold and effective SIF ranges for Specimens A and B are plotted against crack length a for Specimens A and B in Figure 7.3 (a) and (b) respectively. For Specimen A, the Chapetti model predicts crack arrest for applied forces of 6.5kN, 7.0kN and 7.5kN. The EI Haddad also predicts crack arrest for these forces and for the higher force of 8.0kN. For Specimen B, the Chapetti model predicts crack arrest in the PSC region for applied force amplitude 21kN and 22kN. The EI Haddad model predicts crack arrest for 21kN.

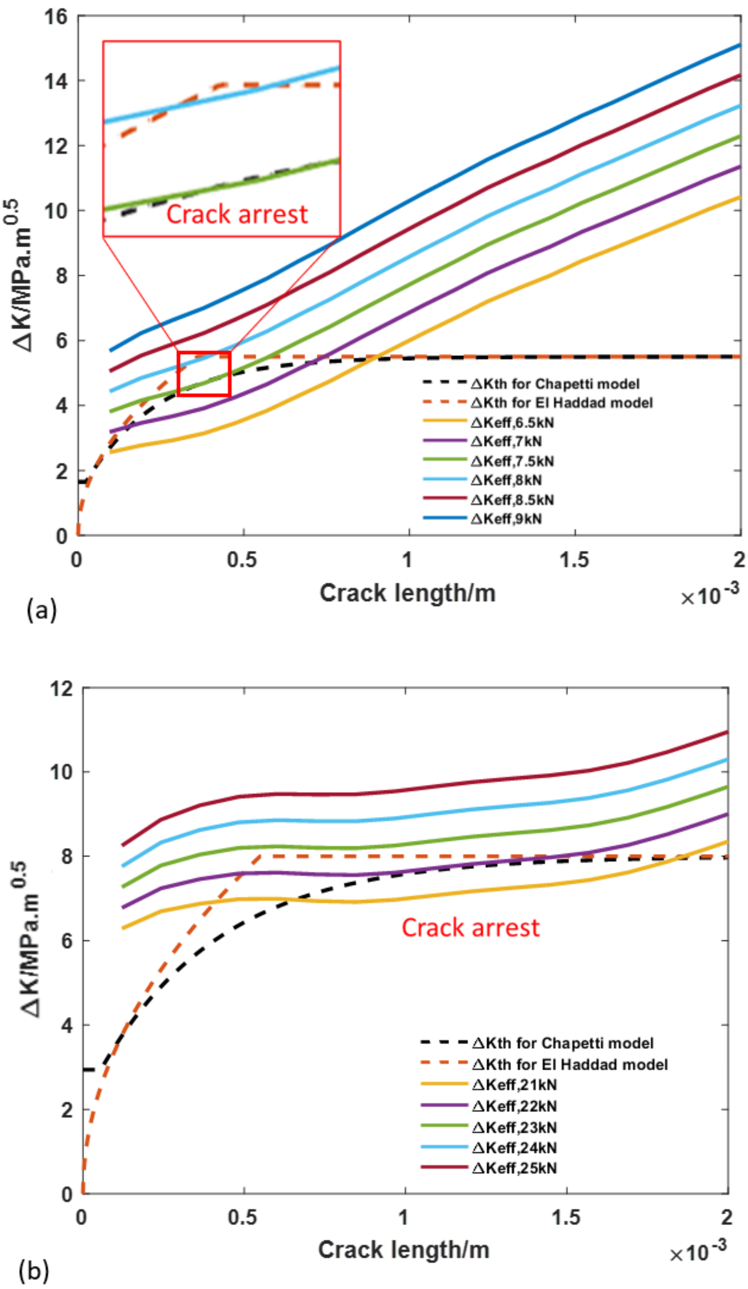

Figure 7.3. Calculated ΔK_{eff} compared with ΔK_{th} a) Specimen A and b) Specimen B.

Test results for fatigue cycles to failure for the Specimen A and Specimen B [108] are summarised in Figure 7.4(a) and (b) respectively where the fatigue limit (more than at least 2×10^6) are marked as red points.

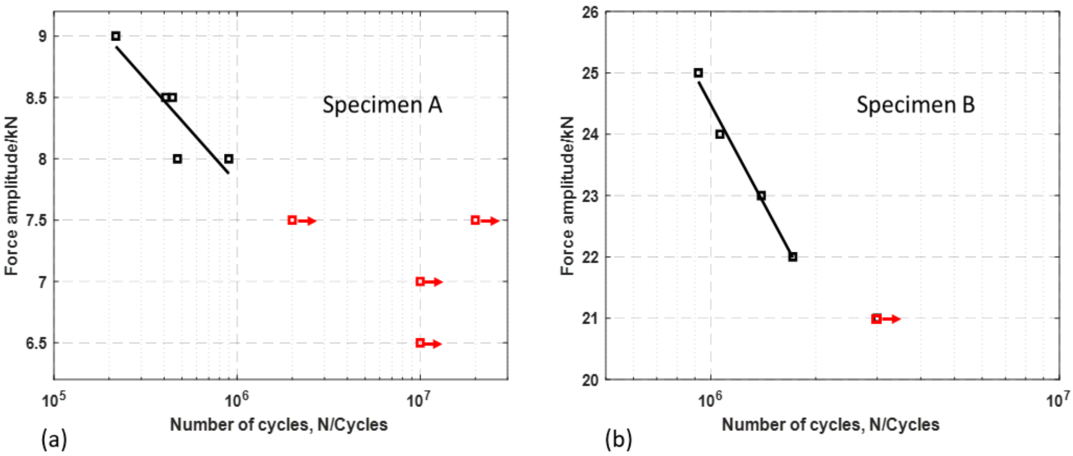

Figure 7.4. Experimental results of fatigue tests of preloaded double-notched specimens a) Specimen A and b) Specimen B[108].

The results for Specimen A show a finite fatigue life for an applied working force of 8kN and above. This shows that crack arrest does not occur at 8kN, as predicted using the El Haddad model. Test results corresponding to the Chapetti model prediction of crack arrest at working load 7.5 kN show run-out at $2x10^6$ and $2x10^7$ cycles. The Specimen B results show finite fatigue life for a working force of 22 kN and above, showing that crack arrest does not occur at 22kN as predicted using the El Haddad model. A single test corresponding to the Chapetti prediction of crack arrest at 21kN shows run-out at $3x10^6$ cycles.

Comparison with fatigue test results indicates that the El Haddad model does not give a conservative estimate of crack arrest within the framework of the proposed method. However, the results given by the Chapetti model indicate that it is a potentially viable approach, within the limits of the run-out data available.

7.3 Influence of Aspect Ratio

For crack propagation simulation in FEA, the crack initiation can be assumed as semicircular, straight-fronted or semi-ellipse, but commonly the shape of crack initiation is considered as either semicircular or semi-ellipse. Based on Chapetti's theory, the value of Y can be generally determined as 0.65. In Taylor's work, he refined the value of Y through the specific shape of semicircular crack initiation and by assuming the aspect ratio is 0.8 to obtain Y=0.746. Therefore, for more accurate prediction, it is necessary to consider the influence of aspect ratio on crack propagation simulation and the fatigue limit prediction. Although, the aspect ratio changes with the crack propagation, the aspect ratio of the initial crack length is commonly assumed between 0.2 and 1.0 [124]. According to initial aspect ratios, the value of the corresponding Y is based on [124].

Since the ΔK_{th} dependent on Chapetti model has been considered in Figure 7.2 and aspect ratio of 0.2 is rarely applied in crack growth simulation, only aspect ratios of 0.4, 0.6 and 0.8 are discussed. For crack propagation simulation, the crack initiation length a is still constant at 0.2mm. Based on several aspect ratios, different sizes of semi-ellipse cracks are applied in two kinds of specimens, with the same procedures to calculate the values of ΔK_{app}, K_{rs} and ΔK_{eff}. The results of ΔK_{eff} and ΔK_{th} with different aspect ratios for the two specimens are shown in Figure 7.5.

For specimen A, 8kN force amplitude is applied and 23kN force amplitude is applied on specimen B. Based on Figure 7.4, both of these selected force amplitudes are close to the fatigue limit forces of the corresponding specimens.

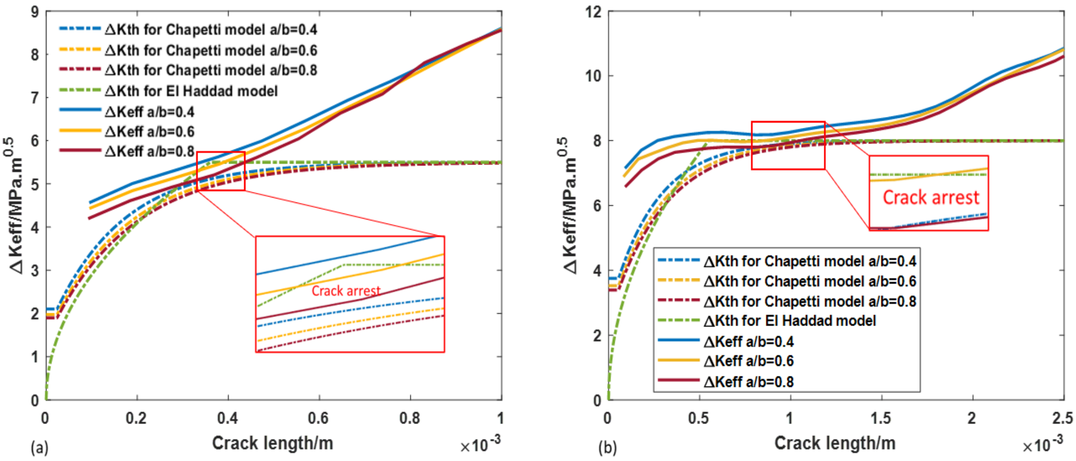

Figure 7.5 Calculated ΔK_{eff} compared with ΔK_{th} with aspect ratios of 0.4, 0.6 and 0.8 a)316Lss b)S355 carbon steel.

It is observed in Figure 7.5 that for each crack configuration, the lines of ΔK_{eff} for different aspect ratios will coincide to a similar line. This is because although the initial aspect ratios and corresponding Y vary, with crack propagation the crack aspect ratio will finally converge. This trend is also seen in Carpinteri's and Caspers's research [124, 163], where the crack aspect ratio converges in the range of 0.6 to 0.7. However, even though the final crack aspect ratios are similar, the initial crack aspect ratios vary, and the difference between these ratios can affect the judgment of crack arrest, especially in short crack region.

Comparing the results shown in Figure 7.5(a), when ΔK_{th} for EI Haddad model is considered, although the applied forces are same, with various initial aspect ratios, the results of crack arrest analysis are different. As for *a/b*= 0.8 and 0.6 (red and yellow lines), the crack is arrested in PSC, but for *a/b*=0.4 (blue line) the crack can continue to propagate to LC and fail. This situation is also present in Figure 7.5(b), where only the initial crack configuration with *a/b*=0.4 can continue to propagate.

The situation of the initial crack with *a/b*=0.4 for specimen B is selected to compare with the results of Figure 7.4 (b) to clarify the influence of the crack aspect ratio on the fatigue limit. The results of ΔK_{eff} and ΔK_{th} with *a/b*=0.4 are shown in Figure 7.6, where based on EI Haddad model, the force leading to the fatigue limit is in the range of 22kN-23kN. According to Figure 7.4 (b), when the force amplitude is between 23kN and 22kN, the crack is also nearly arrested in PSC. So, for the EI Haddad model, the aspect ratio has no significant influence on the crack arrest analysis. However, for the Chapetti model, the results of the calculation with 0.4 aspect ratio are approximately 22kN, which is larger than the result for 0.6 aspect ratio. The reason for the difference in the results of the two models is that in Chapetti model, ΔK_{th} is dependent on the value of Y, but for EI Haddad model, ΔK_{th} is independent on the value of Y, so the fatigue limit is the same. Therefore, when the Chapetti model is selected with a specific aspect ratio of 0.4, the fatigue limit will be underestimated.

For engineering applications, both models can be employed to describe ΔK_{th}, but the initial crack configuration should be considered carefully, as this can affect the calculated fatigue limit. For the two types of double-notched specimens shown in this thesis, the crack configurations with aspect ratios 0.6 and 0.8 may have better agreement on experimental results compared with aspect ratio 0.4.

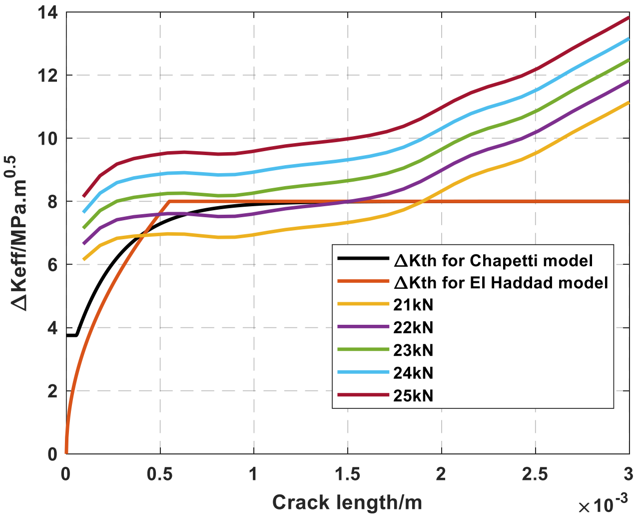

Figure 7.6 Calculated ΔK_{eff} compared with ΔK_{th} of S355 carbon steel (a/b=0.4).

Based on the simulation and experimental results, the following conclusions can be summarized:

- ΔK_{dR} or ΔK_{thR} along cannot represent the entire thresholds, even if the crack size is larger than the MSC ($\Delta K > \Delta K_{dR}$), the crack can still be arrested in PSC region due to the increasing of the threshold. The completed threshold stress range for MSC, PSC and LC must be considered.
- Compressive residual stress can increase the fatigue limit, and the fatigue limit force of notched specimens with induced residual stress can be calculated by the method proposed here by comparing calculated ΔK_{eff} with ΔK_{th}. The numerical results show good agreement with the experimental results. The method can also be easily extended to other notched structures to calculate the fatigue limit for safe design.
- When applying crack growth simulation to calculate ΔK_{eff} or ΔK_{th}, the initiation crack is commonly modelled as semicircular, and it is necessary to consider the influence of aspect ratio of the initial crack configuration. With crack propagation, the aspect ratio can converge, but in the short crack region, the values of ΔK_{eff} with various aspect ratios are different, which can affect determination of the fatigue limit.

7.4 Valve Body Analysis

Sellen et al [157] presented a stress-life design procedure for autofrettage of the complex 3D aluminium AW-6082-T6 valve body shown in Figure 7.7, validated through experimental observation. Their proposed criterion for required autofrettage pressure is *crack arrest* under post-autofrettage working loads. They proposed that a simple, conservative condition for this to occur is the maximum post-autofrettage SIF under working loads is always $K_{max} \leq 0$. From the definition of SIF, this condition is satisfied if the corresponding maximum stress normal to the crack plane is always $\sigma_N \leq 0$.

Sellen et al considered an operational pressure range from zero to 87.5 MPa, and three autofrettage pressures: 180MPa, 270 MPa, and 350MPa. Experimental analysis showed that crack arrest did not occur for 180MPa autofrettage, but the observed irregular crack growth suggested the effective SIF range was close to the threshold value. The 270MPa autofrettage test was stopped after 10^6 cycles, at which very small cracks were observed. A similar observation was made for autofrettage pressure 350MPa.

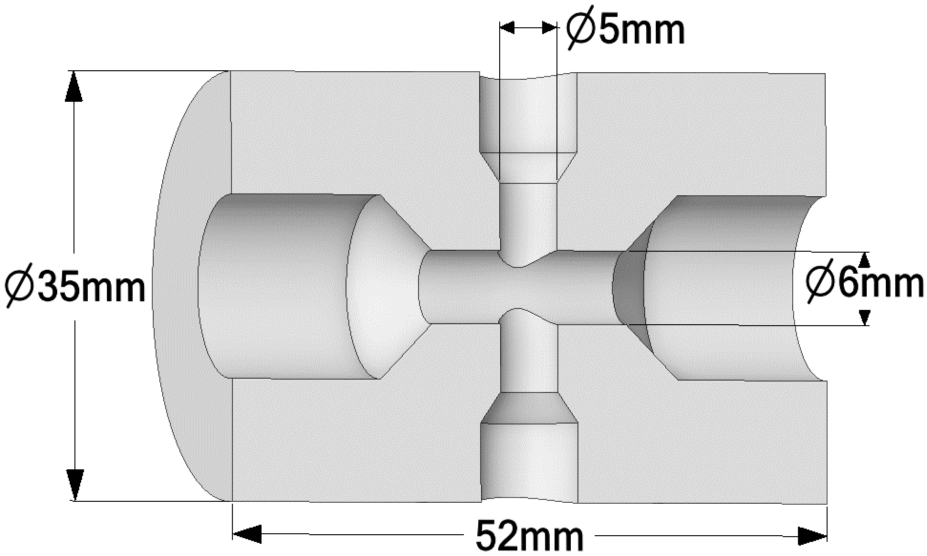

Figure 7.7. Geometry of half of the valve body [157].

Crack arrest in the valve body of [157] is analysed here using the procedure of Figure 4.1. The material properties, material models and boundary conditions used in

FEA are those defined in [157]. Considering the double notch specimen analysis results, the Chapetti model was selected for the assessment of crack arrest.

7.4.1 Material Properties

The material properties used in the FEA and crack propagation threshold model obtained from the literature are given in Table 7.2. Following [157], the valve body material is assumed to be bilinear kinematic hardening material. In constructing the Chapetti model, the value of $\Delta\sigma_{eR}$ was determined from SN curves ΔK_{thR} was obtained from [164, 165] and the value of ΔK_{thR} was obtained from [166, 167] and the average grain size was collected from [168]. The parameters of Chapetti model calculated by (2.41) (2.42), and (2.43) are shown in Table 7.2.

Table 7.2. Collected material properties of AW-6082-T6.

Material	σ_Y (MPa)	E (GPa)	E_T (MPa)	$\Delta\sigma_{eR}\ (R=0)$ (MPa)	ΔK_{thR} $(MPa\sqrt{m})$	d_1 (μm)	ΔK_{dR} $(MPa\sqrt{m})$	k (mm^{-1})
6082-T6	371	76.5	843	150	2.184	32.3	0.982	6.325

The Chapetti fatigue threshold models for AW-6082-T6 based on the material properties of Table 7.2 is shown in Figure 7.8.

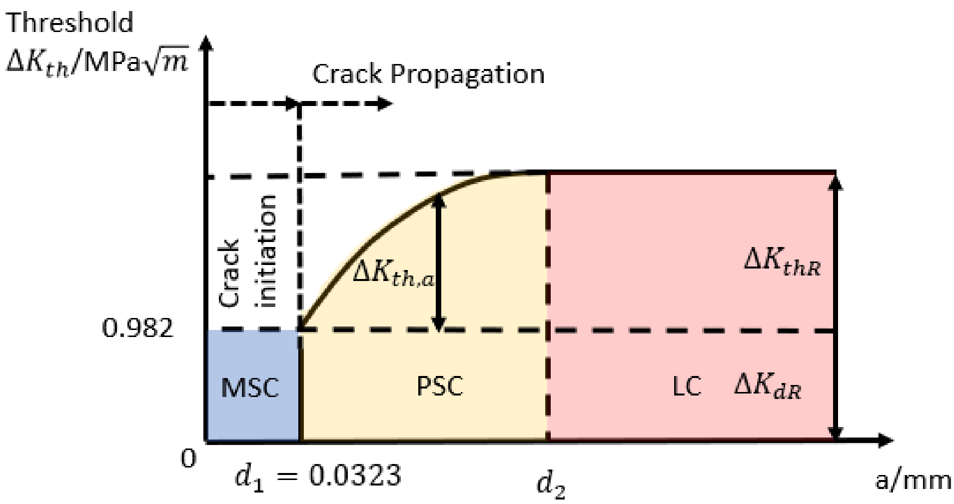

Figure 7.8. Thresholds of aluminium AW-6082-T6 calculated by Chapetti model.

7.4.2 Finite Element Model

The valve body was modelled in ANSYS Workbench using SOLID 187 tetrahedral structural solid elements. The crack-free component has 3 planes of symmetry, and the monotonic and cyclic stress analysis stages of the assessment procedure can be performed for a 1/8 model with appropriate symmetry boundary conditions. However, if crack initiation occurs on a symmetry plane, the material on both sides of the plane must be modelled when applying ANSYS SMART and a 1/4 model is required.

To obtain the location of crack initiation, 1/8 of the valve body was meshed as shown in Figure 7.9a. The applied boundary conditions are shown in Figure 7.9b. Symmetry boundary conditions are applied on the 3 symmetry planes. The real component is sealed by plugs at the end of the conical transition section of the cross-holes. Pressure was applied to the surfaces within the seal, and the pressure force acting on the plugs was represented by axial thrust forces acting on the larger bores.

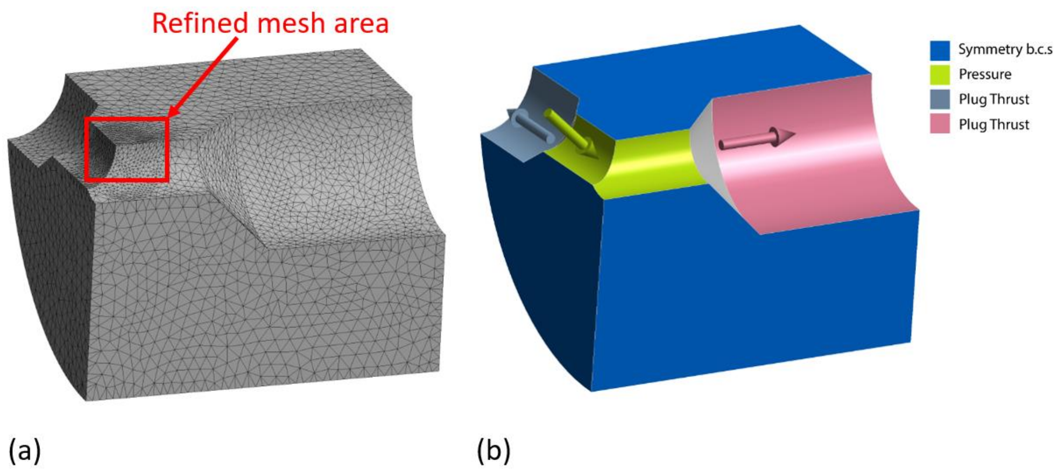

Figure 7.9. a) Finite element mesh and b) Applied boundary conditions for 1/8 valve body model.

Results from cyclic stress analysis shown in Section 7.4.4 indicated that the crack formed on the horizontal symmetry surface of Figure 7.9. A 1/4 model with a similar mesh density was therefore created for crack growth analysis, with boundary conditions shown in Figure 7.10. In addition, the pressures are also applied on the crack flanks.

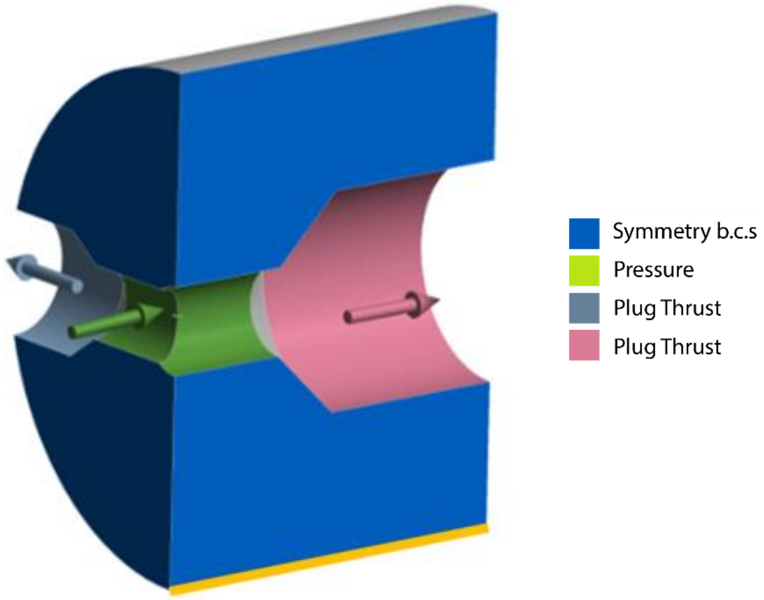

Figure 7.10. Quarter valve structure and applied boundary conditions.

The valve was analysed for an operating pressure cycle from zero to 87.5MPa and five autofrettage pressures: 150MPa, 160MPa, 170MPa, 180MPa, 185MPa and 190MPa.

7.4.3 Preloading and Residual Stress

Elastic-plastic FEA Model 1 was used to calculate the residual stress field induced in the autofrettage process, assuming a bilinear kinematic hardening material model based on material properties of Table 7.2. The distribution of residual stress normal to the symmetry plane for autofrettage pressure 180MPa is shown in Figure 7.11.

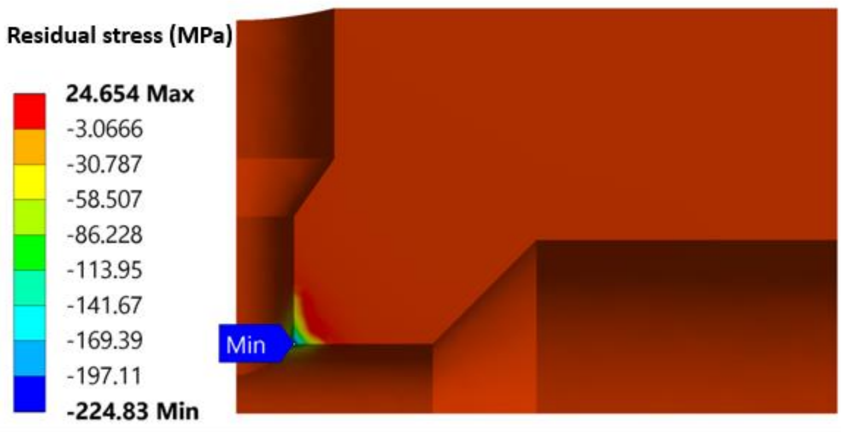

Figure 7.11. Residual stress normal to the symmetry surface at cross-hole intersection after autofrettage.

7.4.4 Crack Initiation

For actual pressure vessels, the fatigue analysis is multiaxial and therefore, multiaxial criteria should be applied to estimate the critical point. As mentioned in Section 2.6, researchers have proposed many improved and innovative multiaxial fatigue failure criteria based on stress and strain by analysing a large set of fatigue data. Among these criteria, the most successful and widely used criteria is based on the critical plane approach [63, 66, 169] where the variable shear stress and strain are considered to be the main cause of fatigue failure and the normal stress in the plane of the shear stress also affects fatigue. According to this theory, Brown [61] proposed that in multiaxial fatigue, cracks are generated in the plane of maximum shear strain and propagate along the direction perpendicular to the normal strain. The fundament of the critical plane approach may be incorporated in the Tresca criterion where the maximum shear stress is also employed as a criterion. The difference is that as a method of fatigue analysis, the core of the critical plane approach is to find the plane with the maximum alternating shear stress or strain.

However, essentially, the maximum shear stress is not one of the stress invariants, but von Mises stress (7.1) is, as the consequence of the variant of shear stress on the orientation, the critical plane approach cannot be applied easily among engineers.

$$\sigma_V = \sqrt{\frac{(\sigma_1 - \sigma_2)^2 + (\sigma_2 - \sigma_3)^2 + (\sigma_3 - \sigma_1)^2}{2}} \tag{7.1}$$

where, σ_V is the von-Mises stress and σ_{1-3} are three principal stresses.

As shown in (7.1), when the von-Mises stress is applied in FEA, the value of stress is always positive, which is contrary to the nature of compressive residual stress: if tensile residual stress is defined as positive, compressive residual stress should be negative. This phenomenon can affect the calculation of mean stress. To solve this issue, the mean stress which is affected by the compressive residual stress can be assumed to be proportional to the hydrostatic pressure, or, as in [108], the sum of the three mean normal stresses. This assumption can be applied accurately in double-notched specimens, but may need further investigation to define the proportional value when applied in complex structures.

7.4.5 Crack Orientation

After determining the critical point, the orientation of the crack must be defined. In the critical plane approach, the crack initiation can be easily determined as the plane with maximum alternating shear stress, and propagate along the direction perpendicular to the normal stress of the plane. However, if the critical point and the fatigue controlling stress components are determined based on von-Mises stress, there is no method to find the orientation of cracks. Here, fracture Mode I, which is the most studied and most common mode in practice, is discussed. In Mode I, normal in-plane loading is employed perpendicular to the crack and therefore, the crack plane can be defined by the normal stress.

Sellen et al. [157] determined the crack plane in a whole structure under unit pressure by the elastic analysis. Then the crack plane orientation can be derived as normal to the first principal stress at this notch [157]. This method can be easily applied, but still has some disadvantages. If the crack grows based on a single static load, the way to determine the orientation of the crack by first principle stress is acceptable, but for fatigue crack growth, the range of stress intensity factor is the main factor to control the crack growth and calculate the fatigue growth life from the Paris law (2.47).

As shown in the Paris law, the first principal stress as a result of unit pressure alone may not represent the range of stress intensity factor. In addition, in some studies based on fracture mechanics, the orientation of the crack is also assumed to be perpendicular to the direction of nominal stress in a flat specimen [170] or the residual hoop stress in a specimen with crossing holes [105]. The assumption of crack initiation should be considered in more detail.

7.4.6 Determination of Crack Initiation by Critical Plane Approach

In stress life fatigue analysis, crack initiation is usually assumed to occur at the location of maximum stress on a free surface [171], referred to as the critical point. The von Mises equivalent stress distribution at the cross-bore intersection for a valve body without autofrettage at maximum operating pressure 87.5 MPa is shown in Figure 7.12(a). The critical point occurs on the surface at the intersection between the cross-holes, where the maximum stress occurs. When compressive residual stress is present, the value and location of the maximum stress can change. This is seen in

Figure 7.12(b), which shows the von Mises equivalent stress distribution at the same pressure for a valve body previously subjected to 180MPa autofrettage pressure. The maximum von Mises stress now occurs internally, close to the cross-hole intersection. However, this does not represent the critical point. As the valve structure experiences 3D stress, the von Mises stress is not suitable for identifying the location of crack initiation and a multiaxial fatigue criterion is required.

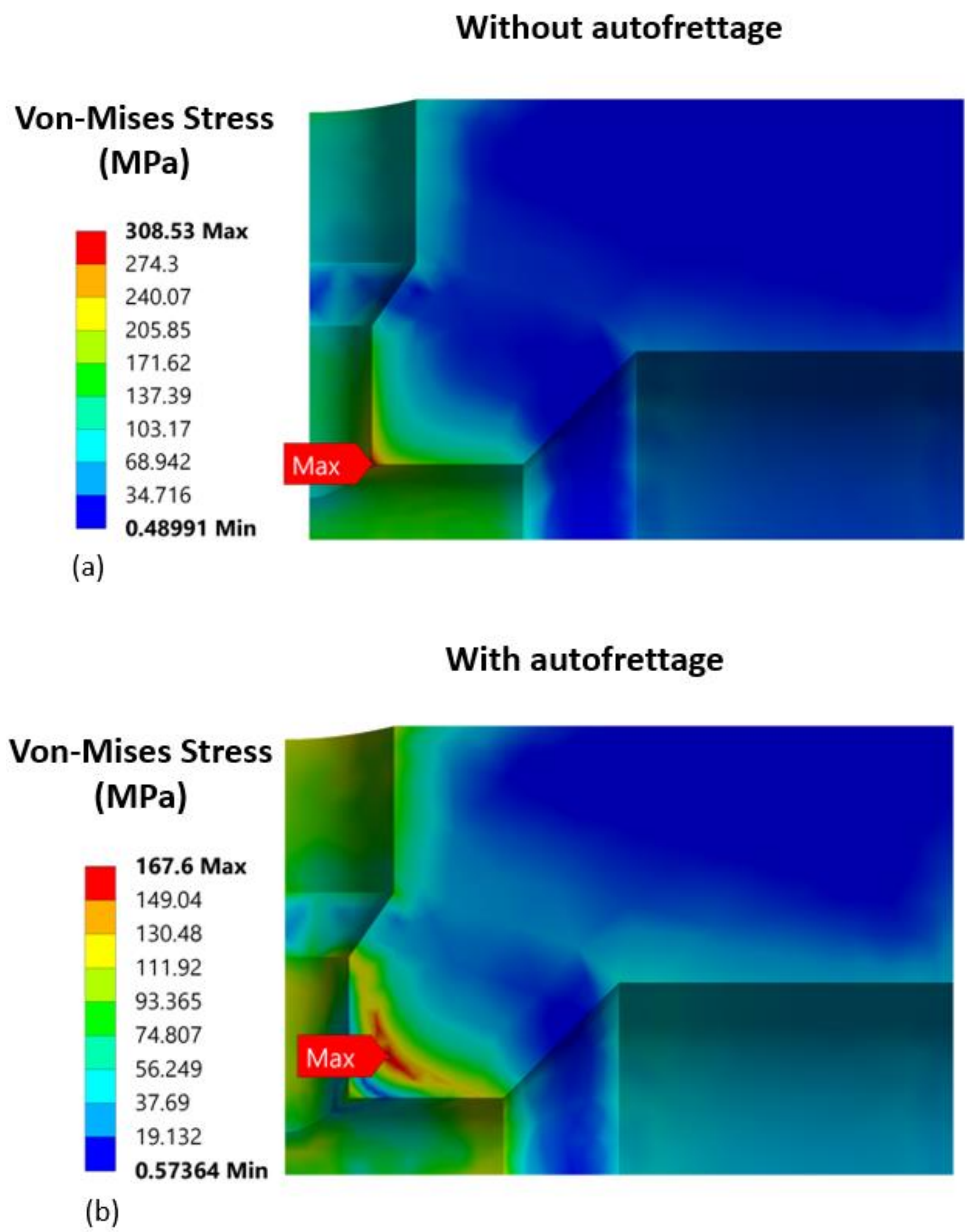

Figure 7.12. Von Mises equivalent stress distribution at maximum operating pressure 87.5 MPa (a) no autofrettage and (b) 270 MPa autofrettage pressure.

Several multiaxial fatigue failure criteria have been proposed, based on both stress and strain. In the critical plane approach [63, 66, 169], fatigue failure is dependent on the maximum shear stress range over the load cycle and the mean stress normal to the shear plane [64]. The location of crack initiation and orientation of the crack plane are determined by considering the stress cycle at specific nodes in the model. Depending on the FEA software used, this may be done for all nodes through post-processor load case calculations, application of internal macros or exporting stress results to an external program for further processing. At each node, the maximum shear stress plane is identified by the maximum shear stress range between the minimum and maximum loads. This may be defined in terms of principal stress if the principal directions do not change over the load range. If the principal directions change over the cycle, the calculation should be based on the stress component range.

The principal stress differences at a node are defined as shown in (2.32). An alternating shear stress range $S_{alt\,ij}$ ($i \neq j = 1,2,3$) is defined for each stress difference, and the maximum alternating stress range at each node determined as (2.33). These equations are also included in the ASME code when the principal stress direction is constant. However, the direction can be changed due to the autofrettage process.

Due to the change in principal stress direction with autofrettage, relying on stress magnitude calculations becomes inadequate. Hence, it's important to incorporate stress transformation calculations to adjust stress components post-autofrettage. The procedures of stress transformation are illustrated in Figure 7.13, where Q is the transform matrix.

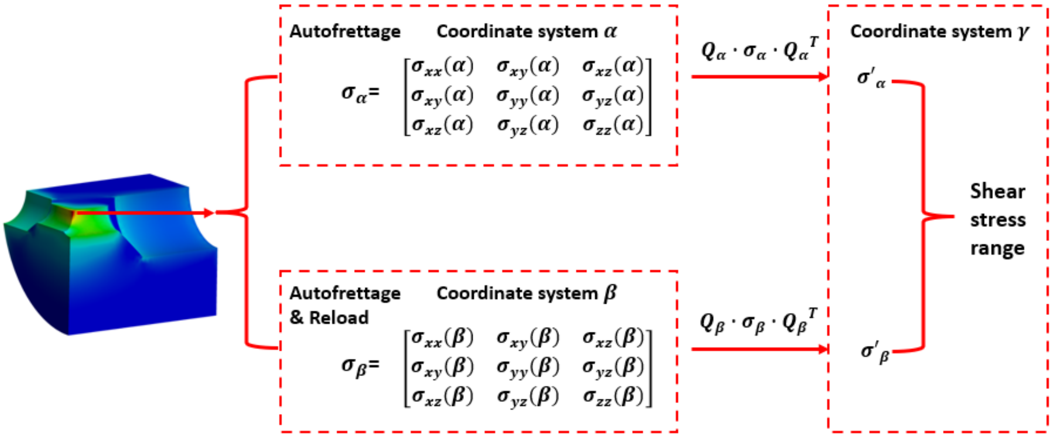

Figure 7.13. Stress transformation to determine the maximum range of normal stress.

1. Export the results of stress components after autofrettage and autofrettage & reload from elastic-plastic FEA.
2. Select another coordinate system γ, do stress transformation to calculate stress components.
3. Calculate the shear stress difference based on the coordinate system γ.
4. Repeat the Step 2 and 3 for all coordinate systems to determine the maximum shear stress range.
5. The plane with the maximum shear stress range can be obtained as the crack plane.

The most difficult procedure above is Step 4: to determine the crack plane by repeated calculation of stress transformation. Therefore, an improved method is proposed here to obtain the plane from the amplitude of stress components.

Assume the coordinate system after stress transformation is known as coordinate system γ and the stress components from the autofrettaged structure and autofrettaged & reloaded structure are based on a global coordinate system. The procedures to calculate the stress range can be simplified as:

$$\Delta\sigma_\gamma' = Q \cdot \sigma_\alpha \cdot Q^T - Q \cdot \sigma'_\alpha \cdot Q^T = Q \cdot \Delta\sigma_\alpha \cdot Q^T \quad (7.2)$$

where, $\Delta\sigma_\gamma'$ is the range of transformed stress, σ_α and σ'_α are stress components from autofrettaged structures and reloaded structures respectively, and $\Delta\sigma_\alpha$ is the range of stress, such that $\Delta\sigma_\alpha = \sigma_\alpha - \sigma'_\alpha$. From (7.2), $\Delta\sigma_\gamma'$ based on arbitrary coordinate systems can be directly obtained from the $\Delta\sigma_\alpha$ if the original coordinate system of σ_α and σ'_α is the same. Additionally, the maximum shear stress range can be directly determined from three principal stresses of $\Delta\sigma_\alpha$, which means the plane with the maximum shear stress range can be determined from $\Delta\sigma_\gamma{}'$, which can also be determined from the $\Delta\sigma_\alpha$. Step 4 can thus be simplified to determine the maximum shear stress from the amplitude of the stress components.

For instance, with 180MPa autofrettage pressure, if the change of coordinate systems of principal stresses is ignored, the ASME code [64] can be directly applied to calculate the shear stress ranges, as shown in Figure 7.14. The maximum shear stress range is thus obtained as 107.34MPa.

Contour plots of the alternating shear stress in the valve body with autofrettage based on the proposed improved method are shown in Figure 7.15. The highest value of 147.9MPa occurs on the surface at the cross-hole intersection, as highlighted in Figure 7.15. This is therefore defined as the crack initiation location. The crack plane is also defined by the principal stress directions, such that the crack surface corresponds to the plane where the alternating shear stress is $S_{alt\,31}$. This is in agreement with experimental findings in [157].

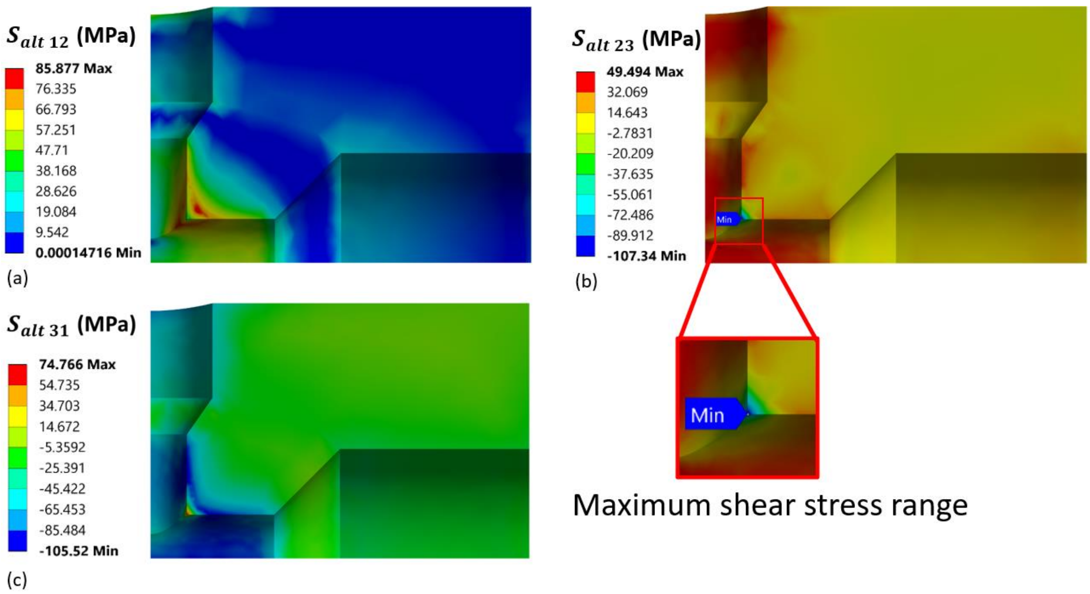

Figure 7.14. Contour plots of alternating stress $S_{alt\,ij}$ MPa with 180MPa autofrettage pressure based on ASME code without considering orientation of principal stresses.

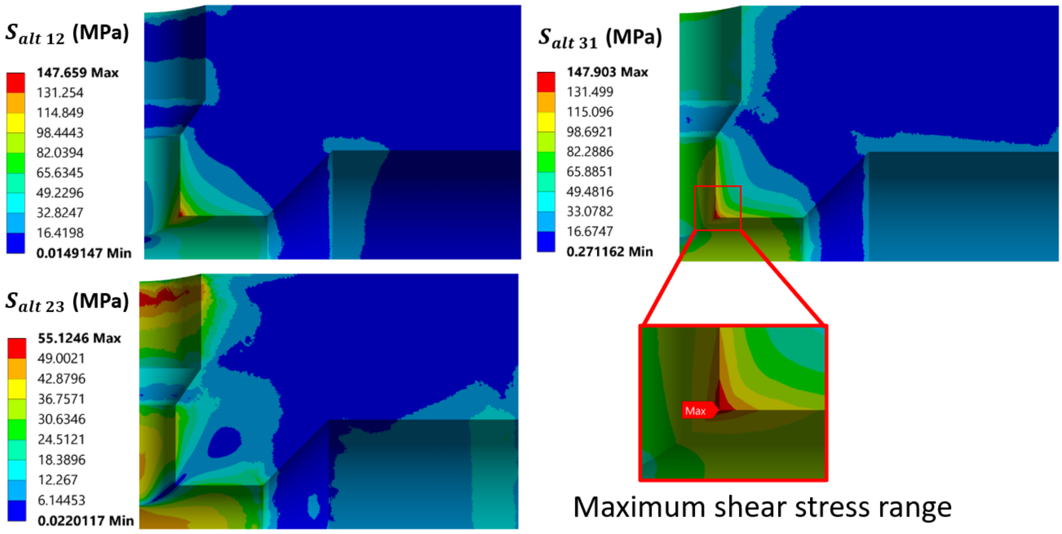

Figure 7.15. Contour plots of alternating stress $S_{alt\ ij}$ MPa with 180MPa autofrettage pressure based on the improved method.

The results of the maximum shear stress range with and without the consideration of the direction of the principal stresses are different, the value of maximum shear stress changes from around 147.9MPa to 107.3MPa when the autofrettage pressure is 180MPa.

The ASME code and improved procedures are also applied to the structure with 270MPa autofrettage pressure. As shown in Figure 7.16, the maximum shear stress range without considering the direction of principal stress is approximately 143.78MPa. Using the proposed method, the maximum shear stress range calculated based on the amplitude stress component is also 147.9MPa for 270MPa autofrettage pressure. To determine which method is more accurate, the theory of superposition is used. Considering the residual stress and subsequent stress induced by applied pressure, the stress amplitude can be calculated as:

$$\sigma_a = \frac{\sigma_{max} - \sigma_{min}}{2} = \frac{\left(\sigma_{app,max} + \sigma_{rs}\right) - \left(\sigma_{app,min} + \sigma_{rs}\right)}{2} = \frac{\Delta\sigma_{app}}{2} \tag{7.3}$$

where, σ_a is the stress amplitude, σ_{max} and σ_{min} are the maximum and minimum stress with induced residual stress, $\sigma_{app,max}$ and $\sigma_{app,min}$ are the maximum and minimum stress as results of applied internal pressure, σ_{rs} is the residual stress and

$\Delta\sigma_{app}$ is the alternating applied stress. Based on the superposition method, the value of σ_a is only dependent on the applied pressure as $\frac{\Delta\sigma_{app}}{2}$, regardless of the value of autofrettage. This theory can be utilized in the calculation of shear stress range. The maximum shear stress range calculated by the proposed method is approximately 147.9MPa, whether the autofrettage pressure is 180MPa or 270MPa. However, if the orientation of principal stress is ignored, based on the ASME Code the maximum shear stress range with 180MPa autofrettage pressure is 107.34MPa and with 270MPa autofrettage pressure, it increases to 143.78MPa. This improvement of the maximum shear stress range is contrary to the theory of superposition. Therefore, the proposed method considering the amplitude of stress components can provide more accurate determination of the shear stress range.

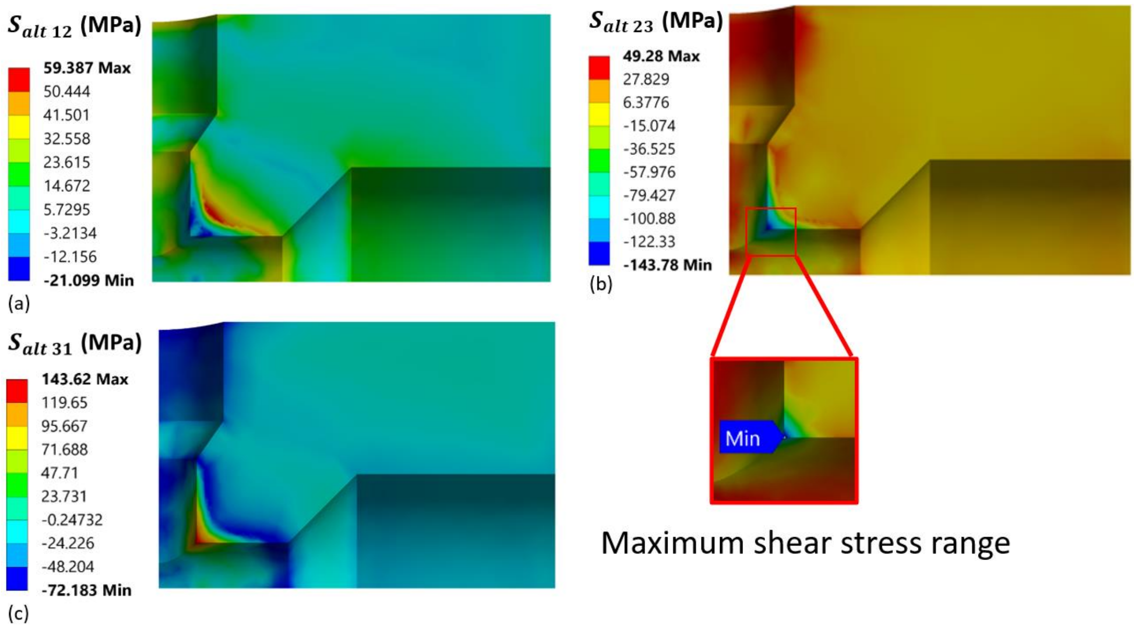

Figure 7.16. Contour plots of alternating stress $S_{alt\ ij}$ MPa with 270MPa autofrettage pressure based on ASME code without considering orientation of principal stresses.

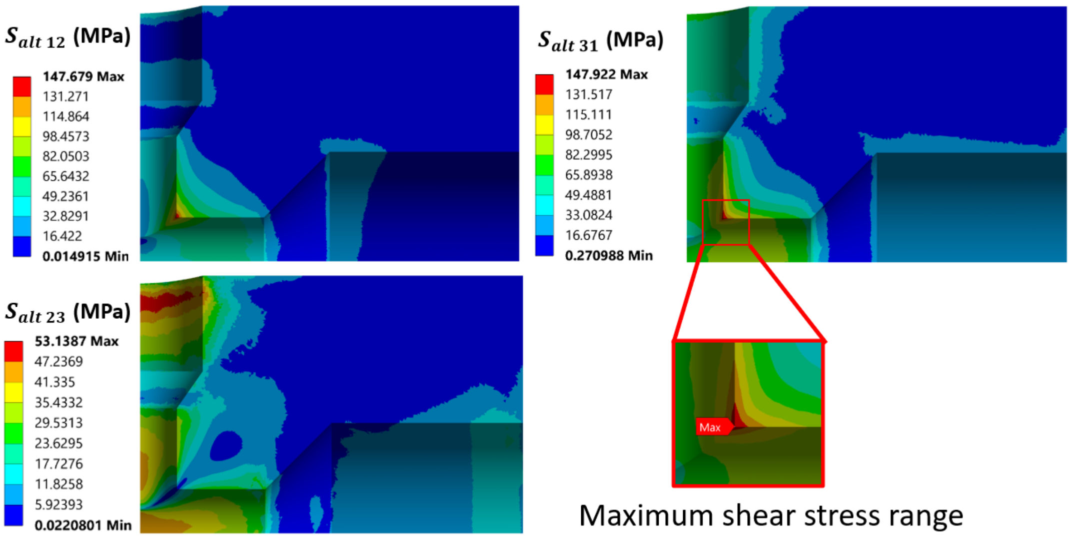

Figure 7.17. Contour plots of alternating stress $S_{alt\,ij}$ MPa with 270MPa autofrettage pressure based on the improved method.

7.4.7 Determination of Crack Initiation by Signed von-Mises Stress

The theory of application of signed von Mises stress to find the critical point is the same as the critical plane approach: to find the largest fatigue controlling stress components on the structure. In general, the stress amplitude as von Mises stress is determined by FEA first and by the mean stress correction methods such as Goodman, Gerber and Soderberg mean stress correction [31], an equivalent stress amplitude is calculated to determine the critical point. In (7.3), the stress amplitude is only dependent on the applied pressure, but the stress ratio used in mean stress correction is dependent on the residual stress as:

$$R = \frac{\sigma_{min}}{\sigma_{max}} = \frac{\sigma_{app,min} + \sigma_{rs}}{\sigma_{app,max} + \sigma_{rs}} \tag{7.4}$$

In FEA, the result of stress amplitude according to (7.3) is shown in Figure 7.18.

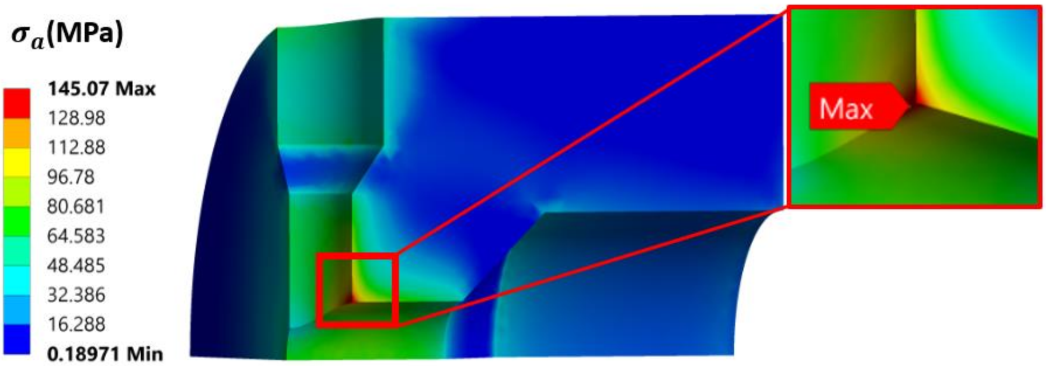

Figure 7.18. The result of stress amplitude with internal pressure.

The positive von Mises stress is widely used to describe the stress distribution of the structure, but the compressive residual stress should be negative by definition. Signed von Mises stress [172] is applied in this section to describe the residual stress and calculate the mean stress. Equation (2.37) is applied with the FKM mean stress correction (2.12) to (2.15) in the following calculations. In addition, according to FKM, for wrought aluminium alloys, $a_M = 0.001$ and $b_M = -0.04$.

According to (2.12) to (2.15), the results of residual stress, mean stress based on signed von Mises stress, and equivalent stress amplitude are shown in Figure 7.19(a), (b) and (c). In Figure 7.19(a), the maximum compressive residual stress is in the notch root and the tensile residual stress surrounds around the notch to balance the stress. In addition, the mean stress also decreases from zero to negative, which is beneficial for fatigue life, as shown in Figure 7.19(b). Finally, based on the calculation of equivalent stress amplitude as shown in Figure 7.19(c), the critical point can be obtained at the notch root, which is the same as determined by alternating maximum shear stress in Section 7.4.5. Therefore, combining these two results, the assumption of the crack initiation on the notch root is acceptable, and compared with the method based on elastic analysis only, the method proposed here is more rigorous where plasticity, shear stress, and signed von Mises stress with mean stress correction are all included.

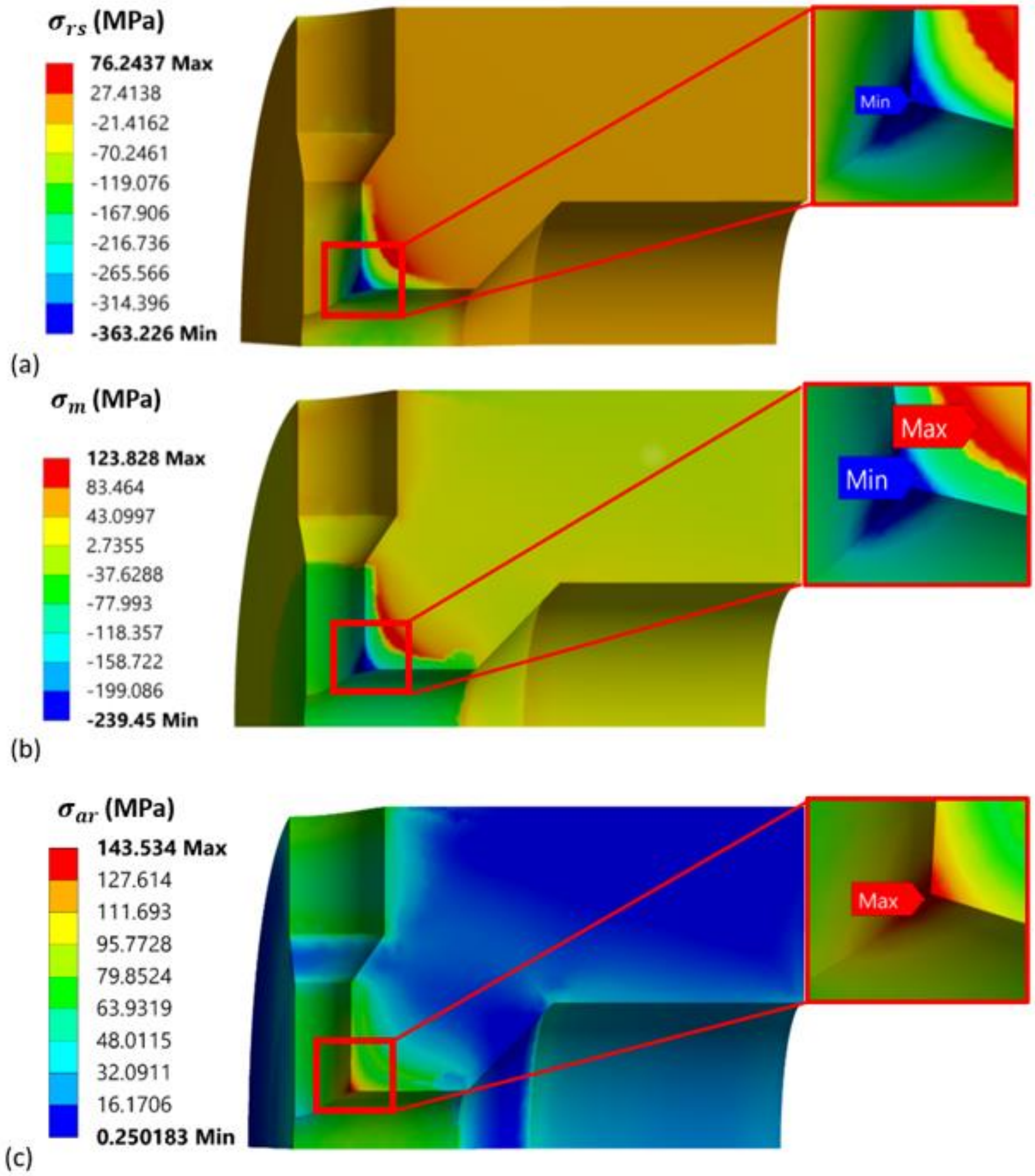

Figure 7.19. The results of (a) σ_{rs} (b) σ_m (c) σ_{ar}.

7.4.8 Determination of Orientation of Crack Plane

In [157], the orientation of the crack was obtained from the direction of the first principal stress of under unit pressure. However, in fatigue fracture, crack growth is determined by the range of stress intensity factor, so a method is proposed to determine the orientation of crack plane from the maximum range of normal stress. Similarly, the maximum range of normal stress can be determined directly from the first principal stress of the stress range $\sigma_{1,\Delta\sigma}$. This can save computational time in FEA. The result of the first principal stress of $\Delta\sigma$ is shown in Figure 7.20, where the direction of the $\sigma_{1,\Delta\sigma}$ is normal to the diagonal plane. Therefore, the crack orientation can be assumed normal to the $\sigma_{1,\Delta\sigma}$.

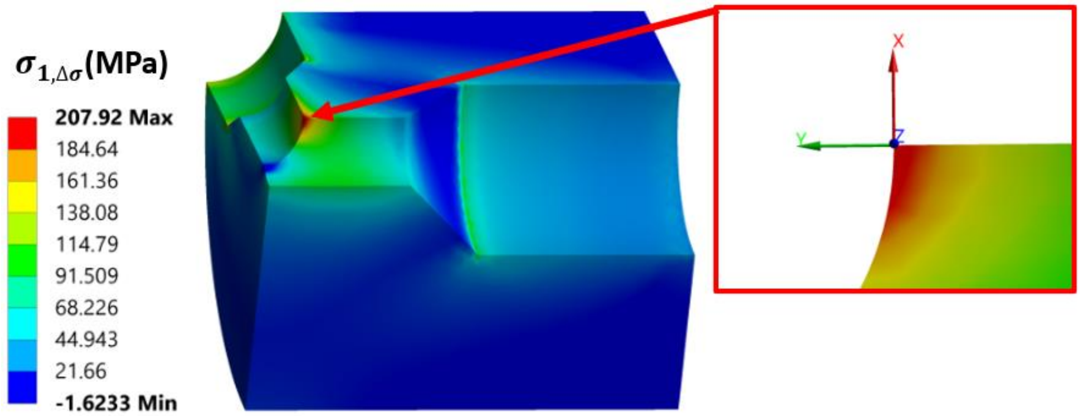

Figure 7.20. The results of $\sigma_{1,\Delta\sigma}$, x direction.

7.4.9 Crack Growth Simulation

An initial semi elliptical crack with an aspect ratio of 0.6 [124, 125] was inserted in the model of Figure 7.10 at the identified crack initiation site, as shown in Figure 7.21. The crack plane lies on the triad X-Z plane. Crack propagation analysis was performed using the ANSYS SMART crack growth tool.

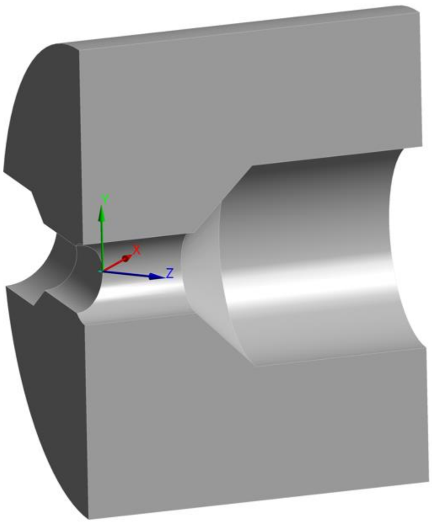

Figure 7.21. Location of crack initiation and crack plane orientation.

Crack growth analysis was performed for six models under cyclic working pressure range of zero to 87.5MPa ($R = 0$), one with no residual stress and others with initial residual stress corresponding to autofrettage pressures of 150MPa, 160MPa, 170MPa, 180MPa, 185MPa and 190MPa imported from elastic-plastic analysis. The calculated variation in K_{max} with increasing crack length for each model is shown in Figure 7.22, where the final crack profile illustration represents the termination of the simulation.

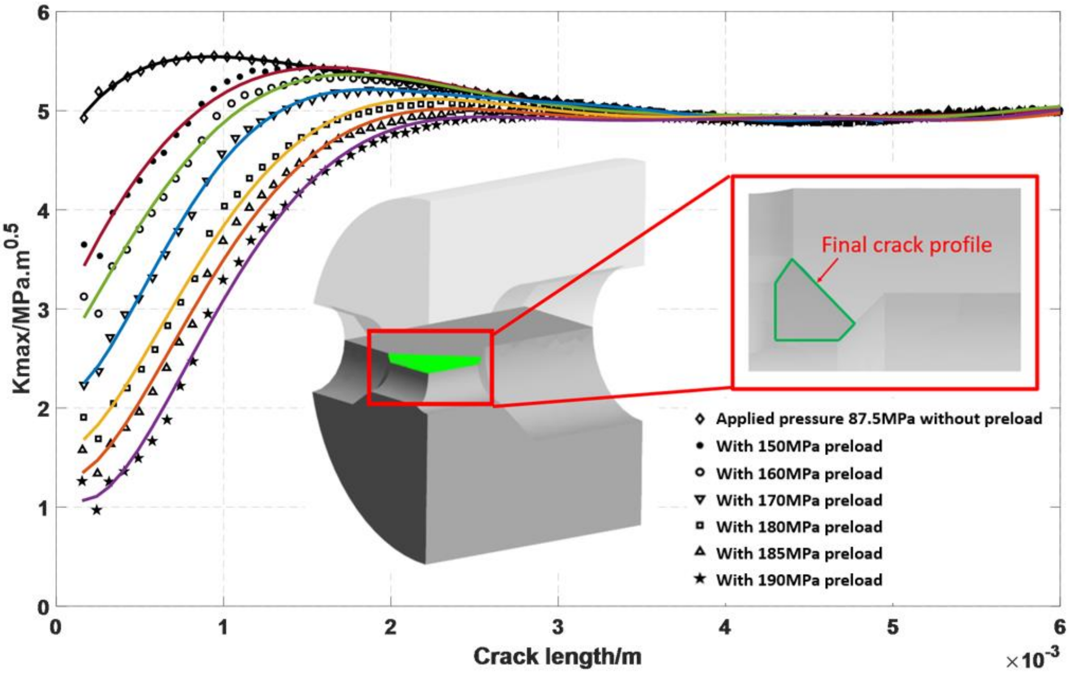

Figure 7.22. Variation in K_{max} with crack length under working pressure for six autofrettage conditions.

Figure 7.22 shows that at shorter crack lengths, within the compressive residual stress region, K_{max} decreases significantly with increasing autofrettage pressure. As the crack propagates through the residual stress region, K_{max} approaches a similar value for all the autofrettage conditions considered and beyond the compressive stress zone, after around 3mm, there is little difference in the curves. A similar response is found for the variation in K_{min} with crack length, as shown in Figure 7.23. Within the residual stress region, K_{min} decreases significantly with increasing autofrettage pressure but the curves approach a similar value as the crack grows beyond this.

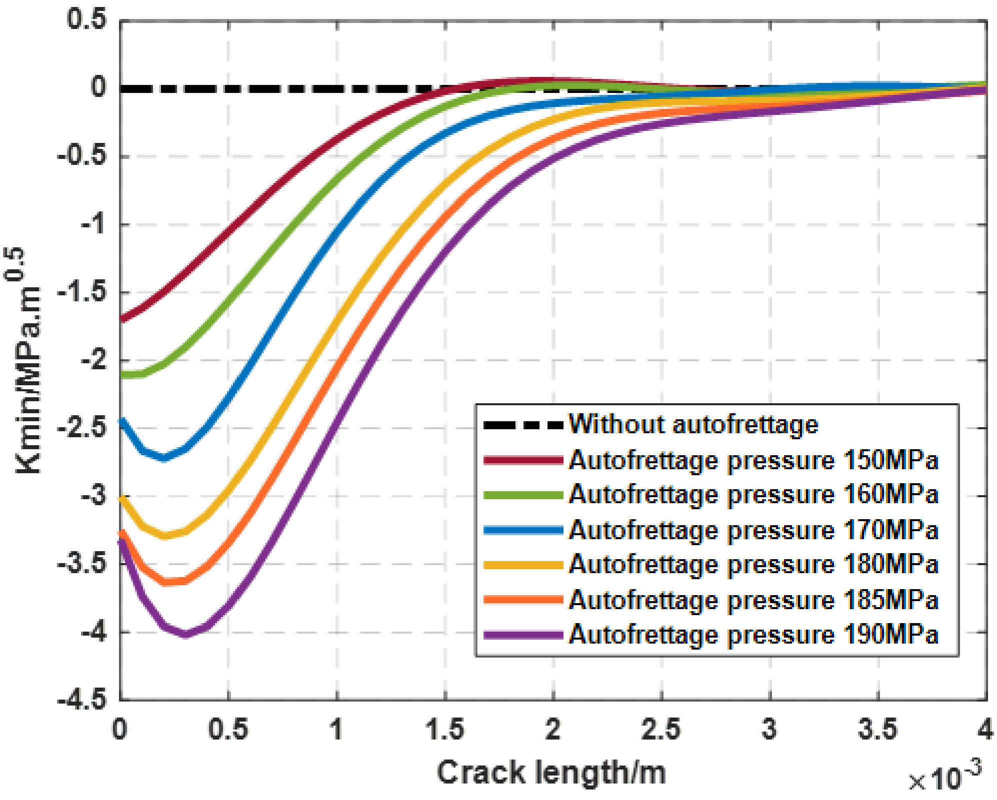

Figure 7.23. Variation in K_{rs} with crack length after autofrettage, with the residual stress normal to the crack plane inset.

7.4.10 Crack Arrest Assessment

The values of ΔK_{eff} with different autofrettage pressures calculated by (4.15) are compared with the Chapetti threshold SIF range ΔK_{th} in Figure 7.24. As the autofrettage pressure increases from 150MPa to 180MPa, the ΔK_{eff} curves approach the threshold curve, but crack arrest is not predicted. Crack arrest did not occur for autofrettage pressure 180MPa in the experimental investigation of [157] but, the 180MPa autofrettage pressure can increase the fatigue life significantly from 150000 cycles to 368000 cycles and based on the form of notch cracks observed in the failed test piece, it was presumed that the effective SIF range was close to the threshold value. This presumption was investigated here by considering the slightly higher autofrettage pressure of 185MPa. Figure 7.24 shows the ΔK_{eff} curve for 185MPa crosses the Chapetti crack propagation threshold boundary, indicating crack arrest in the PSC region.

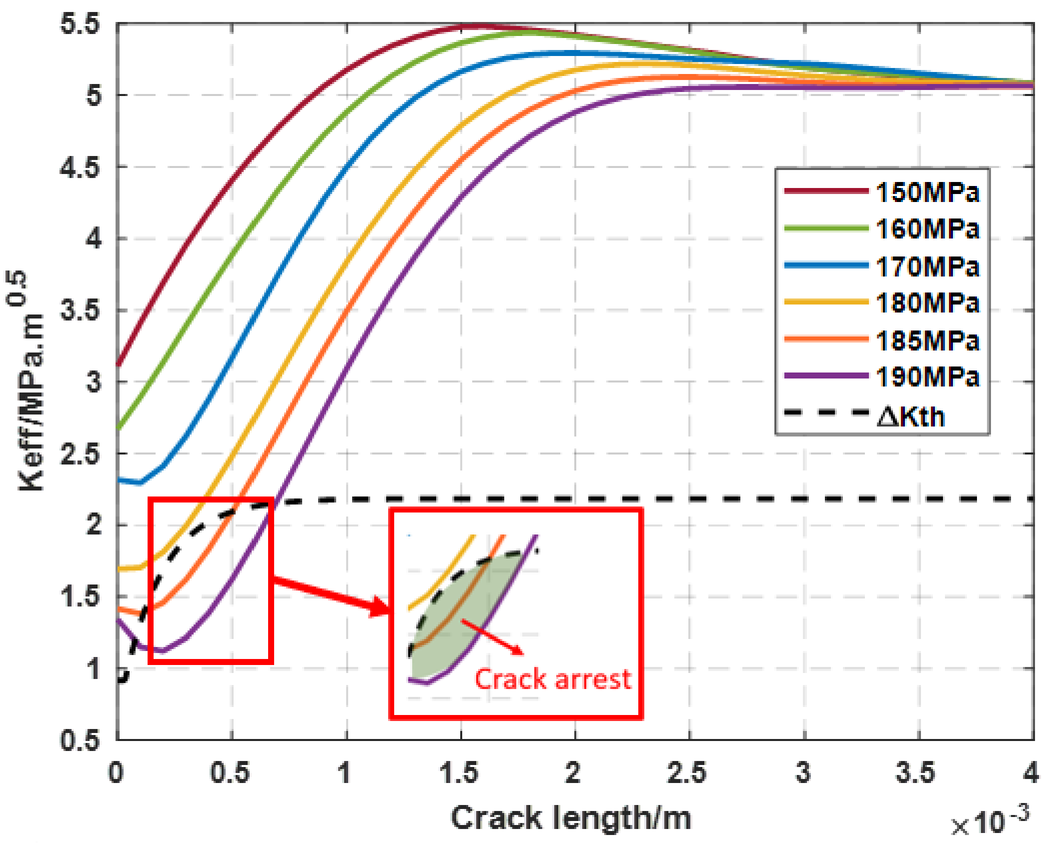

Figure 7.24. Comparison of ΔK_{eff} with ΔK_{th}.

7.4.11 Discussion

The method was applied to two types of preloaded double notch specimens, one stainless steel and the other low carbon steel, and a 3D aluminium alloy valve body design. Comparison with experimental fatigue life data for preloaded double notch specimens showed that the El Haddad model did not result in a conservative estimate of the required preload. The Chapetti model satisfied the necessary condition for crack arrest based on finite run-out data, but this data alone is not sufficient to state crack arrest occurred. A more detailed experimental investigation measuring crack propagation in the compressive residual stress region is required to fully establish the conditions for crack arrest. Experimental investigation of the 3D valve [157] showed that crack arrest did not occur for the minimum autofrettage pressure of 180MPa considered, but presumed that the effective SIF range was close to the threshold value. Application of the proposed method showed no crack arrest at autofrettage pressure of 180MPa, but that crack arrest did occur at the slightly higher pressure of

185MPa, supporting the presumption stated in [157]. Further experimental investigation is required to establish the actual minimum autofrettage pressure required to cause crack arrest in the valve body under the given working cycle, which was shown to occur for the significantly higher autofrettage pressures of 270MPa and 350MPa in [157].

The comparison with available experimental data shows that the proposed methodology is a promising tool for defining the minimum autofrettage pressure required for crack arrest and hence infinite fatigue life. The method can also be used to determine the required autofrettage pressure for a specific finite fatigue life, following the procedure of [132]. The SMART crack growth tool is based on LEFM, where the small-scale yield assumption applies. Future work should investigate the effect of more extensive plastic deformation, with a possible extension of the method by incorporating J-integral correction of the SIF, and the influence of initial crack aspect ratio on crack propagation modelling.

Chapter 8 Conclusion

The proposed method aims to enhance high cycle fatigue stress-life assessment of components with induced residual stress through the application of a fracture mechanics crack growth model and a derived stress-crack initiation life curve. The crack initiation length is assumed dependent on the average grain size of the material and based on the assumed crack initiation length, the number of cycles to crack initiation, N_i, is determined from a S-N_i curve obtained from standard S-N data and application of the ASNSYS SMART crack propagation tool.

The S-N_i curve can be used to determine the crack initiation life of cyclically loaded components with both notch and residual stress effects. The crack propagation life of the component is evaluated by FEA, using the ANSYS Workbench SMART tool. In components with residual stress, the variation of stress intensity factor with increasing crack length is obtained in the form of polynomial equations and the crack propagation life is obtained by superposition of the applied load stress distribution and residual stress distribution. The SMART crack growth tool is currently limited to linear elastic FEA, and the residual stress field resulting from preloading must be imported as an initial state of stress.

Physical testing of double-notch 316L stainless steel and S355 carbon steel specimens showed the expected enhanced fatigue life in specimens with induced residual stress. Application of the proposed method to the analysis of specimens both with and without induced residual stress gave an improved estimation of fatigue life compared to the standard stress life approach. Subsequently, the same proposed method is also employed to the fatigue life prediction of cross-bore blocks made by 4340 steel shown in Section 6.1, the numerical results also have good agreement with the experimental results.

To validate the method, a practical structure made of different materials was considered, hence the 42CrMo4 injection system component considered in Section 6.2. The same analysis procedures are applied to the component but, different to the structure response of the double-notched specimens, plastic shakedown was investigated to occur for several working pressures. To evaluate the structure response, the post-autofrettage equivalent plastic strain is checked over a number of working cycles. If the plastic shakedown response occurs, the redistribution of residual stress is considered and the redistributed residual stress is exported to the following fracture simulation.

Compared with the research in double-notched specimens, the results of injection system components are considered, including the redistribution of the residual stress. The proposed method can also provide good agreement. By investigation, the proposed method demonstrates good performance when the structure response is characterized by elastic shakedown. When the structure response shifts to plastic shakedown, plasticity effect is required to be accounted for in the FEA, in the proposed method, the small scale yield assumption is checked firstly by the calculation of the minimum crack initiation length and the plasticity effect is considered by multistep analysis. Considering plasticity effect, the proposed method provides less deviation compared to LEFM.

Another new methodology for determining the autofrettage pressure required to achieve crack arrest and hence infinite fatigue life in pressure components subject to varying loads was proposed. In this method, the residual stress distribution due to autofrettage is also obtained by elastic-plastic analysis and exported as an initial stress state to a crack propagation model and the ANSYS SMART crack growth tool is applied to simulate crack propagation. The location of crack initiation and fracture plane orientation are determined based on the maximum shear stress amplitude which is determined by the improved method mentioned in Section 7.4.6. The condition for crack arrest is determined by comparing the effective SIF of the growing crack with a crack propagation threshold model for MSC, PSC and LC. The crack threshold models of El Haddad and Chapetti were considered. For the valve body structure considering in the Section 7.4, the proposed method can have better agreement with the experimental results when the Chapetti model is selected to obtain thresholds and through the proposed method based on the crack arrest analysis the minimum autofrettage pressure can be determined.

Although the framework of the proposed method is created and successfully applied in several components, but future work is recommended as:

1. Plasticity correction can be considered more accurate even though the small scale assumption is already satisfied.
2. During the simulation of crack propagation, numerical results are sensitive when the crack length is very short (around 0.5 mm). Currently, this sensitivity is managed by refining the mesh around the crack tips. However, this refined mesh increases computational time. Therefore, a more effective method is needed to balance mesh refinement and computational efficiency.
3. To validate the accuracy of the proposed method, it is necessary to test more practical components made from a variety of materials. While the current focus is primarily on steels, it is important to include other common industrial materials such as cast iron, aluminium, and titanium.

Reference

1. Maschinenbau, F. and E. Haibach, *Analytical strength assessment of components in mechanical engineering*. 2003: VDMA-Verlag.
2. Boiler, A., *Pressure Vessel Code Division 3.* Alternative Rules for High Pressure Vessels, 1998.
3. Deardorff, A.F. and J.K. Smith, *Evaluation of conservatisms and environmental effects in ASME code, section III, class 1 fatigue analysis*. 1994, Sandia National Lab.(SNL-NM), Albuquerque, NM (United States); Structural ….
4. De los Rios, E., et al., *Fatigue crack initiation and propagation on shot-peened surfaces in A316 stainless steel.* International Journal of Fatigue, 1995. **17**(7): p. 493-499.
5. Chahardehi, A., F.P. Brennan, and A. Steuwer, *The effect of residual stresses arising from laser shock peening on fatigue crack growth.* Engineering Fracture Mechanics, 2010. **77**(11): p. 2033-2039.
6. Zhang, X., et al., *Improvement of fatigue life of Ti–6Al–4V alloy by laser shock peening.* Materials Science and Engineering: A, 2010. **527**(15): p. 3411-3415.
7. Gujba, A.K. and M. Medraj, *Laser peening process and its impact on materials properties in comparison with shot peening and ultrasonic impact peening.* Materials, 2014. **7**(12): p. 7925-7974.
8. Zhuang, W. and B. Wicks, *Multipass low-plasticity burnishing induced residual stresses: three-dimensional elastic-plastic finite element modelling.* Proceedings of the Institution of Mechanical Engineers, Part C: Journal of Mechanical Engineering Science, 2004. **218**(6): p. 663-668.
9. Hua, Y., et al., *Surface modification through combination of finish turning with low plasticity burnishing and its effect on fatigue performance for Inconel 718.* Surface and Coatings Technology, 2019. **375**: p. 508-517.
10. Parker, A., G. O'Hara, and J. Underwood, *Hydraulic versus swage autofrettage and implications of the Bauschinger effect.* J. Pressure Vessel Technol., 2003. **125**(3): p. 309-314.
11. Aziz, F., S. Kamal, and U. Dixit, *Enhancing Fatigue Life of Thick-Walled Cylinders through a Hybrid Rotational-Swage Autofrettage-Induced Residual Stresses.* Journal of Materials Engineering and Performance, 2024: p. 1-18.
12. Shim, W., et al., *A study on hydraulic autofrettage of thick-walled cylinders incorporating Bauschinger effect.* Experimental Mechanics, 2010. **50**: p. 621-626.
13. Kamal, S. and U. Dixit, *A comparative study of thermal and hydraulic autofrettage.* Journal of Mechanical Science and Technology, 2016. **30**: p. 2483-2496.

14. Shufen, R. and U.S. Dixit, *A review of theoretical and experimental research on various autofrettage processes.* Journal of Pressure Vessel Technology, 2018. **140**(5): p. 050802.

15. Alegre, J., P. Bravo, and M. Preciado, *Fatigue behaviour of an autofrettaged high-pressure vessel for the food industry.* Engineering Failure Analysis, 2007. **14**(2): p. 396-407.

16. Mughrabi, H., B. Donth, and G. Vetter, *Low‐temperature autofrettage: an improved technique to enhance the fatigue resistance of thick‐walled tubes against pulsating internal pressure.* Fatigue & Fracture of Engineering Materials & Structures, 1997. **20**(4): p. 595-604.

17. Rees, D., *A bounding method for predicting the fatigue life of plain and autofrettaged thick-walled cylinders.* International journal of fatigue, 1991. **13**(1): p. 59-67.

18. Parker, A. and J. Underwood, *Stress intensity, stress concentration, and fatigue crack growth along evacuator holes of pressurized, autofrettaged tubes.* 1996.

19. Badr, E.A., J.R. Sorem Jr, and S.M. Tipton, *Evaluation of the autofrettage effect on fatigue lives of steel blocks with crossbores using a statistical and a strain-based method.* Journal of testing and evaluation, 2000. **28**(3): p. 181-188.

20. Lee, S.-I. and S.-K. Koh, *Residual stress effects on the fatigue life of an externally grooved thick-walled pressure vessel.* International journal of pressure vessels and piping, 2002. **79**(2): p. 119-126.

21. Po¨lzl, M. and J. Schedelmaier. *Fatigue Strength Curves of Thick Walled Tubes Under Consideration of Autofrettage*. in *ASME Pressure Vessels and Piping Conference*. 2003.

22. Thumser, R., et al., *Variable amplitude fatigue of autofrettaged diesel injection parts.* Materialwissenschaft und Werkstofftechnik: Entwicklung, Fertigung, Prüfung, Eigenschaften und Anwendungen technischer Werkstoffe, 2008. **39**(10): p. 719-725.

23. Sellen, S., et al., *Improved design of threaded connections by autofrettage in aluminium compounds for cyclic high pressure loading: design calculations and experimental verification.* Fatigue & Fracture of Engineering Materials & Structures, 2015. **38**(6): p. 714-729.

24. Urade, S.D., D. Bhope, and S. Khamankar, *Stress analysis of multilayer pressure vessel.* Int. J. Eng. Tech. Res, 2014. **2**(9): p. 34-43.

25. Livieri, P. and P. Lazzarin, *Autofrettaged cylindrical vessels and Bauschinger effect: an analytical frame for evaluating residual stress distributions.* J. Pressure Vessel Technol., 2002. **124**(1): p. 38-46.

26. Kamal, S., *Analysis of residual stress in the rotational autofrettage of thick-walled disks.* Journal of Pressure Vessel Technology, 2018. **140**(6): p. 061402.

27. Furuya, Y. and E. Takeuchi, *Gigacycle fatigue properties of Ti–6Al–4V alloy under tensile mean stress.* Materials Science and Engineering: A, 2014. **598**: p. 135-140.

28. Hensel, J., T. Nitschke-Pagel, and K. Dilger, *Effects of residual stresses and compressive mean stresses on the fatigue strength of longitudinal fillet-welded gussets.* Welding in the World, 2016. **60**: p. 267-281.

29. Toparli, M., A. Özel, and T. Aksoy, *Effect of the residual stresses on the fatigue crack growth behavior at fastener holes.* Materials Science and Engineering: A, 1997. **225**(1-2): p. 196-203.

30. Carpinteri, A., R. Brighenti, and S. Vantadori, *Influence of the cold-drawing process on fatigue crack growth of a V-notched round bar.* International journal of fatigue, 2010. **32**(7): p. 1136-1145.

31. Badr, E.A. and J. Ishak, *High-cycle fatigue behavior of type 4340 steel pressurized blocks including mean stress effect.* International Journal of Pressure Vessels and Piping, 2021. **194**: p. 104535.

32. Ince, A., *A mean stress correction model for tensile and compressive mean stress fatigue loadings.* Fatigue & Fracture of Engineering Materials & Structures, 2017. **40**(6): p. 939-948.

33. Dowling, N., C. Calhoun, and A. Arcari, *Mean stress effects in stress‐life fatigue and the Walker equation.* Fatigue & Fracture of Engineering Materials & Structures, 2009. **32**(3): p. 163-179.

34. McKelvey, S.A., Y.-L. Lee, and M.E. Barkey, *Stress-based uniaxial fatigue analysis using methods described in FKM-guideline.* Journal of failure analysis and prevention, 2012. **12**: p. 445-484.

35. Goldak, J., A. Chakravarti, and M. Bibby, *A new finite element model for welding heat sources.* Metallurgical transactions B, 1984. **15**: p. 299-305.

36. Venkatkumar, D. and D. Ravindran, *Effect of boundary conditions on residual stresses and distortion in 316 stainless steel butt welded plate.* High Temperature Materials and Processes, 2019. **38**(2019): p. 827-836.

37. Jiang, W., et al., *Fatigue life prediction of 316L stainless steel weld joint including the role of residual stress and its evolution: Experimental and modelling.* International Journal of Fatigue, 2021. **143**: p. 105997.

38. Guo, Y., et al., *Study on residual stress distribution of 2024-T3 and 7075-T6 aluminum dissimilar friction stir welded joints.* Engineering Failure Analysis, 2020. **118**: p. 104911.

39. Barsoum, Z. and I. Barsoum, *Residual stress effects on fatigue life of welded structures using LEFM.* Engineering failure analysis, 2009. **16**(1): p. 449-467.

40. Maddox, S., *Fatigue design rules for welded structures*, in *Fracture and fatigue of welded joints and structures*. 2011, Elsevier. p. 168-207.

41. Zaroog, O.S., et al., *Modelling of residual stress relaxation: a review.* J Sci Technol, 2009. **17**: p. 211-8.

42. Farajian, M., T. Nitschke-Pagel, and K. Dilger, *Mechanisms of residual stress relaxation and redistribution in welded high-strength steel specimens under mechanical loading.* Welding in the World, 2010. **54**: p. R366-R374.

43. Lee, Y.-B., et al., *Effects of redistributing residual stress on the fatigue behavior of SS330 weldment.* International Journal of Fatigue, 1998. **20**(8): p. 565-573.

44. Shahani, A.R., I. Shakeri, and C.D. Rans, *Effect of residual stress redistribution and weld reinforcement geometry on fatigue crack growth of butt welded joints.* International Journal of Fatigue, 2020. **139**: p. 105780.

45. Murakawa, H., *Residual stress and distortion in laser welding*, in *Handbook of laser welding technologies*. 2013, Elsevier. p. 374-400e.

46. Glinka, G. and A. Newport, *Universal features of elastic notch-tip stress fields.* International Journal of Fatigue, 1987. **9**(3): p. 143-150.

47. Shin, C., K. Man, and C. Wang, *A practical method to estimate the stress concentration of notches.* International Journal of Fatigue, 1994. **16**(4): p. 242-256.

48. Poutiainen, I., P. Tanskanen, and G. Marquis, *Finite element methods for structural hot spot stress determination—a comparison of procedures.* International journal of fatigue, 2004. **26**(11): p. 1147-1157.

49. Neuber, H., *Theory of notch stresses: principles for exact calculation of strength with reference to structural form and material*. Vol. 4547. 1961: USAEC Office of Technical Information.

50. Peterson, R. and R. Plunkett, *Stress concentration factors.* Journal of applied mechanics, 1975. **42**(1): p. 248.

51. SANDEROW, H.I., *THE SUPPORT EFFECT AND ITS IMPACT ON THE DESIGN OF COMPLEX-SHAPED SINTERED PM PARTS.* International Journal of Powder Metallurgy, 2019. **55**(4).

52. Filippini, M., *Stress gradient calculations at notches.* International Journal of Fatigue, 2000. **22**(5): p. 397-409.

53. Taylor, D., *The theory of critical distances.* Engineering Fracture Mechanics, 2008. **75**(7): p. 1696-1705.

54. Susmel, L. and D. Taylor, *A critical distance/plane method to estimate finite life of notched components under variable amplitude uniaxial/multiaxial fatigue loading.* International Journal of Fatigue, 2012. **38**: p. 7-24.

55. Manson, S., *Fatigue behavior in strain cycling in the low and inter. Cycle Range. Fatigue-An Interdisciplinary Approach*. 1969, Syracuse University Press.

56. Dowling, N.E., K.S. Prasad, and R. Narayanasamy, *Mechanical Behavior of Materials: Engineering Methods for Deformation, Fracture, and Fatigue*. 2013: Pearson.

57. Wang, Y.-Y. and W.-X. Yao, *Evaluation and comparison of several multiaxial fatigue criteria.* International Journal of Fatigue, 2004. **26**(1): p. 17-25.

58. Findley, W.N., *A theory for the effect of mean stress on fatigue of metals under combined torsion and axial load or bending.* Journal of Engineering for Industry, 1959. **81**(4): p. 301-305.

59. FA, B.M.K. and K. Miller, *Biaxial low cycle fatigue of 316 stainless steel at elevated tempertaures.* Metals Soc., London, 1982.

60. McDiarmid, D., *A general criterion for high cycle multiaxial fatigue failure.* Fatigue & Fracture of Engineering Materials & Structures, 1991. **14**(4): p. 429-453.

61. Brown, M.W. and K. Miller, *A theory for fatigue failure under multiaxial stress-strain conditions.* Proceedings of the Institution of Mechanical engineers, 1973. **187**(1): p. 745-755.

62. Susmel, L., R. Tovo, and P. Lazzarin, *The mean stress effect on the high-cycle fatigue strength from a multiaxial fatigue point of view.* International Journal of Fatigue, 2005. **27**(8): p. 928-943.

63. Wang, C. and M. Brown, *On plastic deformation and fatigue under multiaxial loading.* Nuclear engineering and design, 1996. **162**(1): p. 75-84.

64. Engineers, T.A.S.o.M., *ASME Boiler and Pressure Vessel Code Division 3,* in *Alternative Rules for High Pressure Vessels*. 2015: New York.

65. Papadopoulos, I.V., *Critical plane approaches in high‐cycle fatigue: on the definition of the amplitude and mean value of the shear stress acting on the critical plane.* Fatigue & Fracture of Engineering Materials & Structures, 1998. **21**(3): p. 269-285.

66. Gao, D., et al., *A multiaxial fatigue life prediction method for metallic material under combined random vibration loading and mean stress loading in the frequency domain.* International Journal of Fatigue, 2021. **148**: p. 106235.

67. Singh, A. and V. Rohilla, *Optimization and Fatigue Analysisof a Crane Hook Using Finite Element Method.* Int. J. Recent Adv. Mech. Eng, 2015. **4**: p. 31-43.

68. Gates, N. and A. Fatemi, *Multiaxial variable amplitude fatigue life analysis including notch effects.* International Journal of Fatigue, 2016. **91**: p. 337-351.

69. Engin, Z. and D. Coker, *Comparison of equivalent stress methods with critical plane approaches for multiaxial high cycle fatigue assessment.* Procedia Structural Integrity, 2017. **5**: p. 1229-1236.

70. Zerbst, U., et al., *About the fatigue crack propagation threshold of metals as a design criterion–a review.* Engineering Fracture Mechanics, 2016. **153**: p. 190-243.

71. Santus, C. and D. Taylor, *Physically short crack propagation in metals during high cycle fatigue.* International Journal of Fatigue, 2009. **31**(8-9): p. 1356-1365.

72. Pugno, N., et al., *A generalized Paris' law for fatigue crack growth.* Journal of the Mechanics and Physics of Solids, 2006. **54**(7): p. 1333-1349.

73. Brückner-Foit, A. and X. Huang, *Numerical simulation of micro-crack initiation of martensitic steel under fatigue loading.* International journal of fatigue, 2006. **28**(9): p. 963-971.

74. Pham, M. and S. Holdsworth, *Role of microstructural condition on fatigue damage development of AISI 316L at 20 and 300 C.* International journal of fatigue, 2013. **51**: p. 36-48.

75. Obrtlík, K., et al., *Short fatigue crack behaviour in 316L stainless steel.* International journal of fatigue, 1997. **19**(6): p. 471-475.

76. Kitagawa, H., *Applicability of fracture mechanics to very small cracks or the cracks in the early stage.* Proc. of 2nd ICM, Cleveland, 1976, 1976: p. 627-631.

77. Miller, K., *The short crack problem.* Fatigue & Fracture of Engineering Materials & Structures, 1982. **5**(3): p. 223-232.

78. Miller, K., *The two thresholds of fatigue behaviour.* Fatigue & Fracture of Engineering Materials & Structures, 1993. **16**(9): p. 931-939.

79. El Haddad, M., K. Smith, and T.H. Topper, *Fatigue crack propagation of short cracks.* 1979.

80. Araújo, J. and D. Nowell, *Analysis of pad size effects in fretting fatigue using short crack arrest methodologies.* International Journal of Fatigue, 1999. **21**(9): p. 947-956.

81. de Pannemaecker, A., S. Fouvry, and J. Buffiere, *Reverse identification of short–long crack threshold fatigue stress intensity factors from plain fretting crack arrest analysis.* Engineering Fracture Mechanics, 2015. **134**: p. 267-285.

82. Chapetti, M.D., *Fatigue propagation threshold of short cracks under constant amplitude loading.* International Journal of Fatigue, 2003. **25**(12): p. 1319-1326.

83. Irwin, G.R., *Analysis of stresses and strains near the end of a crack traversing a plate.* 1957.

84. Paris, P. and F. Erdogan, *A critical analysis of crack propagation laws.* 1963.

85. Stamenkovic, D. and B.M. Eng. *Determination of fracture mechanics parameters using FEM and J-integral approach*. in *Finite element simulation of the high risk constructions, Special Session, within 2nd WSEAS International Conference on Applied and Theoretical Mechanics (MECHANICS'06), Eds Mijuca, D and Maksimovic, S., Venice*. 2006.

86. Elber, W., *The significance of fatigue crack closure.* 1971.

87. Correia, J.A., et al., *Crack closure effects on fatigue crack propagation rates: application of a proposed theoretical model.* Advances in Materials Science and Engineering, 2016. **2016**.

88. Newman Jr, J.C., *A crack opening stress equation for fatigue crack growth.* International Journal of fracture, 1984. **24**.

89. Dinda, S. and D. Kujawski, *Correlation and prediction of fatigue crack growth for different R-ratios using Kmax and ΔK+ parameters.* Engineering Fracture Mechanics, 2004. **71**(12): p. 1779-1790.

90. McClintock, F. and G. Irwin, *Plasticity aspects of fracture mechanics*. 1965: ASTM International West Conshohocken.

91. Sun, C.-T. and Z. Jin, *Fracture mechanics*. 2011: Academic press.

92. S.L. Pu, G.T.S., *The bauschinger effect of reverse yield stress reduction on radial crack growth of a cylindrical pressure vessel.* Engineering Fracture Mechanics, 1987. **26**(4): p. 519-531.

93. Smith, R.W., M.H. Hirschberg, and S. Manson, *Fatigue behavior of materials under strain cycling in low and intermediate life range*. 1963: National Aeronautics and Space Administration Washington, DC, USA.

94. Lopez, Z. and A. Fatemi, *A method of predicting cyclic stress–strain curve from tensile properties for steels.* Materials Science and Engineering: A, 2012. **556**: p. 540-550.

95. Skallerud, B. and P. Larsen, *A uniaxial cyclic plasticity model including transient material behaviour.* Fatigue & Fracture of Engineering Materials & Structures, 1989. **12**(6): p. 611-625.

96. Prager, W., *A new method of analyzing stresses and strains in work-hardening plastic solids.* 1956.

97. Armstrong, P.J. and C. Frederick, *A mathematical representation of the multiaxial Bauschinger effect*. Vol. 731. 1966: Berkeley Nuclear Laboratories Berkeley, CA.

98. Halama, R., J. Sedlák, and M. Šofer, *Phenomenological modelling of cyclic plasticity.* Numerical modelling, 2012. **1**: p. 329-354.

99. Lee, C.-H., V.N. Van Do, and K.-H. Chang, *Analysis of uniaxial ratcheting behavior and cyclic mean stress relaxation of a duplex stainless steel.* International Journal of Plasticity, 2014. **62**: p. 17-33.

100. Novak, J.S., et al. *Estimation of material parameters in nonlinear hardening plasticity models and strain life curves for CuAg alloy*. in *IOP Conference Series: Materials Science and Engineering*. 2016. IOP Publishing.

101. Okorokov, V., et al., *New formulation of nonlinear kinematic hardening model, Part I: A Dirac delta function approach.* International Journal of Plasticity, 2019. **122**: p. 89-114.

102. Chaboche, J., *Unified Model of Cyclic Viscoplasticity Based on the Nonlinear Kinematic Hardening Rule*, in *Handbook of Materials Behavior Models*. 2001, Elsevier. p. 358-367.

103. Bari, S. and T. Hassan, *Anatomy of coupled constitutive models for ratcheting simulation.* International Journal of Plasticity, 2000. **16**(3-4): p. 381-409.

104. Li, H., R. Johnston, and D. Mackenzie, *Effect of autofrettage in the thick-walled cylinder with a radial cross-bore.* 2010.

105. Herz, E., O. Hertel, and M. Vormwald, *Numerical simulation of plasticity induced fatigue crack opening and closure for autofrettaged intersecting holes.* Engineering Fracture Mechanics, 2011. **78**(3): p. 559-572.

106. Okorokov, V., D. MacKenzie, and Y. Gorash. *Fatigue and corrosion fatigue life assessment with application to autofrettaged parts*. in *Pressure Vessels and Piping Conference*. 2018. American Society of Mechanical Engineers.

107. Vormwald, M., et al., *Fatigue strength of autofrettaged diesel injection system components under elevated temperature.* International Journal of Fatigue, 2018. **113**: p. 428-437.

108. Okorokov, V., et al., *High cycle fatigue analysis in the presence of autofrettage compressive residual stress.* Fatigue & Fracture of Engineering Materials & Structures, 2018. **41**(11): p. 2305-2320.

109. Kamaya, M., *Fatigue crack tolerance design for stainless steel by crack growth analysis.* Engineering Fracture Mechanics, 2017. **177**: p. 14-32.

110. Murthy, A.R., et al., *Prediction of fatigue crack initiation life in SA312 Type 304LN austenitic stainless steel straight pipes with notch.* Nuclear Engineering and Technology, 2022. **54**(5): p. 1588-1596.

111. Hu, Y., Z. Hu, and S. Cao, *Theoretical study on Manson-Coffin equation for physically short cracks and lifetime prediction.* Science China Technological Sciences, 2012. **55**: p. 34-42.

112. Xu, J., Z. Zhang, and T. Wu. *Residual fatigue lives assessment of riveted lap joints based on a crack growth model*. in *Structures*. 2021. Elsevier.

113. Needleman, A., *A continuum model for void nucleation by inclusion debonding.* 1987.

114. Belytschko, T. and T. Black, *Elastic crack growth in finite elements with minimal remeshing.* International journal for numerical methods in engineering, 1999. **45**(5): p. 601-620.

115. Moës, N., J. Dolbow, and T. Belytschko, *A finite element method for crack growth without remeshing.* International journal for numerical methods in engineering, 1999. **46**(1): p. 131-150.

116. Doğan, O., C. Yuce, and F. Karpat, *Effects of rim thickness and drive side pressure angle on gear tooth root stress and fatigue crack propagation life.* Engineering Failure Analysis, 2021. **122**: p. 105260.

117. Ignatijev, A., et al., *Fatigue crack initiation and propagation in a PM-gear tooth root.* Engineering Failure Analysis, 2022. **138**: p. 106355.

118. Lee, Y.F. and Y. Lu, *Advanced numerical simulations considering crack orientation for fatigue damage quantification using nonlinear guided waves.* Ultrasonics, 2022. **124**: p. 106738.

119. Shittu, A.A., et al., *Structural reliability assessment of offshore wind turbine support structures subjected to pitting corrosion‐fatigue: A damage tolerance modelling approach.* Wind Energy, 2020. **23**(11): p. 2004-2026.

120. Yu, H. and M. Kuna, *Interaction integral method for computation of crack parameters K–T–A review.* Engineering Fracture Mechanics, 2021. **249**: p. 107722.

121. Celada-Casero, C., et al., *The influence of the austenite grain size on the microstructural development during quenching and partitioning processing of a low-carbon steel.* Materials & Design, 2019. **178**: p. 107847.

122. Huang, J.-Y., et al., *High-cycle fatigue behavior of type 316L stainless steel.* Materials transactions, 2006. **47**(2): p. 409-417.

123. ASTM, E.-. *Standard practice for conducting force controlled constant amplitude axial fatigue tests of metallic materials.* West Conshohocken, 2021.

124. Carpinteri, A., *Shape change of surface cracks in round bars under cyclic axial loading.* International Journal of Fatigue, 1993. **15**(1): p. 21-26.

125. Carpinteri, A., C. Ronchei, and S. Vantadori, *Stress intensity factors and fatigue growth of surface cracks in notched shells and round bars: two decades of research work.* Fatigue & Fracture of Engineering Materials & Structures, 2013. **36**(11): p. 1164-1177.

126. Pegues, J.W., M.D. Roach, and N. Shamsaei, *Influence of microstructure on fatigue crack nucleation and microstructurally short crack growth of an austenitic stainless steel.* Materials Science and Engineering: A, 2017. **707**: p. 657-667.

127. Newman Jr, J., *A crack opening stress equation for fatigue crack growth.* International Journal of fracture, 1984. **24**.

128. Garcia, C., et al., *Fatigue crack growth in residual stress fields.* International Journal of Fatigue, 2016. **87**: p. 326-338.

129. Lam, Y. and K. Lian, *The effect of residual stress and its redistribution of fatigue crack growth.* Theoretical and Applied Fracture Mechanics, 1989. **12**(1): p. 59-66.

130. Gardin, C., et al., *Numerical simulation of fatigue crack propagation in compressive residual stress fields of notched round bars.* Fatigue & Fracture of Engineering Materials & Structures, 2007. **30**(3): p. 231-242.

131. Newman Jr, J. and S. Daniewicz, *Predicting crack growth in specimens with overloads and cold-worked holes with residual stresses.* Engineering Fracture Mechanics, 2014. **127**: p. 252-266.

132. Ma, Y.E., et al., *Size effects on residual stress and fatigue crack growth in friction stir welded 2195-T8 aluminium–Part II: Modelling.* International Journal of Fatigue, 2011. **33**(11): p. 1426-1434.

133. Ma, Y.E., et al., *Size effects on residual stress and fatigue crack growth in friction stir welded 2195-T8 aluminium–Part I: Experiments.* International Journal of Fatigue, 2011. **33**(11): p. 1417-1425.

134. Al‐Mukhtar, A., *Consideration of the residual stress distributions in fatigue crack growth calculations for assessing welded steel joints.* Fatigue & Fracture of Engineering Materials & Structures, 2013. **36**(12): p. 1352-1361.

135. Kashaev, N., et al., *On the prediction of fatigue crack growth based on weight functions in residual stress fields induced by laser shock peening and laser heating.* Fatigue & Fracture of Engineering Materials & Structures, 2021. **44**(12): p. 3463-3481.

136. Bueckner, H., *Weight functions for the notched bar.* ZAMM ‐ Journal of Applied Mathematics and Mechanics/Zeitschrift für Angewandte Mathematik und Mechanik, 1971. **51**(2): p. 97-109.

137. Glinka, G. and G. Shen, *Universal features of weight functions for cracks in mode I.* Engineering Fracture Mechanics, 1991. **40**(6): p. 1135-1146.

138. Zheng, X., G. Glinka, and R. Dubey, *Stress intensity factors and weight functions for a corner crack in a finite thickness plate.* Engineering fracture mechanics, 1996. **54**(1): p. 49-61.

139. Guo, K., R. Bell, and X. Wang, *The stress intensity factor solutions for edge cracks in a padded plate geometry under general loading conditions.* International journal of fatigue, 2007. **29**(3): p. 481-488.

140. Al-Mukhtar, A., *Residual stresses and stress intensity factor calculations in T-welded joints.* Journal of failure analysis and prevention, 2013. **13**: p. 619-623.

141. Bao, R., X. Zhang, and N.A. Yahaya, *Evaluating stress intensity factors due to weld residual stresses by the weight function and finite element methods.* Engineering Fracture Mechanics, 2010. **77**(13): p. 2550-2566.

142. Xiao, X., V. Okorokov, and D. Mackenzie, *High cycle fatigue life assessment of notched components with induced compressive residual stress.* International Journal of Pressure Vessels and Piping, 2023: p. 105069.

143. ASTM, E., *Standard test methods for tension testing of metallic materials.* Annual book of ASTM standards. ASTM, 2021.

144. Gorash, Y. and D. MacKenzie, *On cyclic yield strength in definition of limits for characterisation of fatigue and creep behaviour.* Open Engineering, 2017. **7**(1): p. 126-140.

145. Khan, A.S., A. Pandey, and T. Stoughton, *Evolution of subsequent yield surfaces and elastic constants with finite plastic deformation. Part III: Yield surface in tension–tension stress space (Al 6061–T 6511 and annealed 1100 Al).* International Journal of Plasticity, 2010. **26**(10): p. 1432-1441.

146. Michno Jr, M.J. and W.N. Findley, *An historical perspective of yield surface investigations for metals.* International Journal of Non-Linear Mechanics, 1976. **11**(1): p. 59-82.

147. Ishikawa, H., *Subsequent yield surface probed from its current center.* International Journal of Plasticity, 1997. **13**(6-7): p. 533-549.

148. Abdel-Karim, M., *Effect of elastic modulus variation during plastic deformation on uniaxial and multiaxial ratchetting simulations.* European Journal of Mechanics-A/Solids, 2011. **30**(1): p. 11-21.

149. Dutta, A., S. Dhar, and S. Acharyya, *Material characterization of SS 316 in low-cycle fatigue loading.* Journal of Materials Science, 2010. **45**(7): p. 1782-1789.

150. Xie, X.-f., et al., *Cyclic hardening/softening behavior of 316L stainless steel at elevated temperature including strain-rate and strain-range dependence: Experimental and damage-coupled constitutive modeling.* International Journal of Plasticity, 2019. **114**: p. 196-214.

151. Schijve, J., *The stress intensity factor of small cracks at notches.* Fatigue & Fracture of Engineering Materials & Structures, 1982. **5**(1): p. 77-90.

152. Kamaya, M., *Ramberg–Osgood type stress–strain curve estimation using yield and ultimate strengths for failure assessments.* International Journal of Pressure Vessels and Piping, 2016. **137**: p. 1-12.

153. Milella, P.P., *Fatigue and corrosion in metals*. 2012: Springer Science & Business Media.

154. Standard, A., *Standard test method for measurement of fatigue crack growth rates.* (No Title), 2002. **3**.

155. Strzelecki, P., J. Sempruch, and T. Tomaszewski, *Analysis of selected mathematical models of high-cycle SN characteristics.* Technical Sciences, 2017. **20**(3): p. 227-240.

156. Dong, J., et al., *Fatigue crack propagation experiment and numerical simulation of 42CrMo steel.* Proceedings of the Institution of Mechanical Engineers, Part C: Journal of Mechanical Engineering Science, 2020. **234**(14): p. 2852-2862.

157. Sellen, S., et al., *Design rules for autofrettage of an aluminium valve body.* Fatigue & Fracture of Engineering Materials & Structures, 2016. **39**(1): p. 68-78.

158. Chapetti, M.D. and L.F. Jaureguizahar, *Fatigue behavior prediction of welded joints by using an integrated fracture mechanics approach.* International Journal of Fatigue, 2012. **43**: p. 43-53.

159. Zerbst, U., et al., *The IBESS approach for the determination of the fatigue life and strength of Weldments by fracture mechanics analysis*, in *Fatigue and Fracture of Weldments*. 2019, Springer.

160. Thumser, R., J.W. Bergmann, and M. Vormwald, *Residual stress fields and fatigue analysis of autofrettaged parts.* International Journal of Pressure Vessels and Piping, 2002. **79**(2): p. 113-117.

161. Mohammad, K., et al. *Fatigue behavior of austenitic type 316L stainless steel*. in *IOP conference series: materials science and engineering*. 2012. IOP Publishing.

162. Wang, M., et al., *Characterization of Grain Size in 316L Stainless Steel Using the Attenuation of Rayleigh Wave Measured by Air-Coupled Transducer.* Materials, 2021. **14**(8): p. 1901.

163. Caspers, M., C. Mattheck, and D. Munz, *Propagation of surface cracks in notched and unnotched rods*. 1990: ASTM International.

164. Jíša, D., et al., *Small fatigue crack growth in aluminium alloy EN-AW 6082/T6.* International Journal of Fatigue, 2010. **32**(12): p. 1913-1920.

165. Lukács, J., Á. Meilinger, and D. Pósalaky, *High cycle fatigue and fatigue crack propagation design curves for 5754-H22 and 6082-T6 aluminium alloys and their friction stir welded joints.* Welding in the World, 2018. **62**: p. 737-749.

166. Borrego, L., J. Ferreira, and J. Costa, *Fatigue crack growth and crack closure in an AlMgSi alloy.* Fatigue & Fracture of Engineering Materials & Structures, 2001. **24**(4): p. 255-265.

167. Mann, T., *The influence of mean stress on fatigue crack propagation in aluminium alloys.* International journal of fatigue, 2007. **29**(8): p. 1393-1401.

168. Li, D.-f., X.-j. Wang, and Z.-l. Zhao, *Grain orientation and texture analysis of 6082 aluminum alloy friction plug welded joints.* Journal of Materials Research and Technology, 2022. **18**: p. 1763-1771.

169. Li, J., et al., *Multiaxial fatigue life prediction for various metallic materials based on the critical plane approach.* International Journal of Fatigue, 2011. **33**(2): p. 90-101.

170. LaRue, J. and S. Daniewicz, *Predicting the effect of residual stress on fatigue crack growth.* International Journal of Fatigue, 2007. **29**(3): p. 508-515.

171. Ding, F., M. Feng, and Y. Jiang, *Modeling of fatigue crack growth from a notch.* International journal of plasticity, 2007. **23**(7): p. 1167-1188.

172. Papuga, J., M. Vargas, and M. Hronek, *Evaluation of uniaxial fatigue criteria applied to multiaxially loaded unnotched samples.* Engineering Mechanics, 2012. **19**(2): p. 3.